

6 LEED Theory

Applications

We discuss here the methods of quantitative LEED I(V) analysis and their application to relatively complex types of surface structures: quasicrystalline and modulated surfaces.

We first give a short review of the methods that are used to derive a model of the surface structure from the LEED I(V) curves, in Section 6.1. Finding the correct model of the surface structure – as opposed to precise coordinates – is one of the major challenges in LEED. A variety of different approaches have been used, from direct methods to structure search methods. A generally applicable method has still not been found and there is continuing interest in the development of direct methods. We next outline the present status of the field. We also review briefly the phase shift calculation and the development of methods to overcome problems in the muffin-tin potential model.

Sections 6.2 and 6.3 discuss two types of surfaces, quasicrystalline and modulated surfaces, where quantitative analysis is possible but rarely used. With the increasing speed of computers in combination with the calculation methods of NanoLEED, many more surface modulations could be quantitatively analysed by LEED. Regarding quasicrystals we think that it should be possible to identify the composition of clusters by means of LEED, which is still a major problem in X-ray diffraction. To obtain quantitative results in these areas would be impossible or very difficult with methods other than LEED.

6.1 Quantitative Structure Analysis

The structure determination method which has been applied most is the trial and error approach coupled with structure refinement by various optimisation procedures. Numerous surface structures were analysed by LEED: some of these can be found, for example, in the Surface Structure Database (SSD) [6.1; 6.2] and in a review in Landolt-Börnstein, Vol. 45 [6.3].

One of the most common applications of LEED is certainly the observation of the diffraction pattern with the purpose to control the preparation of the surface and to check whether the surface is ordered, disordered or faceted, as well as to identify the size and orientation of superlattices in adsorbate layers and surface reconstructions.

A short description of this qualitative interpretation of the LEED pattern without quantitative multiple scattering calculations is given in Chapter 4.

The surface structure analysis by LEED consists of two steps, similar to the analysis by X-rays. In the first step, a structure model must be found; in the second step, that structure model must be refined by optimising all its parameters. In many cases more than one plausible model must be investigated.

In 3-D X-ray analysis, including in powder diffraction, the first step is rather well developed and direct methods can be applied, such that the analysis has become routine, at least for structures of low and moderate complexity. In X-ray diffraction the term ‘direct methods’ is solely used for methods to determine the phases of the complex structure factors. These methods are based on the fact that the electron density is positive and on the relation between intensities and phases [6.4]. If the phases of the structure factors are known, an image of the electron density is obtained via the Fourier transform of the structure factors. The model obtained in that way must still be refined by optimisation methods.

Direct methods are not, or not yet, applicable in LEED. Although many approaches have been developed with partial success, as will be discussed in this section, no generally applicable method to determine a structure model directly from the LEED intensity data is available. Multiple scattering severely limits the applicability of the kinematic theory: this implies that all standard X-ray methods of deriving models from intensity data, such as Patterson search methods, difference Fourier analysis, phase determination by the heavy atom method and related methods (see, e.g. [6.5]), are not reliably applicable. Also, widely used methods, including the so-called pixel methods, such as the ‘charge flip’ method by which the electron density is determined in an iteration process [6.6], cannot be applied in LEED. The phases of the atomic diffraction amplitudes cannot be determined by the atom positions alone, as is the case in the kinematic theory of diffraction, but by complex scattering factors and the influence of the surroundings of the atom through multiple scattering. We discuss in the next paragraphs the various approaches to removing or at least reducing multiple scattering effects and the special cases where limited success has been reached. Whether a generally applicable direct method can be developed for LEED remains an open question.

Consequently, to start the structural analysis with LEED, one or more suitable models for the surface structure must be proposed, based on the diffraction pattern, specifying size, orientation and symmetry of the surface unit cell and the chemical composition of the surface. In most cases, this information is not sufficient to propose a unique model; then more information can be used from further experimental methods like STM, AFM and various spectroscopic measurements, in order to constrain the surface composition, bond lengths, bond energies, coordination, etc. In most cases, a series of guessed structures are then tested against LEED experiment. Often, the correct structure model was found earlier by DFT calculations (and occasionally by other experimental techniques); in most modern surface structure determinations by LEED, the result is in fact simultaneously or subsequently confirmed by DFT calculations [6.7; 6.8].

With LEED, surface structures are usually determined by using the ‘trial and error’ approach. This means that the experimental I(V) curves are compared with calculated ones for various reasonable models and, once a promising model has been found, the parameters of the model are refined with optimisation procedures to improve the fit to experiment. Usually several promising models are found and locally optimised; normally no ‘global’ optimisation is used to explore other potential models. This procedure is lengthy; the main problem is to find the right initial model or models. The trial and error method always presents the danger that the correct model has not been thought of or some details of the model have been overlooked. Once some agreement between experimental and calculated curves is found for a specific model, the parameters of this model are locally varied until an optimum agreement has been reached. But the result depends on the correctness or completeness of the initial model. Details not included in the model are not found by local optimisation.

To overcome these problems, several approaches have been proposed to use global optimisation, in which many more possible combinations of all parameters are automatically explored. The method aims to avoid getting trapped in local minima of the R-factor, which are always present in the parameter space. This is a fairly general approach, but it is not completely model-free. For example, a chemical element that is missing in the model will not be found by global optimisation. Therefore, the term ‘direct method’ should not be used or confused with global optimisation. The various methods to derive models and to optimise structural parameters have been reviewed by E. A. Soares et al. [6.9].

In Section 6.1.1, we give a short overview of approaches that attempt to derive structural information directly from LEED intensity data without multiple scattering calculations; Sections 6.1.2–6.1.4 address several more specific aspects. These approaches are based on the Patterson function, holography, or thermal diffuse scattering. The resulting preferred models need to be subsequently refined by optimisation methods, which will be summarised in Section 6.1.5. The influence of non-structural parameters on such structure determination will be addressed in Section 6.1.6.

6.1.1 Approaches to Obtain Structural Information Directly from LEED Intensities

6.1.1.1 Averaging Methods and the Patterson Function

The strong interaction of electrons with the surface atoms and the resulting multiple scattering effects impede the use of the kinematic theory. The first attempt to eliminate multiple scattering effects was the constant momentum transfer averaging (CMTA), proposed by M. G. Lagally, M. B. Webb and co-workers [6.10], in which LEED intensities are averaged that were obtained at one point in reciprocal space but at different energies and angles of incidence, both polar angle and azimuth. By repeating this at other points, a range of averaged data is produced across a part of reciprocal space, for example, over a range of momentum transfer values that emphasises kinematic effects (such as Bragg peaks) and thereby suppresses multiple scattering effects. The averaged intensities are then analysed by a kinematic calculation. The fact that

averaging of intensities does not really reduce multiple scattering effects to a negligible background has prevented a successful application of the method for general cases.

The CMTA method was not applied much until it was revived to construct a Patterson function which is submitted to a kinematic analysis. The Patterson function is obtained as the Fourier transform of the intensities and in the kinematic theory it shows all interatomic distances occurring in the surface structure. The first application of the Patterson function to derive interlayer distances from the (00) beam intensities was to analyse some clean metal surfaces by D. L. Adams and U. Landman, with limited success [6.11]. Due to multiple scattering effects, additional peaks occur in the Patterson function which cannot be assigned to interatomic distances.

To overcome this problem, H. Wu and S. Y. Tong [6.12; 6.13] proposed to apply the CMTA method to *averaged* LEED I(V) curves from which they derived the Patterson function. They showed that, by including a broad range of incidence angles and energies, the peaks in the Patterson function could be assigned to interatomic distances. They applied the method successfully to the Si(111)+(4×1)-In surface [6.14]; they could use only the superstructure I(V) curves due to the superposition of three domains and assumed the Si atom positions in the substrate to be known. The same structure was investigated later by T. Abukawa et al. [6.15] using a single domain surface and an extended data set which allowed determining the Si positions in the substrate from the Patterson function. The Patterson function was also used to select possible models in the more complicated system Si(111)+(1×1)-YSi₂ [6.16] and to also distinguish proposed models for the Si(111)+(1×1)-Fe surface [6.17]. A slightly different method to analyse the Patterson function, which was called ‘integral-energy phase-summing method’ [6.18], was applied to reconstructed Si (111) surfaces, namely Si(111)-(7×7) and Si(111)-(3×2). Multiple scattering effects are relatively weak in silicon and the kinematical analysis in the abovementioned studies on Si surfaces probably worked relatively well for that reason. The application to other surfaces has been rare: for the GaN(0001)-($\sqrt{3} \times \sqrt{3}$)R30° system the site of the Ga adatom could be identified with the Patterson function [6.19]; and a similar study of the GaN(0001)-(1×1) surface exhibited a Ga adlayer on a Ga-terminated surface [6.20].

The determination of a Patterson function from LEED I(V) data requires a very large data set, as has been shown by T. Abukawa et al. [6.15]. The derivation of structure models from the Patterson function, which only shows the lengths and direction of interatomic distances, requires a sufficient amount of data such that structure search methods can be applied. With the development of fast experimental techniques and automated evaluation of diffraction images, the method probably could be further developed. However, the applicability to adsorbed layers on metal substrates or systems with strong multiple scattering effects has not yet been proven.

6.1.1.2 Holography

Further methods to obtain structural information from the intensities have been developed by applying ideas of optical holography. The principle of holography, as originally proposed by D. Gabor [6.21], is to reconstruct the image of an object from

the interference pattern (called hologram) due to the wave scattered by the object interfering with the unscattered portion of the primary incident wave (e.g., from a laser): their interference contains the structural details of the object. The reconstruction of the image is typically done by shining a wave identical to the incident wave through the hologram, especially in the optical case with a laser: this produces an image of the original object by simple interference. The idea can be used with electrons: in this case the reconstruction is done computationally, since it is difficult to reproduce the incident electron wave and shine it onto a hologram.

The hologram, whether produced with photon or electron waves, can be written as the interference of object wave $O(\mathbf{k}', \mathbf{k})$ due to the object with reference wave $R(\mathbf{k}', \mathbf{k})$, which is the unscattered incident wave:

$$\begin{aligned} I(\mathbf{k}', \mathbf{k}) &= |R(\mathbf{k}', \mathbf{k}) + O(\mathbf{k}', \mathbf{k})|^2 \\ &= |R(\mathbf{k}', \mathbf{k})|^2 + |O(\mathbf{k}', \mathbf{k})|^2 + |R^*(\mathbf{k}', \mathbf{k})O(\mathbf{k}', \mathbf{k}) + R(\mathbf{k}', \mathbf{k})O^*(\mathbf{k}', \mathbf{k})|. \end{aligned} \quad (6.1)$$

Here \mathbf{k} is the incident wave vector and \mathbf{k}' the wave vector of the scattered wave. The assumption in optical holography is that the reference wave is much stronger than the object wave, such that the second order terms $|O(\mathbf{k}', \mathbf{k})|^2$ can be omitted. The second assumption is that the reference wave does not depend on the direction of \mathbf{k}' , that is, the reference wave is isotropic. These assumptions are not valid for LEED, as has been pointed out by S. Y. Tong [6.22] and others, and the method must be modified for application in LEED. The computational image reconstruction process is ideally a simple Fourier transformation; however, the measurement of intensities rather than wave amplitudes introduces the complication of unknown wave phases and adds a twin image.

In the following, we give a brief description of the approach to interpret a hologram and produce an image from LEED, following the review of K. Heinz et al. [6.23]. The diffraction geometry is illustrated in Figure 6.1. The method requires a reference atom acting as a beam splitter that produces both the reference wave R and the object wave

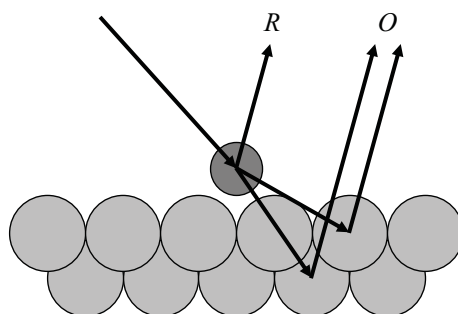


Figure 6.1 An adsorbate atom (darker grey) on a surface splits the incoming wave into reference wave R and object wave O and serves as a reference atom for the surface structure (schematic)

O (this wave R plays the role of the original ‘unscattered’ reference wave, while the wave O plays the role of the ‘scattered’ object wave).

The most obvious application where the object wave and the reference wave can be at least partially separated is for disordered adsorbate layers: for disordered surfaces the diffuse scattering between sharp spots necessarily involves a scattering event from the disordered layer: this event then defines the reference wave R . The case of ordered adsorbate layers is slightly less favourable, as the superstructure intensities occur only partly from single scattering in the superstructure, while scattering from the substrate also contributes through multiple scattering, so that no pure reference wave R exists. The method is not limited to overlayers, however: any atom in the surface can be viewed as a beam splitter; the drawback is then that multiple atoms in the surface qualify as beam splitters, so that the hologram represents the superposition of their multiple neighbourhoods, further complicating the resulting image.

In its simplest form the reference wave scattered from the beam splitter at position \mathbf{r} can be written as

$$R(\mathbf{k}, \mathbf{k}') = F_r(\mathbf{k}, \mathbf{k}') \exp(i\mathbf{k}'\mathbf{r}), \quad (6.2)$$

while the scattered amplitude from the object is given by:

$$O(\mathbf{k}, \mathbf{k}') = \sum_j F_j(\mathbf{k}, \mathbf{k}') \exp(i\mathbf{k}'(\mathbf{r} - \mathbf{r}_j)). \quad (6.3)$$

Here F_r and F_j are the multiple scattering amplitudes due to the beam splitter atom and the object atoms at positions j , respectively. As F_r is assumed to be nearly structureless, that is, independent of \mathbf{k}' , the multiple scattering amplitude F_r is replaced by the single scattering formula. If $|O(\mathbf{k}', \mathbf{k})|^2$ is omitted, the Fourier transform (or more rigorously the Helmholtz–Kirchhoff integral for electrons) of the interference term gives

$$A(\mathbf{r}) = \int (RO^* - OR^*) \exp(-i\mathbf{k}'\mathbf{r}) d^2\mathbf{k}'_{\parallel}, \quad (6.4)$$

where \mathbf{k}'_{\parallel} is the parallel component of \mathbf{k}' . At a fixed energy, the parallel components are the sampling points of the diffuse intensity or of the superstructure spots in the case of ordered structures. The image $A(\mathbf{r})$ consists of a superposition of two terms, called the real image and the twin image. By Eq. (6.1), the interference term $(RO^* - OR^*)$ can be replaced by $I(\mathbf{k}, \mathbf{k}') - |R(\mathbf{k}, \mathbf{k}')|^2$, if $|O(\mathbf{k}', \mathbf{k})|^2$ is assumed to be negligible; $|R(\mathbf{k}, \mathbf{k}')|^2$ can also be omitted, since it only refers to the beam splitter atom and contains no information on other atoms (the beam splitter atom will in any case be at the origin of the resulting image). The image is then approximated as

$$A(\mathbf{r}) \approx \int I(\mathbf{k}, \mathbf{k}') \exp(i\mathbf{k}'\mathbf{r}) d^2\mathbf{k}'_{\parallel}. \quad (6.5)$$

Here, $I(\mathbf{k}, \mathbf{k}')$ is the diffuse intensity or the intensity of the superstructure spots without the integer order spots. This simple evaluation does not work very well due to the neglect of multiple scattering effects and the assumption that $|O(\mathbf{k}', \mathbf{k})|^2$ is small.

Holography was first applied to surfaces in the context of photoelectron diffraction [6.24; 6.25], in which electron scattering is very similar to that in LEED: such ‘photoelectron holography’ (PEH) fits the original optical principle of holography well, since a single adatom can serve as a photoelectron emitter and thus as a reference atom (cf. Figure 6.1). While considerable progress was made with PEH, the relatively complex electron scattering, including multiple scattering and in particular strong forward focusing at higher energies, has limited its applicability in terms of the achievable precision of determining atomic positions [6.26]; nevertheless, useful qualitative structural information is accessible in many cases. For disordered surfaces, photoelectron diffraction (PED) is the method of choice. The reference wave is here generated by a photon which has the advantage to be element-specific and the analysis does not have the problem that the object wave is strong. Nevertheless, further improvements of holographic methods have been proposed and applied for PED, for example, so-called differential photoelectron holography [6.27; 6.28], and may become applicable in future developments in holography by LEED.

The first application of holography in LEED was for diffuse LEED (DLEED) to study the adsorption site of disordered adatoms [6.29–6.31]. As illustrated in Figure 6.1, now the reference wave is the single scattered wave from the adatom, while the object wave consists of the backscattered waves from all other surrounding atoms after being scattered first at the adatom. The strongly scattering adatom is considered as a beam splitter, as shown in Figure 6.1. The 2-D diffuse intensity was inverted by a Fourier transform to reconstruct a real-space image around the adsorption site. This unfortunately gives poor images and spurious peaks arising from multiple scattering effects.

A number of approaches were proposed to overcome these problems (e.g., [6.32; 6.33]). A better 3-D image of the surface was obtained for K/Ni(100) from a set of diffuse LEED patterns, by compensating the anisotropy of the reference wave by an appropriate scattered-wave kernel [6.34; 6.35]; this was also applied to SiC(111)–(3×3) [6.36] and 6H-SiC(0001)–(2×2) [6.37]. A summary is given in U. Starke et al. [6.38]. To reduce disturbances, an iterative procedure was proposed [6.39]; a further approach separates the multiple scattering paths into one part solely taking place in the known substrate and a second part involving the unknown surface [6.40]; thereby simultaneous occupation of different adsorption sites was identified for O/Ni(111) [6.41]. H. Wu et al. [6.42] introduced the selective holographic atomic-reference-pair (SHARP) transformation to directly reconstruct 3D atomic images from LEED I(V) curves using a multiple-incident angle and multiple-energy integral: they applied it to Si(111)+($\sqrt{3} \times \sqrt{3}$)R30°–Ga. The LEED holographic method has been reviewed by K. Heinz et al. [6.23].

Although in several cases a direct image of the adsorption site could be obtained, the holographic method is still not generally applicable, in particular for more complicated adsorption structures and especially for materials with strong multiple scattering, such as metals. Holography by LEED is thus not established as a routine method for surface structure analysis.

6.1.1.3 Further Approaches

The strong correlation of vibrations between near-neighbour atoms induces broad features in the thermal diffuse scattering, called correlated thermal diffuse scattering (CTDS), which can be analysed with a kinematic theory. This has been applied to the higher energies of 500–2,000 eV in medium energy electron diffraction (MEED) [6.43].

6.1.2 Comparison of Measured and Calculated I(V) Curves

The main methods of structure analysis by LEED rely on the fitting of theoretically calculated I(V) curves to experimental curves. This requires criteria to quantify the agreement between experimental and calculated intensities: these criteria are usually captured in so-called R-factors (a name abbreviated from reliability factors or residual factors).

For structure analysis by LEED, one normally measures continuous I(V) curves (here we shall use the equivalent quantity $I(E)$ in formulas, while in the LEED literature the designations I(V), I-V, IV or I/V are customary in text). The measurement is usually done with sufficiently small energy steps so that interpolation between the points is possible, a continuous curve can be drawn and the first derivative dI/dE – or even the second derivative – can be calculated.

In close analogy with X-ray crystallography (where individual Bragg reflection intensities rather than continuous curves are measured), we can define R-factors that quantify the closeness of theoretical and experimental data: this will both allow estimating the validity of a given structural model and enable a refinement of the structural parameters. The following simple R-factors have been proposed (summation rather than integration applies to larger energy intervals):

$$R_1 = A_1 \int |I_{ex} - cI_{th}| dE, \quad (6.6)$$

$$R_2 = A_2 \int |I_{ex} - cI_{th}|^2 dE. \quad (6.7)$$

Here the subscripts *ex* and *th* stand for experiment and theory, respectively, and the integration (or summation) ranges over the energy intervals common to experiment and theory in each diffracted beam considered. In practice, with these R-factors as well as with other R-factors defined later in this section, one calculates separate R-factors for different beams and then averages these beam-specific R-factors with weights proportional to the energy intervals of the different beams. The constant *c* is inserted to account for the usually unknown relative intensity scales in the experiment and in the theory, and it serves to normalise the curves to each other (usually for each beam separately), for example through:

$$c = \left(\int I_{ex} dE \right) / \left(\int I_{th} dE \right). \quad (6.8)$$

The prefactors A_1 and A_2 in Eqs. (6.6) and (6.7) are designed to render the R-factor dimensionless and to provide normalisation. The usual choice is

$$A_1 = 1 / \int I_{ex} dE, \quad (6.9)$$

$$A_2 = 1 / \int I_{ex}^2 dE. \quad (6.10)$$

The R-factor R_2 is used only occasionally, mainly in refinement of parameters when the structure model has been determined. R_2 compares the square of the difference between experimental and calculated intensities, therefore it emphasises the strong intensities, while R_1 compares the linear difference between intensities giving all peaks the same weight. R_1 is rarely used in LEED I(V) analyses but the analogous R-factor is frequently applied in X-ray analyses, with the difference that there X-ray structure factors are compared instead of intensities. Neither of these R-factors requires continuous I(V) curves, so they can be defined for discrete energies allowing large energy steps in the calculation, thus saving computing time but losing details of the intensity functions. R_1 has been called R_{DE} in these cases and has been found to be quite reliable up to steps of 15 eV on the energy scale when the I(V) curves contain enough points [6.44].

The comparison of continuous I(E) curves makes the LEED analysis more closely related to X-ray *powder* diffraction than to X-ray *single crystal* analysis. There is, nevertheless, a difference with respect to powder diffraction, as the comparison of peak positions and their intensities presents some problems in LEED. The peak positions cannot be indexed as is the case in X-ray powder diffraction. The multiple scattering in LEED creates complications: there are additional peaks that cannot be related to a kinematic reflection and also can overlap with other peaks; in addition, the peak locations, peak heights and peak widths are affected by atomic phase shifts and multiple scattering, as well as by inelastic and thermal effects and by structural defects; furthermore, some of the latter effects are not accurately reproduced in theory.

In the R-factor R_2 , the peaks are weighted in proportion to the square of their heights. This is often not realistic. While a small peak is less reliably measured, its mere existence and its position on the energy scale imply equally valuable geometrical information as that of a large peak. This is especially true of the higher-energy parts of I(V) curves, where thermal and atomic scattering effects often make all intensities relatively much smaller than at the lower energies, while the energies at which these small peaks occur remain highly important. For these reasons, J. B. Pendry has proposed an R-factor that attempts to treat all peaks (and minima) with equal weights [6.45]. This is based on the logarithmic derivative L of the I(V) curves:

$$L(E) = \frac{1}{I(E)} \cdot \frac{dI(E)}{dE}. \quad (6.11)$$

Pendry has suggested a corresponding R-factor, which avoids singularities when $I(E) = 0$ by defining the function

$$Y(E) = \frac{L^{-1}}{(L^{-2} + V_{0i}^2)}, \quad (6.12)$$

where $2V_{0i}$ can be taken to be the average peak width of single peaks (as opposed to overlapping peaks). V_{0i} is normally chosen to be the imaginary part of the inner potential, which acts as the damping parameter; usually values between 4 and 5 eV are assumed at medium energies around 100–150 eV. Pendry's R-factor is then defined as:

$$R_P = \frac{\sum_{hk} \sum_i (Y_{hk,i}^{th} - Y_{hk,i}^{ex})^2}{\sum_{hk} \sum_i (Y_{hk,i}^{th} + Y_{hk,i}^{ex})^2}, \quad (6.13)$$

where the index i labels the energy points of the beam (hk), usually in 1 eV steps. R_P has become the most commonly used R-factor and has become the standard estimate of the quality of a LEED analysis. The definition of this R-factor leads to values of $R_P = 0$ for perfect agreement, $R_P = 1$ for random agreement and $R_P = 2$ for total anti-correlation of $I(V)$ curves.

Values around $R_P = 0.1$ can be considered to indicate a very good agreement. With values between 0.2 and 0.3 the structure model may be qualitatively correct, but details are certainly not correct, giving large error bars. It should be noted that very good agreement can be reached with measurements at low temperature (LN₂ temperature and below) and with a large energy range, avoiding the low energy range below 50–60 eV. At room temperature usually only a limited energy range is measurable because of the weak intensities and high background at higher energies. The agreement at room temperature is worse than at lower temperatures because of inadequate treatment of thermal motion. When judging the reliability of an analysis by the minimum R-factor obtained for the best fit result, the temperature of the experimental data should therefore be considered.

Examples for some LEED analyses with low, medium and high level of agreement are shown in Figures 6.2–6.4, respectively.

One disadvantage of R_P is that it requires the calculation of derivatives, which implies that it is sensitive to noise in the experimental data: it is therefore useful to average equivalent data (e.g., $I(V)$ curves measured multiple times or for symmetry-equivalent beams) to reduce the noise. Another minor difficulty arises from the fact that the Y-function may become 0 in both experimental and theoretical $I(E)$ curves for any structure. If the theoretical intensities vanish in a certain energy range and there is background with noise in the experimental data, then R_P becomes 1 in that energy range and may increase the R-factor substantially without indicating a disagreement. The corresponding data points should be omitted. Such a case occurs for example for stepped surfaces: the $I(V)$ curves then exhibit a wide energy range between the Bragg points with theoretically negligible intensity where only background is measured experimentally. The calculated $I(V)$ curve should confirm that in

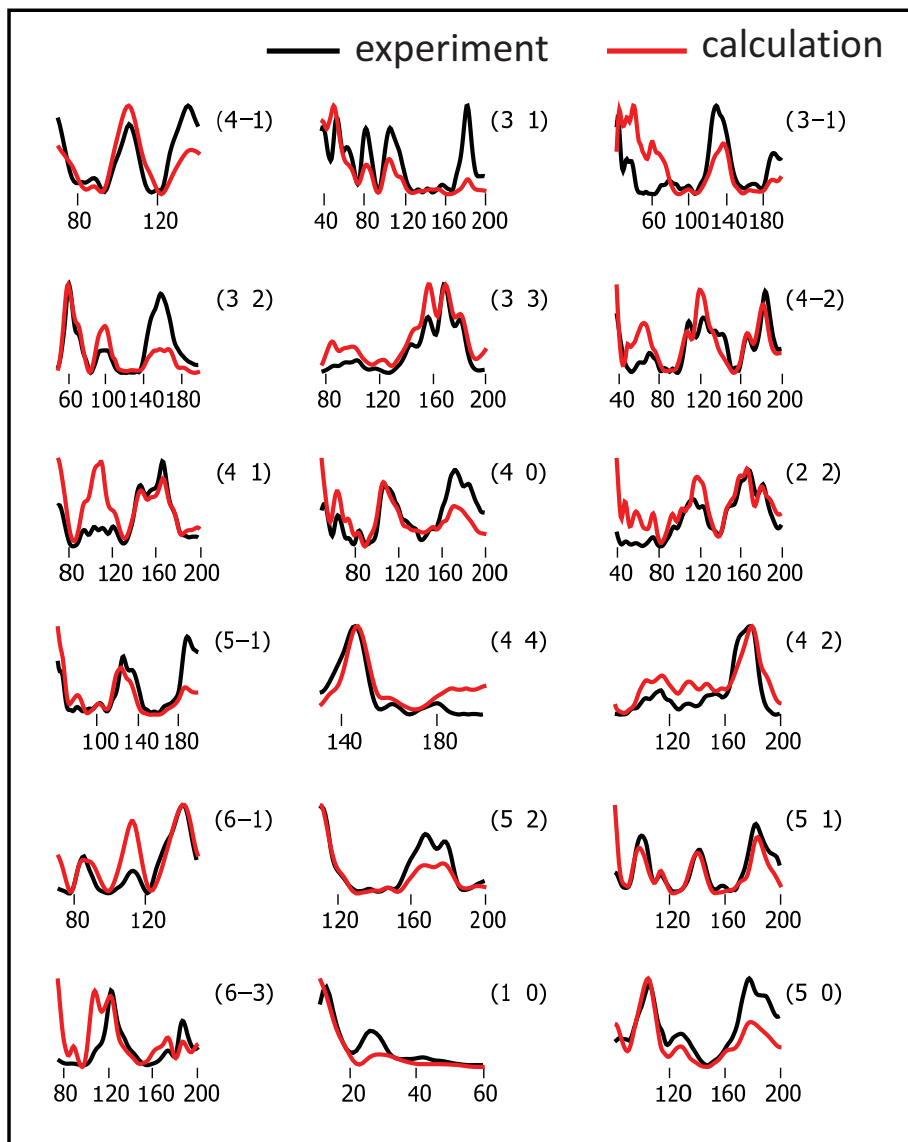


Figure 6.2 Comparison of experimental (black lines) and calculated $I(V)$ curves (red lines) of $\text{Cu}(111) + (3\sqrt{3} \times 3\sqrt{3})\text{R}30^\circ\text{-TMB}$. Intensities of experimental and calculated curves are approximately normalised for each beam separately (with arbitrary units), while energies are given in eV. The average Pendry R-factor of all beams is $R_P = 0.32$. This agreement is not quite satisfactory but is sufficient to identify the structure model and to determine the main parameters; the error bars are large and some structural details are certainly incorrect. TMB stands for 1,3,5-tris(4-mercaptophenyl)-benzene (with chemical formula $\text{C}_{24}\text{H}_{15}\text{S}_3$). Adapted from [6.46] Th. Sirtl, J. Jelic, J. Meyer, K. Das, W. M. Heckl, W. Moritz, J. Rundgren, M. Schmittel, K. Reuter and M. Lackinger, *Phys. Chem. Chem. Phys.*, vol. 15, pp. 11054–11060, 2013, Electronic Supplementary Information (ESI), <https://doi.org/10.1039/c3cp50752a>, with permission from the PCCP Owner Societies.

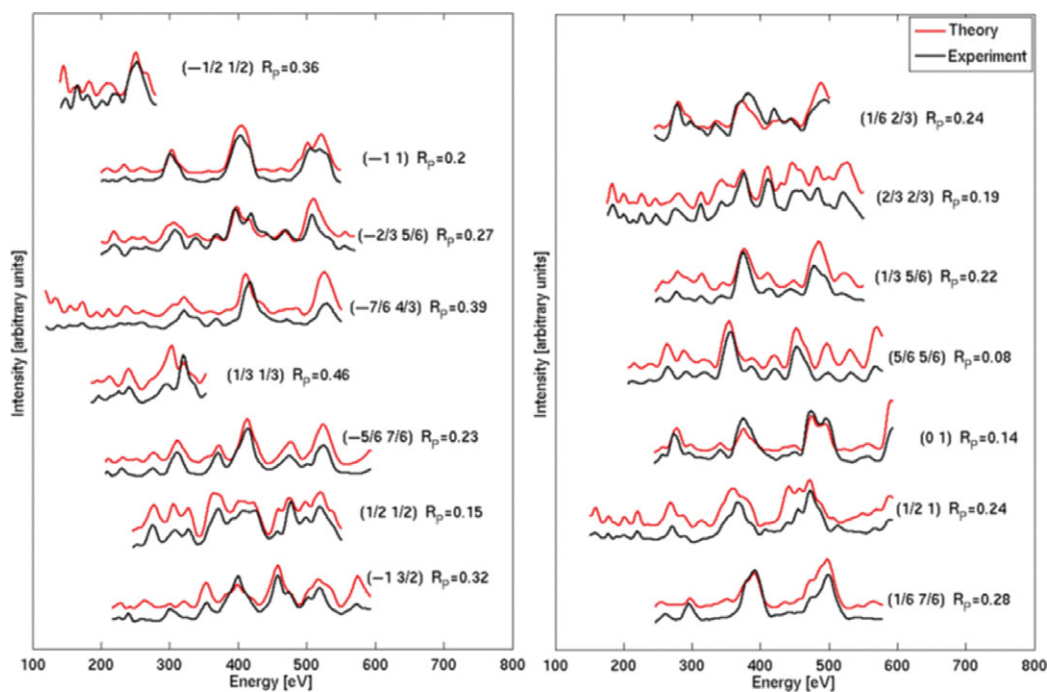


Figure 6.3 Comparison of experimental (black lines) and calculated I(V) curves (red lines) of $\text{Ag}(111) + (2\sqrt{3} \times 2\sqrt{3})\text{R}30^\circ - \text{C}_{60}$. The average Pendry R-factor of all beams is $R_P = 0.24$ and indicates good agreement. It is sufficient to identify the structure model and details of the surface structure. A better agreement cannot be expected in view of the complexity of the system with mixing of two orientations of C_{60} molecules. Reprinted with permission from [6.47] K. Pussi, H. I. Li, H. Shin, L. N. Serkovic Loli, A. K. Shukla, J. Ledieu, V. Fournée, L. L. Wang, S. Y. Su, K. E. Marino, M. V. Snyder and R. D. Diehl, *Phys. Rev. B*, vol. 86, p. 205406, 2012; Supplementary Material. <https://doi.org/10.1103/PhysRevB.86.205406>. © (2012) by the American Physical Society.

this energy range no peak occurs, but in the R-factor analysis this energy range should be omitted.

Pendry's R-factor is not quite metric, meaning that its convergence does not guarantee that the theoretical and experimental curves are necessarily converging together. This non-metric character is due to V_{0i} in the definition of the Y -function, Eq. (6.12), which implies that the R-factor depends on the length of the energy range of the I(V) curves. Test calculations revealed that in all cases the influence on structural results can be neglected.

While many other R-factors were proposed for LEED, only one of these has been used extensively, namely the 'reduced' Zanazzi-Jona R-factor R_{ZJ} [6.49]. This uses the first and second derivatives of $I(E)$ with respect to energy and is defined as:

$$R_{ZJ} = A_{ZJ} \int [|I''_{ex} - cI''_{th}| |I'_{ex} - cI'_{th}| / (|I'_{ex}| + \max |I'_{ex}|)] dE \quad (6.14)$$

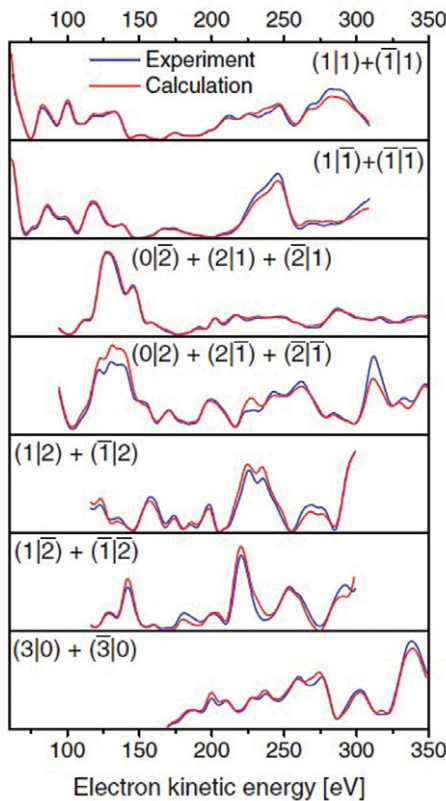


Figure 6.4 Example of an excellent agreement in the LEED I(V) analysis of MoO₃/Au(111)-c(4×2). The final R-factor is $R_P = 0.044$. Reprinted from [6.48] E. Primorac, H. Kuhlenbeck and H.-J. Freund, *Surf. Sci.*, vol. 649, pp. 90–100, 2016, with permission from Elsevier.

with

$$A_{ZJ} = 1 \left/ \left(0.027 \int I_{ex} dE \right) \right.. \quad (6.15)$$

The reduction factor 0.027 is a typical average value that R_{ZJ} would have in the absence of this factor for unrelated LEED curves. In addition, this factor makes R_{ZJ} dimensionless. The Zanazzi-Jona R-factor suffers from slightly higher computational costs and has been found to behave somewhat less predictably than other R-factors in conventional structural determination, perhaps because of the inclusion of second derivatives of I(V) curves which enhance sensitivity to experimental noise. This has been used in earlier structure determinations but was not used in recent LEED I(V) analyses. We also mention that a series of metric distances have been defined by J. Philip and J. Rundgren [6.50] which are less sensitive to noise in the data, but they also require a relatively higher computational effort and are rarely used.

6.1.3 Error Estimates

The LEED I(V) curves can be viewed as a superposition of Lorentzian curves. The peaks are narrow at low energies and become broader at high energies when the curves are drawn as a function of energy, due to the gradually increasing imaginary part of the inner potential V_{0i} , which dominates the peak width. However, when viewed as a function of the wavenumber k , the single peaks have approximately constant width, cf. Figure 6.5.

It is obvious from Figure 6.5 that well separated peaks rarely occur since peaks frequently overlap. The relevant information in the I(V) curves is therefore given by the number of peaks, the peak positions and their heights. Thus, the I(V) curves can be well represented by specifying only the positions, heights and widths of individual Lorentzian peaks. We therefore should count the number of these parameters as the number of independent data points, independent of the number of energy points at which the experimental I(V) curves were measured. Nevertheless, the experimental energy step plays a significant role: a smaller step provides additional data points and thus reduces the experimental noise by allowing better smoothing of the I(V) curves.

The number of independent experimental data points and the number of parameters affect the error bars and the reliability of the analysis. The error bars for the

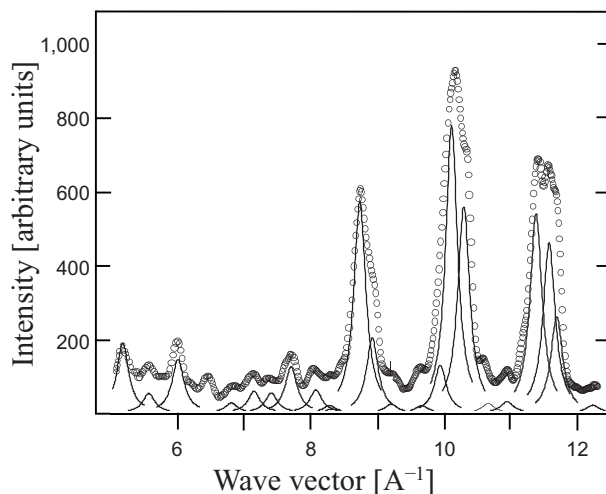


Figure 6.5 Example showing that I(V) curves (with experimental data points shown as circles) are well reproduced by a superposition of Lorentzian peaks (continuous lines) when presented in k -space. The Lorentzian peaks have approximately constant width in k -space. Shown is the $(-1,1)$ beam of $C_{60}/Ag(111)$. Figure drawn with permission from [6.47] K. Pussi, H. I. Li, H. Shin, L. N. Serkovic Loli, A. K. Shukla, J. Ledieu, V. Fournée, L. L. Wang, S. Y. Su, K. E. Marino, M. V. Snyder and R. D. Diehl, *Phys. Rev. B*, vol. 86, p. 205406, 2012; Supplementary Material. <https://doi.org/10.1103/PhysRevB.86.205406>. © (2012) by the American Physical Society.

model parameters are usually estimated from the expectation values for the R-factors assuming random errors in the data points or from a statistical analysis considering experimental errors and independent parameters. Both ways are used in LEED I(V) analyses.

An estimate of the expectation value of the R-factor for given numbers of data points and parameters has been proposed by J. B. Pendry [6.45]. He assumes that the I(V) curve consists of a superposition of Lorentzian curves of width $w = 2V_{0i}$, where V_{0i} is the optical potential describing the damping of the electron wave in the crystal and w is the HWHM (see Section 6.1.6.5). The separable peaks therefore are spaced on average by an energy interval of $4V_{0i}$ and thus the number of peaks can be estimated to be:

$$N = \frac{\Delta E}{4V_{0i}}, \quad (6.16)$$

where ΔE is the total energy range (the number N includes an estimate of the number of peaks caused by multiple scattering by assuming the maximum possible density of distinct peaks). The statistical error is then

$$RR = \frac{\text{var}R}{\bar{R}} \sim \sqrt{\frac{8V_{0i}}{\Delta E}}, \quad (6.17)$$

where $\text{var}R$ is the variance due to random errors in the experiment and \bar{R} is an average R-factor for uncorrelated data. The meaning of RR , a ‘double-reliability factor’, is that, for uncorrelated data, random errors will cause the R-factor value to be within the range $\bar{R}(1 \pm RR) = \bar{R} \pm \text{var}R$ with 68% probability. An R-factor value falling outside the range $\bar{R}(1 \pm 1.96RR) = \bar{R} \pm 1.96 \text{var}R$ has a probability of only 10% of being caused by random fluctuations, for uncorrelated data. A significance factor S can now be defined as

$$S = 1 - \frac{1}{\sqrt{2\pi}} \int_{-T}^{\infty} e^{-\frac{t^2}{2}} dt, \quad \text{where } T = \frac{\bar{R} - R}{RR}. \quad (6.18)$$

The significance factor S is the probability of a random fluctuation of an R-factor to have a value less than R and, by implication, $1 - S$ gives the probability that a structural choice producing the value R is correct [6.45].

It should be noted that V_{0i} is actually energy dependent and becomes relevant in LEED intensity calculations at lower energies, as was first pointed out by J. Rundgren [6.51]. The width of the peaks in the I(V) curves is approximately proportional to the damping parameter V_{0i} while the width of the Lorentzian peaks is approximately constant in k -space. V_{0i} is energy-dependent, smaller at low energies and larger at high energies, as shown in Figure 6.6 for the example of copper. The number of peaks calculated by Eq. (6.16) therefore depends on the energy range. I(V) curves in the low energy range exhibit a higher density of peaks.

The error estimate of Pendry is based on the expectation value for R and neglects the number of parameters and the correlation between parameters. It leads to relatively

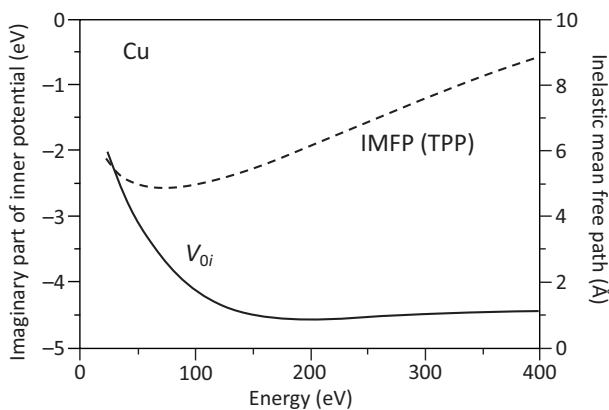


Figure 6.6 Inelastic mean free path (IMFP, dashed line), based on the TPP-2M equation of S. Tanuma, C. J. Powell and D. R. Penn [6.52] and imaginary part of the inner potential (V_{0i} , solid line) for copper. Reprinted with permission from [6.51] J. Rundgren, *Phys. Rev. B*, vol. 59, pp. 5106–5114, 1999. © (1999) by the American Physical Society.

large error bars. On the other hand, the more careful statistical error estimates based on counting statistics as used in X-ray analysis lead to very small error bars because systematic errors and the influence of approximations used in the theory are neglected. This is also the case in LEED, and Pendry's error estimate may compensate for this deficiency so that the relatively large error bars may be quite realistic; they are used in most LEED analyses.

An alternative approach for the error estimate based purely on experimental errors has been proposed by D. L. Adams [6.53]. This follows closely the usual practice in X-ray structure analysis, except that the experimental error cannot be determined from the counting statistics; instead it is derived from the standard deviation determined from repeated measurements and from symmetrically equivalent beams. The standard deviation σ_{hk} is defined for each beam as an average over all energy points:

$$\sigma_{hk} = \frac{1}{n_{hk}} \sum_{i=1}^{n_{hk}} \left[\frac{1}{n_s} \sum_{h'k'} \left(I_{hk,i}^{\text{ex}} - I_{h'k',i}^{\text{ex}} \right)^2 \right]^{1/2}. \quad (6.19)$$

Here, n_{hk} is the number of energy points in the beam (hk) and n_s is the number of beams $(h'k')$ that are symmetrically equivalent to beam (hk) or the number of independent measurements of the same beam. Adams takes the weighted R-factor comparing experimental and calculated intensities as used in X-ray analysis:

$$R = \frac{\sum_{hk,i} \left(\frac{I_{hk,i}^{\text{ex}} - cI_{hk,i}^{\text{th}}}{\sigma_{hk}} \right)^2}{\sum_{hk,i} \left(\frac{I_{hk,i}^{\text{ex}}}{\sigma_{hk}} \right)^2}. \quad (6.20)$$

The normalisation factor for the calculated intensities is defined as

$$c = \frac{\sum_{hk,i} \left(\frac{I_{hk,i}^{ex} \cdot I_{hk,i}^{th}}{\sigma_{hk}^2} \right)}{\sum_{hk,i} \left(\frac{I_{hk,i}^{th}}{\sigma_{hk}} \right)^2}. \quad (6.21)$$

To obtain the error estimate of a structure parameter, the number of independent data points is needed, which is estimated as the number of Bragg points in the energy range of each beam:

$$N = \sum_{h,k} \frac{\Delta k_{z,hk}(E_2) - \Delta k_{z,hk}(E_1)}{2\pi/d}, \quad (6.22)$$

where d is the interlayer distance in the substrate, while E_1 and E_2 span the energy range of the given beam. The standard deviation of a parameter p_i is then given by:

$$\sigma_i = \left(\frac{R_{\min} \varepsilon_{ii}}{N - m} \right), \quad (6.23)$$

where m is the number of parameters and ε_{ij} are the matrix elements of the inverse of the error matrix α . The error matrix is derived from the curvature of the R-factor near its minimum:

$$\varepsilon_{ij} = (\alpha^{-1})_{ij}, \quad (6.24)$$

with

$$\alpha_{ij} = \frac{1}{2} \left(\frac{\partial^2 R}{\partial p_i \partial p_j} \right) \cong \sum_{hk,n} \left(\frac{\partial I_{hk,n}^{th}}{\partial p_i} \right) \cdot \left(\frac{\partial I_{hk,n}^{th}}{\partial p_j} \right). \quad (6.25)$$

The error matrix can be used to check the correlation between parameters. If large off-diagonal terms occur, the error estimates determined from the diagonal terms may be unsafe. The pair correlation coefficients between two parameters i and j can be obtained from the error matrix by

$$P_{ij} = \frac{\varepsilon_{ij}}{\sqrt{\varepsilon_{ii}} \sqrt{\varepsilon_{jj}}}. \quad (6.26)$$

The error estimate proposed by Adams also neglects correlation between parameters. It gives the precision determined from the statistical analysis assuming independent parameters. The true accuracy may be much lower, due to insufficiencies of the multiple scattering theory and further experimental errors.

Another proposal for the error estimates in LEED I(V) analysis was made by C. B. Duke et al. [6.54] based on the χ^2 analysis commonly used in X-ray structure determination. They proposed to use each measured point on the I(V) curve as an independent measurement: this seems inappropriate due to the natural peak width and leads to error bars that are much too small, especially when a small step width in

energy has been chosen so that too many points in the I(V) curve are taken as independent whereas they are in reality not independent.

Since Pendry's R-factor R_P is established as standard in LEED I(V) analyses, its value is given in nearly all publications. While the error estimate and the RR-value as defined by Pendry do not consider experimental errors, these could be easily included, as follows. The standard deviation can be defined for each beam as proposed by Adams, Eq. (6.19), and a weighted R-factor based on the Y-function defined by Pendry could be used:

$$R_w = \frac{\sum_{hk,i} \left(\frac{Y_{hk,i}^{\text{ex}} - Y_{hk,i}^{\text{th}}}{\sigma_{hk}} \right)^2}{\sum_{hk,i} \left(\frac{Y_{hk,i}^{\text{ex}}}{\sigma_{hk}} \right)^2}. \quad (6.27)$$

The weights σ_{hk} for each beam, Eq. (6.19), are the standard deviations determined from repeated measurements and from symmetrically equivalent beams. Using this R-factor, the standard deviation for a parameter can be calculated from the error matrix (Eqs. (6.24) and (6.25)). The number of independent points in the I(V) curves is estimated as in Pendry's RR factor from V_{0i} (Eq. (6.16)). The precision determined in a more elaborate statistical analysis frequently underestimates the accuracy of the result but is comparable to the error given in X-ray analyses.

6.1.4 Optimum Energy Range

Clearly, a sufficiently large experimental data set is needed to determine the unknown parameters of a structure. The LEED I(V) measurement is usually made only at normal incidence, because this orientation is easily controlled and all beams having sufficient intensity are measured. Large 2D unit cells imply more parameters to be determined; they also produce a higher density of diffracted beams and therefore a larger amount of measurable intensities that approximately balances the number of parameters. At low temperatures the measurement may reach an upper energy of about 500–600 eV, beyond which intensities become too weak due to thermal effects and defects. At room temperature only a much smaller energy range can be measured.

The data set is not limited to normal incidence and can be extended to measurements at oblique incidence; however, this is rarely done. Off-normal incidence presents a significant disadvantage in the case of symmetrically equivalent domains producing coincident beams, which occur in most structures: LEED calculations must then be performed separately for each equivalent structural domain orientation and then averaged together (possibly with relative weights to be determined), since the incidence directions on different domains will no longer be equivalent. This complicates an automated search procedure considerably.

Redundancy of data, that is, measurement of more data than strictly necessary, is required to perform a reliable structure determination. We may compare the situation in X-ray structure analysis, where in single crystal structure analyses the overdetermination is defined as the number of reflections divided by the number of

Table 6.1 Examples of overdetermination. Each peak is assumed to provide two data points, namely its energy and its height

System	Data set	Overdetermination <i>n</i>
water on Fe ₃ O ₄ (001) [6.55]	≈ 110 peaks, 220 data points, 30 free parameters Fit by additional use of restraints (bond lengths)	≈ 7
Cl on Ru(0001) [6.56]	≈ 60 peaks, 120 data points, 10 free parameters	≈ 12
C ₆₀ on Ag(111) [6.57]	≈ 310 peaks, 620 data points, 15 free parameters	≈ 40
SO ₄ on Ag(111) [6.58]	≈ 180 peaks, 360 data points, 107 relevant parameters Substrate relaxation was checked in addition, leading to a total of 163 parameters	≈ 3.5

parameters. An overdetermination of 8 to 10 is recommended for publication in *Acta Crystallographica E*. For powder diffraction the number of peaks follows from the size of the unit cell and the angular range which has been measured. The angular range determines the resolution.

For LEED, the required energy range is not quite so clearly determined, since the number of free parameters depends strongly on the depth down to which substrate relaxations are considered. Depending on the size of the superstructure cell, the number of parameters is much enlarged if relaxations in several substrate layers are included in the analysis. Due to the strong damping of the electron wave the influence of the structural parameters in deeper layers is small and substrate relaxation is better studied by X-ray diffraction than by LEED. With LEED it is useless to refine parameters in layers deeper than about 1 nm, about twice the penetration depth. The data would be overfitted by unrealistic relaxations in the deeper substrate layers which are known to be bulklike. Nevertheless, one should check whether substrate relaxations down to that depth improve the agreement or not without unphysically large relaxations in deeper layers. Detectable substrate relaxations are frequently limited to one or two layers for the case of adsorbates on metals, whereas on oxides and other compounds the situation may be different.

We give some examples of overdetermination for LEED I(V) analyses in Table 6.1, showing that in most cases the number of independent data points is sufficient. The last example, a $(7\sqrt{3}\times\sqrt{3})R30^\circ$ structure of SO₄ on Ag(111), is marginally acceptable due to a large unit cell without symmetry.

6.1.5 Structure Analysis Methods

Nearly all quantitative structure analyses performed by LEED are obtained by the ‘trial and error’ method. One or more structural models are typically first derived from

the possible geometrical arrangements in the surface unit cell, the experimentally known coverage of adsorbate atoms, chemical knowledge of favourable bonding geometries, STM or AFM images, molecular vibration frequencies, prior model calculations and any other information available from other kinds of experiment or theory. These proposed trial models are then evaluated by I(V) calculations and refinement of the parameters, usually producing R-factors that differentiate between the trial models by quantifying their goodness of fit.

Various refinement procedures and search methods are in use in the different LEED computer programs. They can be divided into methods requiring the calculation of a derivative of the intensity with respect to the model parameter and derivative-free methods in connection with R-factors, described in Section 6.1.2. Both have advantages and disadvantages.

All optimisation methods have in common that they can become trapped in local minima and that they are then bound to a model. In that case, the starting model must be sufficiently close to the correct structure. How close must it be? A very rough estimate is that the atoms should be within a few hundredths of a nanometre, that is, a few tenths of an Ångström, from the correct positions. If all the atoms are poorly placed, it is often not possible to start the full simultaneous refinement of all parameters. One then tries to first refine single parameters or blocks of parameters, while keeping other parameters fixed, and to proceed stepwise in this way until in the final step all parameters can be freed and optimised together. For large structures in particular, a block refinement can be used, which however converges more slowly, or constraints can be used to move rigid groups of atoms or molecules in the structure. In any case, one must check that the same minimum is reached when starting with several different trial structures. The radius of convergence, that is, how far from the correct positions one may start an iterative search, is normally larger for simple structures (e.g., determination of the position of a single atom in the unit cell) if the major part of the starting model is correct. In general, many cycles of iteration steps are necessary to locate the true minimum of the R-factor.

We present in Sections 6.1.5.1 and 6.1.5.2 different methods which have been used, starting with local optimisation methods, also called refinement methods, and then global search methods.

6.1.5.1 Local Optimisation Methods

Least-Squares Refinement

In X-ray diffraction the main refinement procedure is the ‘least squares’ method, which requires the calculation of derivatives of the structure factors with respect to the structural parameters. With X-ray diffraction the calculation of derivatives can be done analytically. In the case of LEED this is not possible or not practical and the calculation must be done numerically [6.59]. Therefore, only minor advantages over derivative-free optimisation methods would remain. It would be helpful if approximations could be used for the calculation of derivatives.

A very efficient optimisation scheme is the so-called expansion method, which is routinely applied in many fields and is also the standard method used in X-ray

structure refinement. It is based on the minimisation of a fitting function which is usually the mean square deviation between experimental and theoretical data points. It requires the knowledge of the derivatives of the intensities with respect to the variable parameters. In its original form it works well near the minimum where the gradient is small, because it is based on a linear expansion of the intensities as a function of the variable parameters. Farther away from the minimum, the gradient methods usually work better. Therefore, a combination of both methods has been developed by D. W. Marquardt [6.60] and his approach has in fact become the standard method for optimisation in many fields. Detailed descriptions of the procedure can be found in most textbooks in X-ray crystallography (see for example [6.4]). With LEED this approach has been successfully applied in a number of structure analyses, for example: Ag(111)+(4×4)-O [6.61], Cu(111)+(3√3×3√3)R30°-TMB [6.46], α-Fe₂O₃(0001), α-Cr₂O₃(0001) [6.62], Fe₃O₄(001)+H₂O [6.55] and Ru(0001)+(√3×√3)R30°-Cl [6.56].

We briefly outline the expansion method in the following. The published programs for the expansion method allow the inclusion of a standard deviation for each data point. In the case of LEED, that would be the standard deviation for each beam, σ_{hk} . This quantity is mostly not available or not measured, so that $\sigma_{hk} = 1$ is used corresponding to an unweighted R-factor, R_u . We nevertheless include σ_{hk} in Eq. (6.28) to produce a weighted version, R_w , of the Pendry R-factor, R_P . Minimised is the mean square deviation between Pendry's Y -functions defined in Eq. (6.12), summed over beams and energies, with different beam weights given by σ_{hk} :

$$R_w = \frac{\sum_{hk,i} \left(\frac{Y_{hk,i}^{ex} - Y_{hk,i}^{th}}{\sigma_{hk}} \right)^2}{\sum_{hk,i} \left(\frac{Y_{hk,i}^{ex}}{\sigma_{hk}} \right)^2}. \quad (6.28)$$

The weights σ_{hk} are defined as the standard deviation for each beam,

$$\sigma_{hk} = \frac{1}{n_{hk}} \sum_{i=1}^{n_{hk}} \left[\frac{1}{n_s} \sum_{h'k'} \left(Y_{hk,i}^{ex} - Y_{h'k',i}^{ex} \right)^2 \right]^{\frac{1}{2}}, \quad (6.29)$$

and could be easily determined from the differences between n_s symmetrically equivalent beams which had been measured anyway. In practice this is rarely used and the unweighted R-factor is selected with $\sigma_{hk} = 1$.

A series expansion of the Y -function in terms of a change in parameters \mathbf{p}_j is used, $j = 1, N_p$, where N_p is the number of parameters to be optimised, \mathbf{p} is a vector in the parameter space and \mathbf{p}_0 denotes the set of start parameters. We can write:

$$Y_{hk,i}(\mathbf{p} + \Delta\mathbf{p}) = Y_{hk,i}(\mathbf{p}_0) + \sum_{j=1}^{N_p} \frac{\partial Y_{hk,i}(p_j)}{\partial p_j} \Delta p_j + \dots \quad (6.30)$$

The first two terms correspond to the linear expansion and are inserted into the minimum condition

$$\frac{\partial R}{\partial p_j} = 0, \quad (6.31)$$

where R stands for either R_w or $R_u = R_P$. This leads to a set of linear equations that defines the change Δp_j :

$$\sum_{hk,i} \left(\partial Y_{hk,i}^{ex} - \partial Y_{hk,i}^{th} - \sum_{j=1}^{N_p} \frac{\partial Y_{hk,i}^{th}}{\partial p_j} \Delta p_j \right) \frac{\partial Y_{hk,i}^{th}}{\partial p_m} = 0. \quad (6.32)$$

Eq. (6.32) can be written in short form as:

$$\beta_m = \sum_{j=1}^{N_p} \Delta p_j \alpha_{jm}, \quad (6.33)$$

with

$$\alpha_{jm} = \frac{1}{2} \left(\frac{\partial^2 R}{\partial p_j \partial p_m} \right) \cong \sum_{hk,i} \left(\frac{\partial Y_{hk,i}^{th}}{\partial p_j} \right) \left(\frac{\partial Y_{hk,i}^{th}}{\partial p_m} \right). \quad (6.34)$$

The new parameters $p_j + \Delta p_j$ are obtained by matrix inversion of Eq. (6.33) and the procedure is repeated until convergence is reached. The standard deviation of the i -th parameter is given by

$$\sigma_i = \sqrt{\frac{R_{\min} \varepsilon_{ii}}{N - m}}, \text{ with } \varepsilon_{ij} = (\alpha^{-1})_{ij}, \quad (6.35)$$

where m is the number of parameters and N the number of independent data points. The partial derivatives must be calculated numerically, or else approximately by, for example, tensor LEED. Replacing the coefficients α_{jm} by $\alpha_{jm}^0 = \alpha_{jm}(1 + \delta_{jm}\lambda)$ allows a continuous transition from a gradient-method-like behaviour (at large values of λ) to the expansion method (at small values of λ). The parameter λ is dynamically adjusted. Using the Y -function for comparison of experimental and calculated data as shown in Eq. (6.12), the expansion method is closely related to the linear tensor LEED method [6.63].

The numerical calculation of derivatives of the intensities with respect to the parameters to be optimised is time-consuming and requires approximations since an analytical solution is not practical. Tensor LEED is very efficient but is also an approximation. It shifts the position of an atom but leaves the wave field backscattered from the surrounding atoms unaltered. The optimisation with the expansion method therefore may not find the true minimum; it frequently stops in local minima and may have numerical problems when very small intensity differences occur.

A number of optimisation methods that do not require derivatives have been proposed. We briefly mention in the following some methods which were tried in earlier LEED studies; details of these approaches can be found in the Numerical Recipes by W. H. Press et al. [6.64].

Simplex Method

The simplex method [6.64] is among the simplest optimisation algorithms. It does not require derivatives at all but uses a ‘simplex’ (set of vertices) of $N + 1$ points in parameter space, if there are N parameters to fit. At each iteration step, the vertex with the highest R-factor is replaced by a new vertex guessed to provide a lower R-factor. The simplex method is very robust, but often slow: in test cases, it tends to be considerably slowed down by long, shallow, twisting valleys in the R-factor hypersurface.

Direction-Set Method

A more effective algorithm is the direction-set method [6.65], which minimises the R-factor along a set of independent directions which are updated as the search proceeds. The minimisation along each direction is done independently, by parabolic interpolation if the function is tested to be parabolic in the region of interest or by simple bracketing if such a test fails. In order to optimise the efficiency of this step, the algorithm updates the directions by trying to converge on a set of so-called conjugate directions, which are such that minimisation along one does not spoil the subsequent minimisation along another. As an example, if we consider minimising a positive, quadratic function, a possible set of conjugate directions (but not the only one) corresponds to the eigenvectors of the matrix \mathbf{A} defining the quadratic function, such as the long and short axes of elliptical contours. If these, say N , eigenvectors are identified, the problem is reduced to N one-dimensional independent minimisations, that is, one along each direction.

Rosenbrook Method

The Rosenbrook algorithm [6.66], as well as its modification described in W. H. Press et al. [6.64], is best used when the search has already reached the vicinity of a local minimum. It identifies a set of conjugate directions by repeatedly computing the Hessian matrix of the R-factor (the Hessian is the matrix of partial second derivatives) and by updating the set of conjugate directions to be the set of principal directions of the Hessian. This option returns the position of the minimum together with the principal directions and the corresponding curvatures of the R-factor at the minimum: these are also useful information for evaluating the uncertainties of the structural determination.

Hooke–Jeeves Method

The Hooke–Jeeves approach [6.65; 6.67] is a form of steepest-descent method [6.62]. It explores the local shape of the R-factor hypersurface in the immediate vicinity of a given structure and deduces from it the best direction in which to move in order to reduce the R-factor value. The search proceeds in that direction until the R-factor no longer diminishes. The scheme is then repeated from the new point reached in this manner. This scheme was employed in a LEED structural determination which used full-dynamical calculations for all R-factor evaluations needed in the process [6.68]. It could be considerably accelerated by applying tensor LEED or other methods.

Bounded Optimisation by Quadratic Approximation (BOBYQA)

The optimisation algorithm ‘BOBYQA’ was developed by M. J. D. Powell [6.69]. It is a derivative-free method to iteratively minimise a cost function (the R-factor in LEED) when upper and lower bounds for the parameters can be defined. The algorithm solves the problem using a trust region method that forms quadratic function models by interpolation. One new point is computed on each iteration, usually by solving a trust region sub-problem subject to the bound constraints or, alternatively, by choosing a point to replace an interpolation point so as to promote good linear independence in the interpolation conditions. The method has been found to locate safely the minimum R-factor region for a large number of parameters if the start model is within ≈ 0.03 nm for all geometrical parameters; an application has been described in R. Wyrwich et al. [6.58].

6.1.5.2 Global Search Methods

Global search methods are optimisation schemes in which the global minimum of the cost function is sought, as opposed to a local minimum. In the case of LEED this cost function is the R-factor hypersurface, which exhibits a high density of local minima and noise [6.70]. Optimisation algorithms like the least squares scheme or simplex method frequently get trapped in a local minimum and usually require a number of trials with different start parameters to reach a minimum which can be considered as global. However, even this is not guaranteed as the parameter space used in local optimisation algorithms is always limited. Global optimisation schemes therefore start with the full parameter space (or in practice at least a reasonably large parameter space) and should find the global minimum of the R-factor hypersurface (within reasonable limits). A global search may go beyond optimising *continuous* variables like atomic coordinates, thermal parameters and site occupancies: a global search may also include optimising so-called *discrete* or *categorical* variables, such as determining the chemical element or even the presence versus absence of atoms (e.g., when their surface coverage is uncertain or periodic vacancies are possible).

Various formulations of global optimisation have been developed and applied with diffraction methods and also in DFT calculations. They require an enormous number of models and therefore have not been applied in LEED to solve unknown structures; however, their applicability has been tested with known structures with a relatively small number of free parameters. With further speeding up of computing times, parallel computation and development of approximations in the multiple scattering calculation, these methods certainly have the potential of more general application. We shall describe three basically different approaches: simulated annealing (SA), genetic algorithms (GAs, also called evolutionary algorithms, EAs) and generalised pattern search (GPS). These methods had been applied in various fields, including some in X-ray diffraction where the large number of structure factor calculations is less of a burden than in LEED.

Simulated Annealing

P. J. Rous [6.70] was the first to apply simulated annealing (SA) to the search problem in LEED. He compared the computational cost with the number of free

parameters of the model and found a scaling relation of N^6 . The scaling behaviour, that is, the rate of increase of the computational effort with the number of parameters N , is an important factor since the method is hoped to be applicable to systems with a large number of unknown parameters N . This large number of model calculations prohibited the application to structures with more than a few free parameters. Simulated annealing starts with a model with randomly chosen parameters and allows a random increment for each parameter at each step. In the beginning the full parameter space is allowed for each parameter. Using the Metropolis criterion, if the cost function (i.e., the R-factor) has decreased after applying the increments, the move is accepted; an increase of the R-factor is also accepted with a probability determined by a Boltzmann factor controlled by an artificial temperature parameter. The temperature is gradually decreased during the process, analogous to the real annealing of crystals.

In the original SA algorithm used in LEED, a Gaussian function was selected for the probability to accept the step. The convergence of this procedure is very slow. The speed is increased if a Cauchy–Lorentz function is used instead of a Gaussian, which allows occasionally larger steps and a faster temperature decrease than the SA approach: the resulting scaling is an excellent N^1 , that is, simple proportionality of computational effort to number of parameters. This method is called fast simulated annealing (FSA) [6.71] and has become the most applied version of the algorithm. The broad wings of the Cauchy–Lorentz function allow a larger step toward a global minimum while the Gaussian function remains in a local minimum, as illustrated in Figure 6.7. Several variants with different statistical distributions are in use [6.72] but will not be discussed here. The number of model calculations can be substantially reduced when fast simulated annealing (FSA) is used, as was shown later by V. B. Nascimento et al. [6.73].

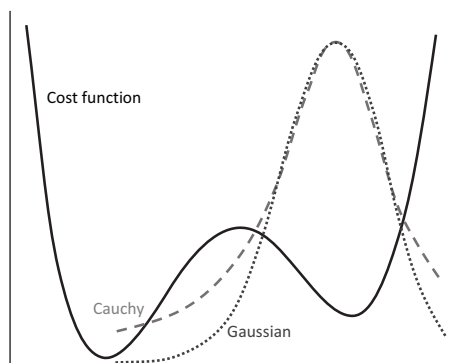


Figure 6.7 Comparison of a Cauchy probability density and a Gaussian probability density over an example cost function. The longer jumps enabled by the Cauchy probability density allow faster escape from local minima. Redrawn from [6.71] H. Szu and R. Hartley, *Phys. Lett. A*, vol. 122, pp. 157–162, 1987, with permission from Elsevier.

FSA and variants with further improvements are the most commonly used approaches in various fields. The effectiveness of the method in LEED, testing different statistics and generalised distribution functions, has been published by E. dos R. Correia et al. [6.74] and has been called ‘generalised simulated annealing’ (GSA). They found in a theory-to-theory comparison for 2–10 parameters a linear scaling behaviour of N^1 for the example of CdTe(110), as with FSA. The number of required LEED calculations is still enormous in simulated annealing algorithms so that this method has not been applied to solve unknown surface structures.

An approach that is related to simulated annealing was proposed by M. Kottcke and K. Heinz [6.75]. They start from random models and allow random moves of the atoms, but instead of using the Metropolis criterion of SA, they only accept new models with improved R-factors. To avoid getting trapped in local minima, they allow more distant moves with an R-factor-dependent Gaussian step distribution that is wider when the most recent R-factor is higher. Based on tensor LEED, the method can explore structures deviating from a certain preselected reference by atomic shifts, chemical occupation of lattice sites and both isotropic and anisotropic atomic vibrations. This automated optimisation scales as $N^{2.5}$, providing a compromise between global and local search methods. The method is more successful at locating the global minimum than other refinement algorithms but still needs several start structures and many iterations.

Genetic or Evolutionary Algorithms

A sophisticated class of algorithms to locate the global minimum of a cost function has been developed in other fields and is known as genetic or evolutionary algorithms (GAs or EAs). These are inspired by the evolution of biological systems which can be understood as an optimisation process. GAs have been widely applied in very different fields and technological problems.

GAs are based on computing the costs (i.e., R-factors in LEED) of a set of trial structures that form a ‘population’, in the terminology of this method. Each trial structure is characterised by its ‘gene’ or ‘chromosome’, that is, a list of its structural and non-structural parameters that are to be optimised; they are lined up as a string of digits, analogous to biological DNA. A GA proceeds by evolving the population of trial structures, which retains the same size as the starting population, from one ‘generation’ to the next. This evolution is biased toward increasing the quality of the members of the population and proceeds until the population contains a trial structure of sufficient quality (low enough R-factor). The initial generation of trial structures must be specified by the user, for example, it could be a set of structures deemed to be realistic, but it can also be a set of random structures: the global character of the search should find the correct structure in either case.

Creating a new generation of the population is performed concurrently by various schemes, primarily: mutation, that is, random change of one or more structural or non-structural parameters (or of digits within those parameters); ‘crossover’, that is,

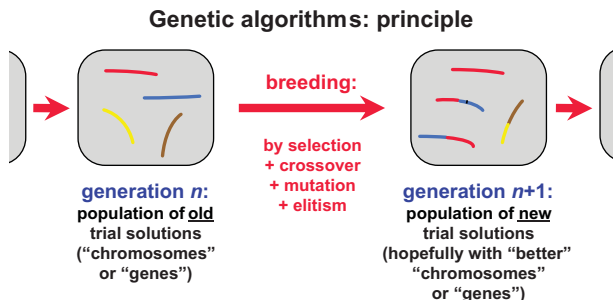


Figure 6.8 Schematic representation of the principle of typical genetic or evolutionary algorithms. A population is composed here of four trial solutions shown in different colours, where each coloured string contains all data defining a trial solution, like biological DNA. The population evolves by breeding from generation n to generation $n + 1$. Breeding occurs by first selecting some of the best trial solutions from generation n , then pairing these to generate new trial solutions for the next generation $n + 1$, by crossover (e.g., the new red/blue and blue/red mixed solutions created from the old red and blue solutions, as exemplified in Figure 6.9) or by mutation (e.g., by randomly changing a gene at the black spot in the new red/blue solution). Elitism can also be applied to allow one or more of the best old trial solutions to survive intact into the new generation (e.g., the red solution here).

intermixing structural features from two parent structures; and elitism, that is, survival of the best structures into the next generation. The breeding process, including crossover, is schematically illustrated in Figure 6.8. Crossover combines pairs of the ‘best’ trial structures in the population (i.e., structures having relatively better R-factors in LEED) to generate new trial structures: namely, the genes of a pair of so-called parents are mixed (essentially by cut and paste) to give new structures called ‘offspring’ or ‘children’. Figure 6.9 displays a typical flowchart of a GA in LEED, as well as one example of how crossover can be implemented.

A number of variants of GAs exist which differ in the strategy of selecting the offspring by mutation, crossover, etc. Evolutionary processes usually work faster than simulated annealing, as random steps are not used but the experience from previous calculations is included more constructively: for example, while simulated annealing mainly rejects ‘bad’ solutions, GAs incorporate details of ‘better’ solutions into new trial structures. The number of LEED calculations required until a minimum of the R-factor is reached remains a limiting factor with GAs, but the method is ideal for parallel computation and, for this reason, it is also more promising than simulated annealing. Genetic algorithms are robust, not very sensitive to noise; they also work well with highly correlated parameters which may trap other optimisation schemes in local minima.

Genetic algorithms were first applied to LEED by R. Döll and M. A. Van Hove [6.77]. Later the method was also applied to photoelectron diffraction [6.78]. Its scaling behaviour has been tested by M. L. Viana et al. [6.79] for the model systems

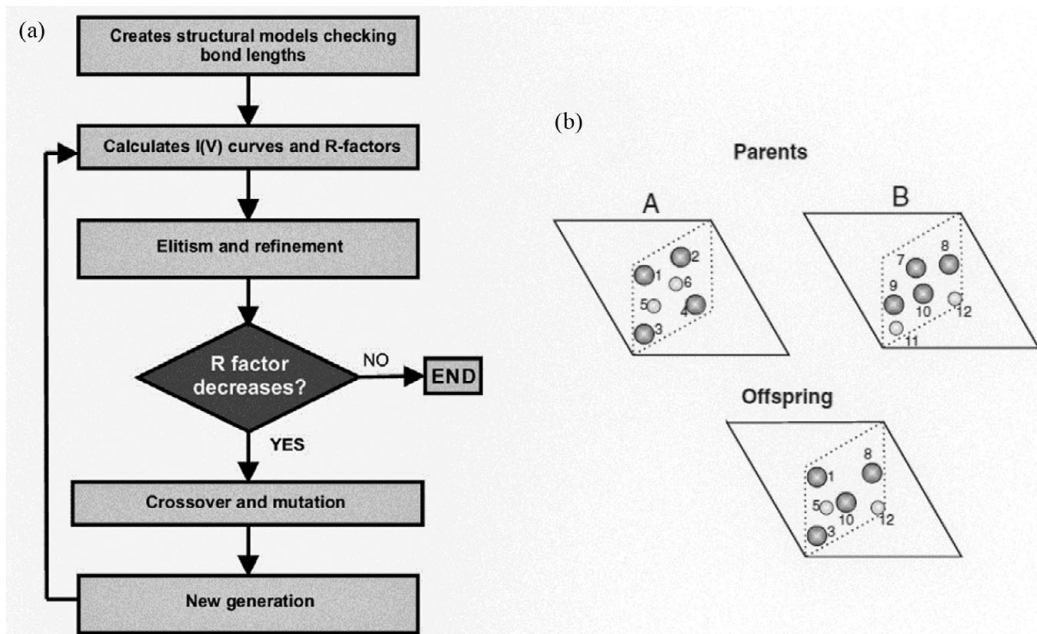


Figure 6.9 (a) Schematic flowchart of a GA algorithm for LEED. (b) Schematic representation of one type of crossover operation within a 2-D surface unit cell from parent structures A and B to a new Offspring structure (exemplifying the crossover shown in Figure 6.8): atoms to the left (at positions 1, 3, 5) inherit their coordinates from parent A, while atoms to the right (at positions 8, 10, 12) inherit their coordinates from parent B. © IOP Publishing. All rights reserved. Reproduced with permission from [6.76] M. L. Viana, D. D. dos Reis, E. A. Soares, M. A. Van Hove, W. Moritz and V. E. de Carvalho, *J. Phys.: Condens. Matter*, vol. 26, p. 225005, 2014; permission conveyed through Copyright Clearance Center, Inc.

$\text{Ni}(111)+(\sqrt{3}\times\sqrt{3})\text{R}30^\circ-\text{Sn}$, $\text{InSb}(110)$ and $\text{CdTe}(110)$ using 5 to 16 structural and non-structural parameters. For test cases with a relatively small number of parameters a scaling proportional to $N^{1.6}$ was found in R. Döll and M. A. Van Hove [6.77] and $N^{1.3}$ to $N^{1.7}$ in M. L. Viana et al. [6.79], depending on the difficulty to locate a minimum of the R-factor. Further reduction of the computational effort can be achieved by including symmetry and bond length restrictions in the procedure to generate offspring. Models are then immediately rejected before being subjected to a costly LEED calculation if they do not fulfil minimum bond length requirements or given symmetry conditions. The method is called ‘novel genetic algorithm for LEED’ (NGA-LEED) [6.76] and also differs from the previous application of genetic algorithms by a local refinement step applied to certain intermediate structures to accelerate the search. The atomic positions are located on grid points because the location of a global minimum can then be performed faster with a smaller number of possible structure models and the refinement of parameters can be performed in a final

step within the near vicinity of the determined minimum. As a result, the computational effort could be drastically reduced. The method was tested for the previously solved structure of Ag(100)+(4×4)–O and Au(110)–(1×2) using experimental data.

Other variants of evolutionary processes are also very promising. These include differential evolution (DE) [6.80] and covariance matrix adaptation evolutionary strategy (CMA-ES) [6.81]. Differential evolution [6.80] is a rather simple but effective population-based search scheme. It starts with a population of P individuals. Each individual is characterised by a vector consisting of its N structural parameters. The value of P is recommended to be about 5 to 10 times the number of free parameters. The start population is randomly chosen within the full parameter space; no start model needs to be defined. The next generations are produced by mutation, crossover, etc., as in GAs, but the algorithm is quite different to that used in GAs. In the mutation step a weighted difference between two arbitrarily chosen individuals of the population is added to a third arbitrarily chosen individual, thus defining a new individual. In the next step, called crossover, a new population is formed by mixing the components of the new individual with another vector, the target vector. The target vector is initially randomly chosen. The LEED calculation is now performed for the new population and the selection process is the following: if the R-factor for an individual has decreased, this individual then becomes the new target vector, otherwise the old target vector remains. The process is iterated until no further decrease of the R-factor is obtained. Two factors influence this process: one is the factor occurring in the mutation step which defines the weighted difference between two arbitrarily chosen individuals; the other factor occurs in the crossover step and determines the mixing with the target vector. The performance of the optimisation process is determined by the choice of these two parameters. The best choice must be checked by a LEED calculation and depends on the number of parameters and the surface structure. The performance of DE has been investigated by V. B. Nascimento and E. W. Plummer [6.82] for the case of BaTiO₃(100), where they found a scaling behaviour of $N^{1.47}$ for up to 12 free structural parameters. These results show that DE is one of the most promising methods for global optimisation in LEED.

The other variant, the covariance matrix adaptation evolutionary strategy (CMA-ES), is also a population-based method. However, in contrast to GAs, the crossover step is omitted and new individuals are generated solely by mutation. The R-factor hypersurface in the search space is determined in each generation from the R-factors of all individuals in the population. New individuals for the next generation are derived from the multi-variate normal distribution which is given by the covariance matrix. The normal distribution is adapted to the R-factor hypersurface. This means that the choice of new parameters for the individuals of the new population is determined by the shape of the R-factor hypersurface. The speed with which a minimum is reached can be expected to be higher than with GAs, but the process may be trapped in a local minimum of the R-factor hypersurface. The parameters of the CMA-ES algorithm are the numbers of parents l and offspring k , with $k > l$, as well as the initial standard deviations of the algorithm's normal distributions, which also define the distribution of individuals in the initial population.

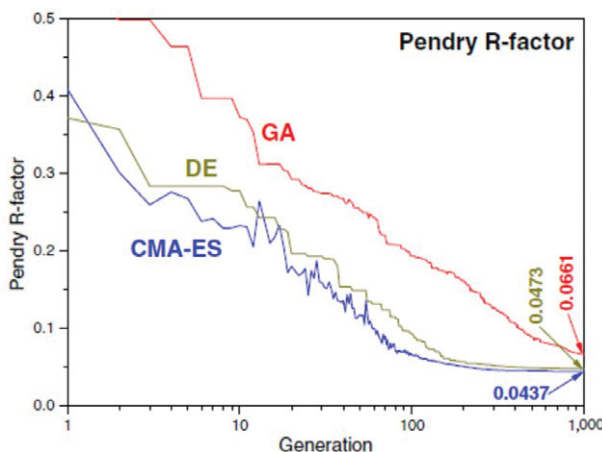


Figure 6.10 Pendry R-factor of the fittest individual as a function of the number of generations for covariance matrix adaptation evolutionary strategy (CMA-ES), differential evolution (DE) and a genetic algorithm (GA). Reprinted from [6.48] E. Primorac, H. Kuhlenbeck and H.-J. Freund, *Surf. Sci.*, vol. 649, pp. 90–100, 2016, with permission from Elsevier.

Different global search methods have been tested and compared by E. Primorac et al. [6.48] for MoO₃ monolayers on Au(111). The results were also compared to a tensor LEED analysis. Three different population-based search methods were employed: CMA-ES, DE and a real-valued GA. The GA is called real-valued because the genome consists of real numbers in the present case. The I(V) curve computations for the individuals of the population were performed in parallel on a multi-processor system which significantly reduced the computation time (but not the overall computational effort). A reduction of the computational effort was achieved by requiring fulfilment of symmetry and of minimum bond length constraints for the models. A total of 28 parameters were optimised, with 24 structural parameters which were refined by the evolutionary processes. The results are shown in Figure 6.10.

The parameters determining the performance of the different algorithms, the convergence radius and the computational effort have been carefully tested. The CMA-ES and DE algorithms turned out to be faster than the GA method and led to a lower R-factor after a certain number of generations. The evolutionary processes DE and CMA-ES seem to be better suited in the last stage of the refinement where very small shifts of the parameters occur. In the CMA-ES method this is probably due to taking into account the local geometry of the R-factor hypersurface. This is not the case in GA, while in DE it is probably indirectly included by the choice of the new target vector in each generation. In the final stage of the refinement, the GA method therefore works more slowly. For CMA-ES several runs with different start models were performed; one run led to the lowest R-factor, showing that the global minimum was reached with an excellent agreement. For comparison, the tensor LEED method leads much faster to a local minimum but, being an approximation, typically yields a

larger R-factor. It is therefore useful to combine a relatively coarse global search to identify the probable global minimum region (using, e.g., genetic algorithms) with a fast refinement step to optimise the details of the global minimum itself (using, e.g., tensor LEED); in some cases, the coarse search may suggest several candidates for the global minimum: these can then be distinguished by refinement.

Discrete Variables and Generalised Pattern Search

In optimisation problems like LEED, it may be necessary to optimise not only continuous variables, but also discrete variables: these are often called ‘categorical’ variables, as they may take only two or a few distinct values, for example, the chemical identities of atoms in a compound system or their presence versus absence. For instance, an adsorbate atom may or may not substitute for a substrate atom which is expelled, so both options may need to be tested. Also, the coverage of an adsorbate may be uncertain, which may be viewed as presence versus absence of such atoms at specific locations, while vacancies may also occur in a substrate. As a further example, a metallic surface alloy may distribute its component atoms differently from the bulk arrangement. Discrete variables preclude differentiation and thus optimisation by steepest descent or similar methods.

Many of the global search methods described in the preceding paragraphs can be generalised to include optimisation of discrete variables, if they do not rely on derivatives of the cost function (R-factor). We here discuss a method that is particularly suited to handle discrete variables at the same time as continuous variables (such as atomic coordinates): the generalised pattern search (GPS) method in its ‘mixed variables’ version [6.83; 6.84], which is also well adapted for imposing restrictions such as symmetry, bond length and coordination constraints; it is a member of a wider class of generating set search (GSS) methods [6.85]. The basic GPS strategy for continuous variables is simple to explain using a 2-D example, with four compass directions (north, east, south and west): starting from one assumed trial structure, for each variable, the procedure steps by a pre-set amount Δ_0 in the four compass directions until the cost function is reduced and moves the trial structure to that better position; otherwise the step length Δ_0 is halved; these steps are repeated until convergence. For discrete variables, some of their properties must be provided by the user: these properties can vary significantly from one type of application to the next, so the user must select an appropriate method within the code [6.86].

The application of GPS to LEED was tested for a complex ordered surface alloy structure, Ni(100)+(5×5)-Li [6.83]. This structure results from adsorption of Li on Ni (100). The surface structure is illustrated in Figure 6.11, where panels (a–d) show the best fit among the 45 proposed models shown at left, based on prior separate local optimisations by tensor LEED [6.87]. The 45 proposed models differ in the occupation of bulk-like Ni(100) lattice sites with either Ni atoms or Li atoms or neither (i.e., vacancies). These models illustrate the situation where there is uncertainty about the adsorption coverage (density of adsorbate atoms), the penetration of adsorbates into the substrate, the relocation of substrate atoms (substrate reconstruction), the presence of vacancies and even the number of layers affected. Taking as an example only the

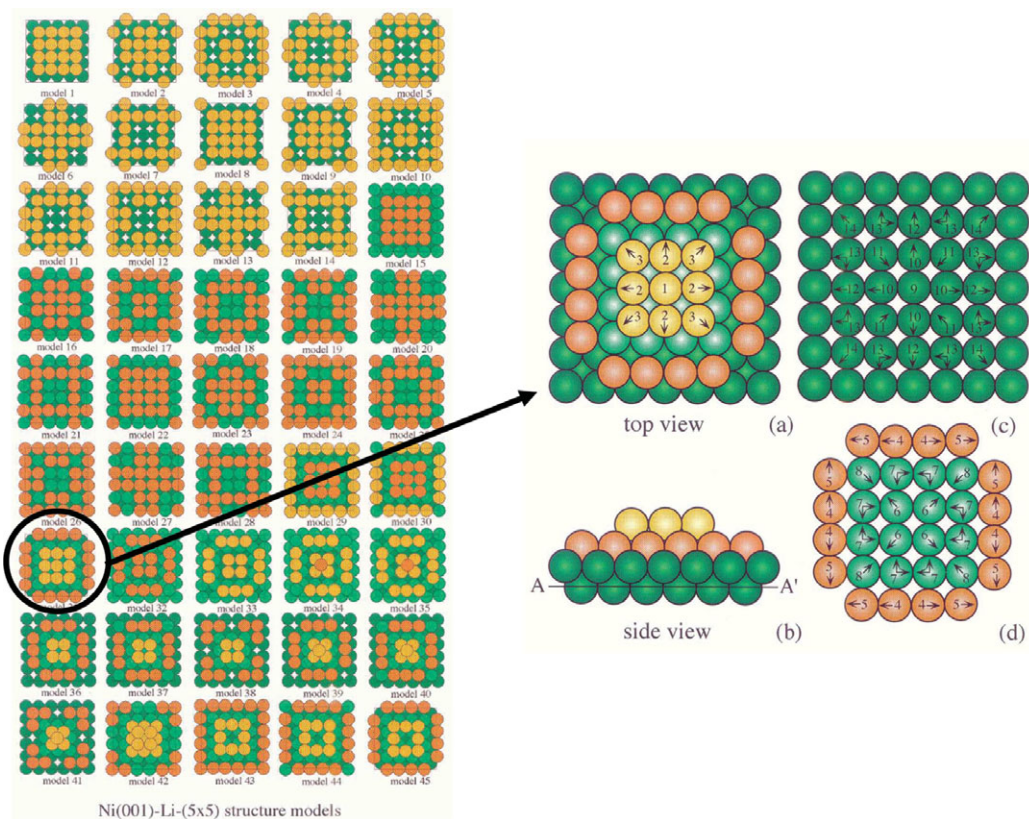


Figure 6.11 The Ni(100)+(5×5)-Li surface formed by adding Li atoms on a Ni surface. The 45 small panels on the left are structure models built from physical intuition. In these models, the Ni atoms (green) and Li atoms (orange and yellow) are distributed in various arrangements in 1, 2 or 3 layers, with varying numbers of Ni and Li in the (5×5) unit cell. Panels (a) and (b) detail structure model 31, while panels (c) and (d) represent its second and third outermost layers (the first outermost layer is shown in yellow in (a) and (b)): this model has the lowest R-factor among these 45 models, based on prior separate tensor LEED optimisations. Adapted from [6.87] H. Jiang, S. Mizuno and H. Tochihara, *Surf. Sci.*, vol. 380, pp. L506–L512, 1997, with permission from Elsevier.

previously best-fit structure (model 31 highlighted in Figure 6.11(a–d)) and assuming the full p4m point group symmetry of the Ni(100) substrate, there are 14 inequivalent atoms in the cell in the outermost 3 layers (numbered in the figure). In this case, we thus need to optimise 28 continuous structural variables ($3 \times 14 = 42$, but symmetry reduces this number) and 14 discrete variables (each of these atoms can be either Ni or Li). This count ignores thermal parameters as well as the inevitable adjustable inner potential, V_0 .

The performance of the GPS method was first compared with that of GAs starting with the model 31 presented in the last paragraph, without optimising the chemical elements (both methods utilise tensor LEED to determine R-factors). A feature of GAs is that their breeding procedures normally create numerous trial structures that are physically totally

unrealistic unless suitable constraints are imposed, such as limits on acceptable bond lengths. Therefore, only small atomic relaxations (± 0.04 nm, i.e., ± 0.4 Å) from the best known solution were allowed in the search with GA. GPS produces far fewer such invalid structures and found an improved solution ($R_P = 0.12$) at around 600 function evaluations, while the GA found the model 31 ($R_P = 0.24$) only at around 2,400 function evaluations. Next, atomic positions were fixed, while chemical elements could change. Using the notation 11111222222222 (1 = Li, 2 = Ni) for the 14 chemical identities of the 14 numbered atoms in model 31 (see Figure 6.11), a search was started with the choice 11111122211122 (i.e., some Ni atoms were substituted by Li atoms). GA now needed 280 function evaluations to obtain model 31, while GPS needed only 49 function evaluations. (GPS actually found an improved solution at 135 function evaluations, again with $R_P \sim 0.12$: these solutions with $R_P \sim 0.12$ are actually invalid, as they were found to have an unphysical inner potential determined by the tensor LEED code and not by the GPS procedure; it would be easy to constrain the inner potential within GPS.) Using 20 random initial chemical guesses, GPS reached the same minimum $R_P \sim 0.12$, with an average of 152 function evaluations. Optimising simultaneously the continuous and discrete variables led GPS to a slightly improved $R_P = 0.23$ compared with the prior best fit of model 31 at $R_P = 0.24$, with the largest difference of 0.013 nm = 0.13 Å from the previous best atomic positions [6.87].

6.1.6 Influence of Non-structural Parameters on the Structure Determined by LEED

Several non-structural parameters enter the LEED I(V) analysis and are discussed in this section:

- The scattering potential model. The spherically symmetric muffin-tin (MT) model is most commonly used together with phase shifts.
- The inner potential $V_0(E)$ and its energy dependence. The parameter V_0 , often called muffin-tin zero (V_{MTZ}) or muffin-tin constant, is normally taken to be isotropic (independent of the direction of propagation) and often independent of energy; it may vary from one atomic layer to another, especially for overlayers.
- The inelastic mean free path (IMFP) or damping constant is normally given by the imaginary part of the inner potential $V_{0i}(E)$, also called optical potential, and its energy dependence. The damping of the electron wave inside the crystal is usually approximated by the single isotropic parameter V_{0i} , which is sometimes taken as energy dependent. It leads inside the crystal to a complex energy $E + V_0 + iV_{0i}$ and complex wave vectors \mathbf{k} (see also Section 5.1).

The main other non-structural parameters in LEED calculations are the atomic displacement parameters (ADP) which describe displacements from the average atomic positions due to thermal motion and static defects. Their influence on the LEED intensities cannot be neglected and is routinely included in most LEED I(V) analyses by simple isotropic displacements in a Debye model. The theory is described in Section 5.5 for more general cases, in particular for anisotropic displacements.

We investigate here the influence of the potential model and the inner potential. These parameters are usually considered to be less important for the structure analysis, so that frequently average values are used. This is certainly justified when only the structure model must be identified, where an average accuracy of 0.005–0.01 nm (0.05–0.1 Å) is sufficient.

In many cases, however, a higher structural accuracy would be desirable. For example, an important part of quantitative LEED investigations is undertaken for studying catalytic reactions on surfaces. The change of molecular configurations and bond lengths in the adsorbed state compared to the free molecule is of great importance for understanding the reaction. An accuracy of bond lengths in the order of 0.0001 to 0.001 nm (0.001–0.01 Å) would then be required. Such accuracy can be obtained in 3-D X-ray analysis but is not standard in surface studies, including in surface studies by X-ray diffraction.

There is room for improvements in the calculation of LEED intensities in the areas of phase shift calculation and, as mentioned in Sections 5.5 and 6.1.5.2, in anisotropic atomic displacements. Improved calculation of phase shifts is discussed in this section. Their influence is particularly important in the low energy range. Although the muffin-tin model is usually considered to be sufficient in LEED, it may actually be the largest source of theoretical inaccuracy. In DFT calculations, more sophisticated full potential models are required in order to achieve better approximations for the Coulomb potential and the exchange-correlation terms than is possible with a simple muffin-tin approximation, since DFT deals with electrons at lower energies than LEED; see for example a review by K. Schwarz [6.88]. In LEED, higher energies in the range of about 20–500 eV are used, where the LEED electrons are scattered mainly by the Coulomb potential of the atomic cores. The core potential is screened by the bound electrons and therefore depends also on the surrounding atoms. The different approximations used to describe the crystal potential therefore influence the LEED I(V) curves and the accuracy of the structure analysis. It is often observed that excellent agreement between experimental and calculated LEED intensities and small error bars can be obtained for metals with close packed structures. However, for covalent structures and compounds like oxides the R-factors and the error bars are usually larger. This indicates that the muffin-tin model and the phase shift calculation are less appropriate for these structures and leave room for improvement. We first briefly review the development of the construction of the crystal potential and the phase shift calculation.

A note on terminology is needed here. In the relevant literature, the term inner potential is often used interchangeably with muffin-tin zero and muffin-tin constant; these terms are also used in Section 5.2, where the muffin-tin model is illustrated in Figure 5.3. These terms then indicate a spatially constant potential between atomic muffin-tin potentials, although different constant values may apply in different layers, as shown in Figure 5.3. In many publications, however, inner potential refers to the average potential of an electron in a crystal, including the average over the atomic cores (this inner potential can be measured, for example, as an energy shift of Bragg peaks in LEED, although this only gives a very approximate and energy-independent

value). In this section, the inner potential $V_0(E)$ will instead designate the spatially constant interstitial potential, which is a theoretical construct that cannot be directly measured; it is referenced to the vacuum level that exists infinitely far from the surface. In Sections 6.1.6.1 and 6.1.6.2, the inner potential V_0 and the muffin-tin zero V_{MTZ} are equivalent, that is, $V_0 = V_{MTZ}$; they may depend on energy, but most LEED calculations have kept them independent of energy. However, in Section 6.1.6.3, while the muffin-tin zero V_{MTZ} will be independent of energy and identical to the vacuum level, the inner potential $V_0(E) = V_{XC}(E)$ will consist of the energy dependent exchange-correlation energy; $V_{XC}(E)$ vanishes at very large energies, where therefore $V_0(\infty) = V_{MTZ}$. In addition, in all cases in LEED, the electron energies are shifted rigidly (by the same constant amount for all potentials or I(V) curves) to best fit the experiment, because the potential models do not properly include other surface-specific effects such as the work function change (due to surface dipoles resulting from spill-over of bound electrons into the vacuum or charge transfer between adsorbate and substrate), which gives rise to the image potential shown in Figure 5.3.

6.1.6.1 The Conventional Muffin-Tin Model

In the multiple scattering theory of LEED, the muffin-tin (MT) model is commonly used to describe the scattering properties of the atoms. The model uses a spherically symmetric potential for each atom and the scattering is described in spherical waves. The phase shifts of the spherical waves are calculated and then enter the multiple scattering theory as parameters, similar to atomic form factors in X-ray diffraction. A short description is given in Section 5.2. The elastic electron–atom scattering theory and scattering phase shift codes used for LEED emanate from the survey ‘Augmented Plane Wave Method’ by T. L. Loucks [6.89]. From the electron density of the atomic orbitals, the radial spherically symmetric atom potential $V(r)$ of the free atom is calculated for $0 \leq r \leq \infty$, where $V(\infty)$ is taken as zero. To obtain a spherically symmetric potential for one atom after superposition of the potentials from the surrounding atoms, the procedure proposed by L. F. Mattheiss [6.90] is used. In this method the potentials of the neighbouring atoms are expanded in spherical harmonics with the central atom as origin. Only the $l = 0$ term is taken to obtain spherical symmetry. A complete crystal potential comprises MT potentials where nearest neighbour MT spheres approximately touch one another and MT potentials are approximately continuous with a constant muffin-tin zero between the MT spheres, as illustrated in Figure 5.3. In close-packed elemental solids, compounds and adsorbates the crystal potential may be discontinuous, as steps can occur between the different MT spheres and the constant inner potential in the interstitial region; however, such steps are unrealistic and should be minimised, as discussed further in Sections 6.1.6.2 and 6.1.6.3.

The phase shift calculation via the MT potential usually proceeds in three steps:

- Calculation of the electron charge density of the free atom.
- Calculation of the free-atom potential by radial integration of the Poisson equation and construction of the muffin-tin potential by taking the spherically symmetric part of the superposition from the surrounding free atom potentials.

- Calculation of the phase shifts by integration of the non-relativistic Schrödinger equation or the relativistic Dirac equation with the spherically symmetric potential.

In the first step, the electron density of the free atom is calculated. Either the non-relativistic or the relativistic Hartree–Fock equations are solved for the self-consistent atomic orbitals (relativistic effects become important in heavier elements). Some computer programs require input of the atomic orbital structure; other programs require only the nuclear charge to identify the atom: then a table of the orbital structure of the ground state of all atoms is included in the program.

In the second step, using the electron density of the atomic orbitals, the radial atom potential $V(r)$ of the free atom is calculated by integrating the Poisson equation. The part of the electron charge that is absent from the muffin-tin spheres is distributed in the interstitial region and assumed to be spatially constant. Since the early days of LEED, the inner potential has usually been assumed to be independent of energy and of propagation direction. The value of the inner potential is usually determined by fitting to the experimental curves.

In the third step, the Schrödinger equation or the Dirac equation is radially integrated up to a MT radius. For the earliest LEED calculations, the MUFPOT code developed by J. B. Pendry et al. [6.91] was often used; similar codes were developed by other groups. More recently the phase shift code package provided by A. Barbieri and M. A. Van Hove [6.92] has been frequently used to generate phase shifts.

Although the procedure described here has been applied successfully in many structure analyses by LEED, there remain some problems in the construction of the crystal potential. The principal problem is that for structures with *covalent* bonds the MT potential is less appropriate, since for these the charge distributions within and between atoms deviate relatively more from spherical symmetry or constant interstitial values: properly, this would require a ‘full potential’ LEED calculation (with in particular non-spherically symmetric atomic potentials and a non-constant inner potential, as described in Section 5.2.1 and references [5.6–5.9]). Such calculations, however, would be computationally complex and onerous, especially during a structural optimisation process that would require updating the potential. Nevertheless, the MT model appears to be capable of producing a positional accuracy of at least 0.01 nm (0.1 Å), particularly if low electron energies are avoided; the most recent step-free MT model described in Section 6.1.6.3 delivers a positional accuracy of about 0.002 nm (0.02 Å).

Furthermore, within the MT model, the proper choice of the MT radii has also been problematic in many cases and can be improved, except for elemental metals with close packed structures where the midpoints between nearest neighbours define the MT radius (ignoring the usually small surface relaxations of atomic positions). For non-metallic compounds like oxides, for compounds with covalent bonds and for molecular structures, the choice of half the nearest-neighbour distance for the definition of the MT radius leads to a poor description of the electron density in the interstitial regions and in the outer parts of the MT spheres. The standard prescription for the construction of the MT potential generates artificial steps at the MT radius

between the potential within the spheres and the MT zero. A continuous potential would be more realistic.

A frequent question is how to treat ionic compounds. One aspect is whether published ionic radii are appropriate in the MT model. Such ionic radii are used qualitatively to classify structures of ionic compounds like oxides and halides but were not designed to describe electron–ion scattering and thus cannot be assumed to be appropriate, and indeed are questionable, as reported in the following paragraphs. However, ionic radii are useful to estimate interatomic distances in compounds where the structure is not yet known. Another aspect is the long-range electrostatic electron–ion interaction in an ionic lattice. To estimate this interaction, a Madelung sum over the ionic lattice is used, analogous to the Madelung sum used to obtain the lattice energy in ionic solids.

In X-ray crystallography, atomic form factors are used for neutral atoms and for ions, justified by the fact that the scattering factors for X-rays are derived from the number of electrons assigned to a neutral atom or an ion. However, for electron diffraction the situation is less clear. Electrons are mainly scattered by the core potential which is screened by the valence electron density of the atoms or ions, and ionic radii do not seem appropriate to define MT radii. We here briefly describe the LEED results obtained in the past for ionic structures to illustrate the more complex situation. In an early LEED study of the MgO(100) surface, C. G. Kinniburgh [6.93] investigated several potential models and MT radii, with the result that the MT radius had the largest effect on the LEED intensities. The comparison of I(V) curves showed a best fit with equal radii for both Mg^{2+} and O^{2-} ions, while ionic and neutral potentials gave similar agreement with experiment. A subsequent study of the NiO(100) surface by C. G. Kinniburgh and J. A. Walker [6.94] came to a similar conclusion, while finding that an ionic potential gave slightly better agreement with experiment than a neutral potential. These studies were based on a qualitative comparison of experimental and calculated I(V) curves rather than on R-factors. In later LEED studies of adsorbate layers on metal substrates, where I(V) curves were quantitatively compared by an R-factor, MT radii of the adsorbates were mostly derived from neutral atoms. In subsequent LEED studies of metal oxide surfaces and other ionic compounds, the best approach to the phase shift calculation remained an open question.

In a study of $TiO_2(110)$ surfaces [6.95], the charge transfer between metal and oxygen ions was approximated by using the ground state electron density of bulk TiO_2 obtained from DFT calculations. The MT radii derived from the electron density were approximately equal and about 0.1 nm (1 Å) for both ions; these corresponded to neither atomic nor ionic radii. The LEED I(V) analysis with phase shifts calculated using these MT radii led to a significant improvement of the agreement of the I(V) curves with an R-factor $R_P = 0.29$. The best R-factor obtained with phase shifts calculated from neutral atoms and an altered occupation of atomic states to simulate ionic potentials was about $R_P = 0.6$. The structural results, however, were very similar, with the largest difference of about 0.01 nm (0.1 Å) in the coordinates of an oxygen atom. However, a LEED I(V) analysis of another TiO_2 modification, brookite,

$\text{TiO}_2(011)-(1\times 2)$, did not find such a large improvement with phase shifts derived from DFT calculations [6.96]. Only small differences in R-factors and structural parameters were found between the results obtained from neutral atoms with symmetrisation by the Mattheiss procedure, compared with using phase shifts derived from self-consistently calculated electron densities.

The presence of potential steps between muffin-tin spheres and inner potential is conceptually not satisfactory; nonetheless, they were present in nearly all LEED I(V) calculations performed so far. It is often suggested that such steps would lead to resonances in the electron wave functions, since electrons could backscatter multiple times between a nucleus and such a nearby potential step. However, this is a misconception, since these potential steps are actually not included as scatterers in the usual LEED theory: only the scattering factors via the phase shifts enter the multiple scattering theory. The electron wave functions are not calculated by solution of the Schrödinger equation for the full crystal potential as required in DFT calculations. Nevertheless, the steps perturb the integration of the Dirac or Schrödinger equation in the calculation of the phase shifts, and the phase shifts export perturbations into the multiple scattering calculation.

The potential steps between vacuum and atomic layers, as well as between inequivalent atomic layers, are normally ignored in the theory, except for their refraction effect, so that resonances in the scattering between atomic layers and potential steps are excluded. This neglect is justified by the fact that a smooth step causes much less reflection than an abrupt step. The potential steps in the MT model have some influence on the LEED I(V) curves because the energy of the electrons is different on both sides of a step, causing changes in kinetic energy and thus also changes in wavelength and propagation direction.

6.1.6.2 An Improved Muffin-Tin Model

To overcome the problem of steps in the MT potential model, an important improvement was introduced by J. Rundgren [6.97; 6.98]: he used MT spheres with pre-assigned core level shifts and optimised MT radii in order to minimise steps to the interstitial inner potential at the MT radii. Mattheiss' superposition potential was combined with the Hedin–Lundqvist local density functional exchange-correlation potential $V_{\text{xc}}(E)$ [6.99; 6.100] to form a total potential for the elastic electron–atom scattering. The energy of the scattered electron inside the solid is $E - V_0(E)$. The MT radii are optimised by the differential evolution (DE) method and then become energy dependent through the energy dependence of the exchange-correlation potential. The potential step between the MT spheres and the MT zero is minimised by coordinated shifts of the MT potentials and optimisation of MT radii. Optimisation leads to steps of the order of 0.1 eV between MT spheres and MT zero. Unfortunately, the resulting MT radii and inner potential depend on incident energy, while in principle the MT radii should be independent of the energy of the incident electron.

V. B. Nascimento et al. [6.101] were the first to apply optimised MT radii in a LEED I(V) analysis, for the $\text{Ca}_{1.5}\text{Sr}_{0.5}\text{RuO}_4(001)$ surface. They applied a number of different methods to calculate the potentials and the MT radii, including charge

densities obtained from DFT calculations and also charge densities obtained from a relativistic Hartree–Fock calculation for neutral atoms. Interestingly, they observed undulations in the phase shifts as a function of energy due to energy dependent steps in the MT potential when calculated according to the Mattheiss procedure, while smooth phase shift curves were produced with optimised MT radii. They also applied an energy dependent imaginary part of the inner potential, as proposed by J. Rundgren [6.51]. Numerical data for the inelastic mean free path (IMFP) are available from the National Institute of Standards and Technology (NIST) [6.102]. The relation between the IMFP and the optical potential is described in Section 6.1.6.3 and further references can be found there. The results showed a significant improvement of the R-factor compared to previously used phase shifts [6.101]. The structural results agreed in this case within error estimates with previous results and reduced those error estimates significantly. Phase shifts obtained from optimised MT radii were also used in a number of further LEED I(V) analyses, of which some are mentioned here without intending to give a complete list, for example the studies of: epitaxial thin films of $\text{LaNiO}_3(001)$ [6.103] and adsorbate structures like $\text{Cu}(111)+(3\sqrt{3}\times 3\sqrt{3})\text{R}30^\circ\text{-TMB}$ [6.46], $\text{Ag}(111)+(4\times 4)\text{-O}$ [6.61] and $\text{Ag}(111)+(7\times \sqrt{3})\text{rect-SO}_4$ [6.58].

In the method described in this section, non-overlapping MT spheres were used to minimise the potential steps between the MT spheres. However, there remains an energy dependence of the MT radii and the interstitial potential. This is still an inadequate description of the potential, as the potential without the exchange-correlation term should in principle be independent of the energy of the incident electron. The MT radii should likewise be independent of energy. These issues are addressed in Section 6.1.6.3.

6.1.6.3 A New Step-Free Overlapping Muffin-Tin Potential

A new approach to obtain a step-free potential and energy independent MT radii was recently developed by J. Rundgren et al. [6.104]. A step-free potential is characterised by the complete absence of steps and therefore a continuous potential at the MT radii. Referring to Figure 5.3, this implies: there will be a single value of the inner potential $V_0(E)$ for all atomic layers, instead of the layer-dependent muffin-tin zero of Figure 5.3; the inner potential $V_0(E)$ will match without step the spherically symmetric potential within each MT sphere. The step-free method has two important features: (a) the inner potential refers to an energy-independent MT zero V_{MTZ} , which is identical to the vacuum level so that $V_0(E) = V_{\text{MTZ}} + V_{\text{XC}}(E)$ and $V_0(\infty) = V_{\text{MTZ}}$; and (b) the method allows overlapping atomic potentials, such that MT radii can add up to more than the near-neighbour interatomic distances and thus create intersecting spheres. The concept of overlapping MT spheres is not new, but also not common in LEED. These aspects will be further discussed in the following. A schematic illustration of the MT potential with overlapping spheres is given in Figure 6.12.

At high energies, say 200 keV, as used in transmission electron microscopy, the exchange–correlation interaction $V_{\text{XC}}(E)$ between an electron and a solid vanishes because of finite-time electron gas relaxation in solids. Then the inner potential $V_0(E)$ becomes energy invariant, and $V_0(E) = V_{\text{MTZ}}$; this is determined together with the

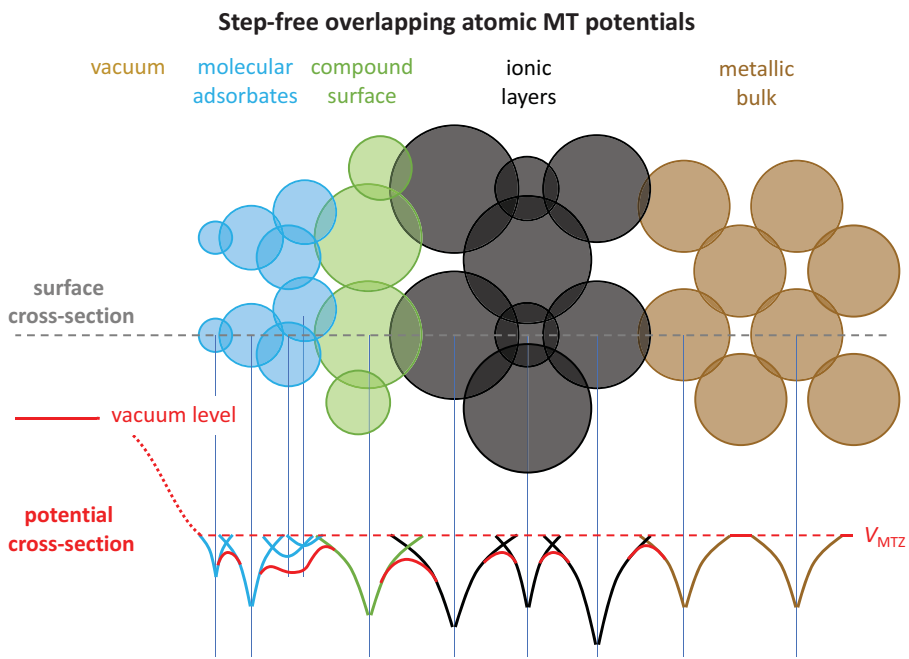


Figure 6.12 Sketch of step-free overlapping MT potentials for a hypothetical surface consisting of adsorbates (blue) on a compound surface (green) supported by an ionic film (black) on a metallic bulk (brown), shown in cross-section. The MT radius for each atom is chosen such that a common MT zero V_{MTZ} (red horizontal dashed line) can be defined, with no step between the MT zero and the potentials within the spheres. The MT radii and the MT zero are determined by differential evolution (DE). A schematic cross-section of the potential along the dashed line is shown below (the red curve sums up the other coloured atomic potentials); the dotted red curve represents the transition to the vacuum level.

choice of the MT radii; see for example also the discussion of the ‘mean’ inner potential by D. K. Saldin and J. C. H. Spence [6.105]. The MT zero V_{MTZ} is shown in Figure 6.13.

Given the low energies used in LEED, the effective scattering potential inside the crystal is set up in the new MT model as the sum of the energy invariant MT zero V_{MTZ} and the local-density-functional exchange-correlation (XC) potential of G. D. Mahan and B. E. Sernelius [6.100]. The spatial average of the XC contribution from the interstitial region gives an energy dependent potential $V_{XC}(E)$ with respect to the MT zero. The MT zero V_{MTZ} and the XC potential $V_{XC}(E)$ add up to the inner potential $V_0(E) = V_{MTZ} + V_{XC}(E)$, referred to the vacuum level, as illustrated in Figures 6.12 and 6.13. The MT zero V_{MTZ} is now completely independent of the energy of the incident electron and applies to the whole surface slab, including both the adsorbate layer and the substrate.

The energy dependent XC potential $V_{XC}(E)$ is calculated from the local density functional theory by G. D. Mahan and B. E. Sernelius [6.100]. For LEED intensity

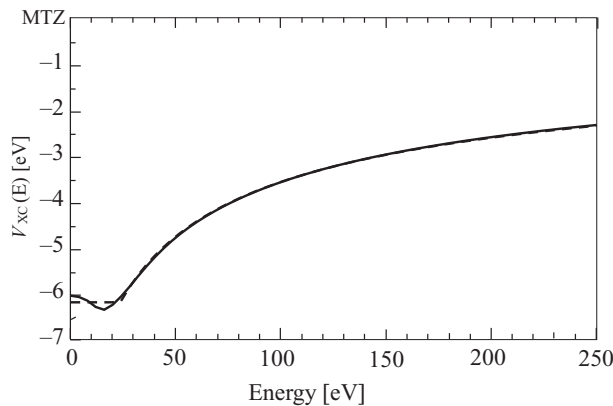


Figure 6.13 Inner potential for the molecular adsorbate system Cu(111)+(3 $\sqrt{3}$ ×3 $\sqrt{3}$)R30°–TMB, calculated with overlapping and optimised MT radii. The MT zero V_{MTZ} is independent of energy. The exchange-correlation potential V_{XC} is calculated according to G. D. Mahan and B. E. Sernelius [6.100] (black curve). Its approximation by four parameters (see Eq. (6.36)) is shown by the dashed curve which is nearly identical with the theoretical curve above a lower energy limit (here 20 eV); below the lower limit, V_{XC} is approximated by a constant. The energy scale is relative to the vacuum level. Reprinted from [6.104] J. Rundgren, W. Moritz and B. E. Sernelius, *J. Phys. Commun.*, vol. 5, p. 105012, 2021 (Open Access).

calculations $V_{XC}(E)$ is modelled with four adjustable parameters p_1 to p_4 , as described in Section 6.1.6.4. It is approximated by a constant lower limit below a minimum energy, as shown in Figure 6.13 by the dashed curve. In the LEED calculation the internal energy of the electron refers to the MT zero which is identical to the vacuum level. However, the experimental external energy (which is measured in the experiment) includes surface specific effects and experimental errors. To relate that internal energy to the external energy, we need the MT zero to be related to the external energy. The parameters used in the LEED calculations therefore include the MT zero. The modulus of the \mathbf{k} -vector inside the crystal is given by $\sqrt{2m_e(E - V_0(E))}/\hbar$, and the phase shifts extracted from the MT potential are related to $E - V_0(E)$ to allow the easy optimisation of the parameters p_1 to p_4 that model $V_0(E)$. An optimisation of these parameters is still necessary because the calculated $V_0(E) = V_{MTZ} + V_{XC}(E)$ does not include work function changes due to surface dipoles and other contributions.

The MT radii of the different atom types are determined by differential evolution (DE) under the condition of achieving a single common V_{MTZ} and different overlap parameters for each atom type. Here, an atom type is defined by the element and similar bonds to the neighbouring atoms; depending on the structure model, atoms of the same element may belong to different types (note that $V_{XC}(E)$ is common to all atoms).

The overlap of atomic potentials permits great freedom in the optimisation of MT radii combined with energy shift. The MT radii and the common level of the MT zero are found by DE optimisation from the superposition of atomic potentials, as follows.

First, the inner potential V_0 is defined as the spatial average of all atomic potentials in the unit cell outside the MT spheres. The unit cell includes the surface slab and two undistorted substrate layers. V_0 therefore depends on the choice of MT radii R_{MT} . These are next found in an iterative process until all atomic potentials fulfil the condition that $V_i(R_{\text{MT}}) = V_0$ for all atom types i ; this step truncates the atomic potentials at their individual MT radii R_{MT} , such that each atomic potential merges without step into the constant V_0 . The resulting total potential is continuous everywhere. V_{MTZ} is then set to V_0 . The details of the procedure are described in J. Rundgren et al. [6.104]. The potentials within the MT spheres are now referenced to the MT zero and the exchange-correlation potential is related to the MT zero. In this scheme, the Mattheiss procedure of superposing atomic potentials is not applied because it assumes non-overlapping MT spheres and fixes the potentials in the MT spheres relative to the vacuum zero; steps in the potential at the MT radius to the interstitial potential cannot be avoided in the Mattheiss procedure.

DE optimisation of overlapping MT sphere radii and a flat MT zero produces potential steps of the order of only 10^{-14} eV (with a computer precision of 10^{-16}). As mentioned in Section 5.2.1, the condition of non-overlapping MT spheres is not essential for the MT model and an overlap is therefore possible [6.106; 6.107]. It has been shown that the use of overlapping spheres leads to the same secular equations as non-overlapping spheres and the same formalism can be used with overlapping spheres, provided that the muffin-tin radii do not exceed the centres of the neighbouring potentials and the interstitial area is treated correctly [6.107]. Increasing the radii of the MT spheres has the advantage of reducing the interstitial volume and allows better representation of bonds between atoms by more accurately including the electron density between the atoms. Overlapping potential spheres have been used, for example, within the exact muffin-tin orbital (EMTO) theory to calculate properties of elemental metal structures and alloys and have led to the same trends as full potential calculations [6.108].

Overlap Parameter

The combination of the energy invariant MT zero with the XC potential and the optimisation of the MT radii implies overlap parameters S_{ovl} which may be different for each element and different bonds. The overlap parameter S_{ovl} is defined as an enhancement of an initially estimated MT radius which is chosen as half of the nearest-neighbour (NN) distance $d(\text{NN})$ of the corresponding atom pair. The condition for the sum of the two MT radii of an atom pair is: $r_{\text{MT}} + r_{\text{MT}}(\text{NN}) \leq d(\text{NN}) \times (1 + S_{\text{ovl}})$. Here r_{MT} is the radius of the atom of interest. Both r_{MT} and S_{ovl} must be chosen such that this condition is fulfilled for all neighbouring atoms; S_{ovl} may be different for each independent atom in the unit cell, see for example the atoms in the middle of Figure 6.12 where the overlap for atoms with manifestly different radii is shown.

The values for the fractional increase S_{ovl} are determined by the DE procedure to obtain the MT potential and can be optimised by fitting to experimental data in the final step of the analysis. A fit of the overlap parameters S_{ovl} to the experimental data is possible because different MT radii produce different phase shifts and also slight differences in the I(V) curves; V_{MTZ} and $V_{\text{XC}}(E)$ also depend slightly on the MT radii,

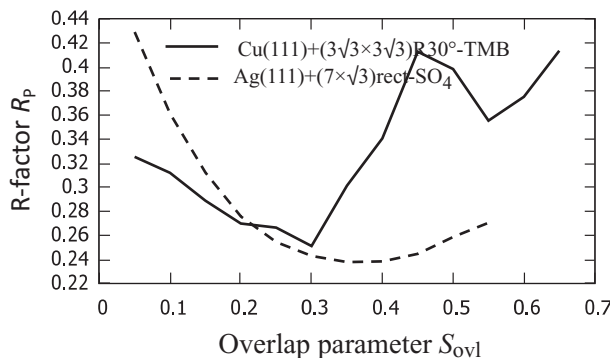


Figure 6.14 R-factor R_p as a function of the overlap parameter S_{ovl} for $\text{Cu}(111) + (3\sqrt{3} \times 3\sqrt{3})\text{R}30^\circ\text{-TMB}$ (full line) and $\text{Ag}(111) + (7 \times \sqrt{3})\text{rect-SO}_4$ (dashed line). (TMB is defined in the caption of Figure 6.2). The optimum structure is kept constant and the phase shifts are calculated with MT radii fulfilling the condition $r_{\text{MT}} + r_{\text{MT}}(\text{NN}) \leq d(\text{NN}) \times (1 + S_{\text{ovl}})$. In this example, S_{ovl} is taken to be the same for all atoms. For the bulk atoms the MT radius is fixed to be half the nearest-neighbour distance.

and there is enough freedom in the choice of the overlap parameter S_{ovl} to obtain a flat MT zero. The inner potential $V_0(E) = V_{\text{MTZ}} + V_{\text{XC}}(E)$ can therefore be fit to the experimental data within limits for the overlap of the MT radii. By design, the MT radii keep the same values throughout the whole energy range. The overlap parameters apply to all atoms; for the bulk atoms in close packed metals the MT radius can be fixed to be half the NN distance.

In actual optimisations [6.104], the DE optimisation leads to an average value of S_{ovl} in the range 0.3–0.4 for all atoms. Only small differences from the average occur when the parameters for individual atom types are fit independently. The R-factor as a function of an average S_{ovl} is shown in Figure 6.14 for two optimisations; there is a clear minimum for S_{ovl} around 0.3. Figure 6.14 shows the results for two relatively complex systems, $\text{Cu}(111) + (3\sqrt{3} \times 3\sqrt{3})\text{R}30^\circ\text{-TMB}$ and $\text{Ag}(111) + (7 \times \sqrt{3})\text{rect-SO}_4$. For the first system the minimum R-factor is at $S_{\text{ovl}} = 0.3$, while for the second system it is at $S_{\text{ovl}} = 0.35$. Similar results have been found for the simpler systems $\text{Ag}(111) + (4 \times 4)\text{-O}$ and $\text{Ru}(0001) + (\sqrt{3} \times \sqrt{3})\text{R}30^\circ\text{-Cl}$ [6.104]. The parameter S_{ovl} can be refined in the final step of the analysis for the individual atoms to find the minimum R-factor.

Energy Dependence of the Exchange-Correlation Potential

A further parameter f_{XC} is introduced here to take into account possible modifications of the local-density functional XC potential $V_{\text{XC}}(E)$ when excitations are present. A factor f_{XC} related to the ground-state exchange-correlation energy $\mu_{\text{XC}}(E)$ had been suggested by L. Hedin and B. I. Lundqvist [6.99] and discussed in detail by R. E. Watson et al. [6.109]. This factor should ensure that $V_{\text{XC}}(E)$ approaches $\mu_{\text{XC}}(E)$ when E approaches zero. The ground-state exchange-correlation energy cannot be determined experimentally. Therefore, a variable factor f_{XC} is used here which can be fitted

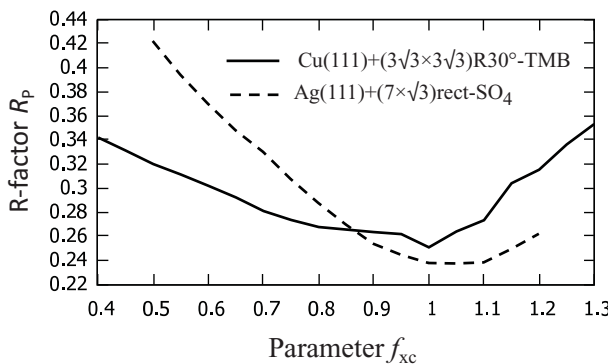


Figure 6.15 R-factor R_p as a function of the correction parameter f_{xc} for the exchange-correlation potential for two systems, $\text{Cu}(111) + (3\sqrt{3} \times 3\sqrt{3})\text{R}30^\circ\text{-TMB}$ (full line) and $\text{Ag}(111) + (7 \times \sqrt{3})\text{rect-SO}_4$ (dashed line) (TMB is defined in the caption of Figure 6.2).

to the experiment. The factor is certainly not unity, as a comparison has shown between two different calculations of $V_{XC}(E)$ [6.97]. The curves calculated by G. D. Mahan and B. E. Sernelius [6.100] exhibited some differences to the calculation after L. Hedin and B. I. Lundqvist.

A similar parameter is considered in the new potential calculation used here [6.104]. The factor f_{XC} multiplying $V_{XC}(E)$ is used here as a qualitative parameter without considering individual excitation energies. It applies to all atoms. The optimum values for f_{XC} are finally found by fitting to the experimental LEED I(V) curves. In the cases which were tested, this produced a flat minimum in the R-factor with values of f_{XC} close to 1.0, indicating that $V_{XC}(E)$ is quantitatively correct [6.104]. Because $V_{XC}(E)$ describes the energy dependence of the inner potential, the fit of the factor f_{XC} to experimental data includes experimental uncertainties in the measurement of the energy of the primary beam. The influence of f_{XC} on the R-factor is shown in Figure 6.15, where the structural parameters have been kept fixed. In principle, a new refinement of atomic coordinates would be required for each new set of phase shifts to obtain the true minimum of the R-factor, but the resulting differences are small.

The fact that the MT parameters S_{ovl} and f_{XC} can be fit to experimental data does not increase the number of structural parameters in the structure search or the refinement. Since their influence on the I(V) curves is relatively small, the optimisation of S_{ovl} and f_{XC} is not necessary in the beginning of a LEED I(V) analysis. The analysis can therefore start with standard fixed data for the MT parameters. The optimisation of the new MT parameters S_{ovl} and f_{XC} can be done in the final step of the analysis after the structure model is already essentially determined with standard MT parameters: this near-final structure then enters the calculation of new final MT parameters. It leads to a final improved structure with lower R-factor and lower error bars, which result from a new calculation of I(V) curves with a new set of phase shifts using the final MT parameters. The deviation in structural parameters is small, mostly below 0.002 nm (0.02 Å). Although such small deviations are hardly visible in the

structure model, they can have a noticeable influence on the R-factor. Indeed, changes of about 50 or more structural parameters in this range can together cause a significant difference in the R-factor, for example for $\text{SO}_4/\text{Ag}(111)$ from 0.235 to 0.21, or for $\text{TMB}/\text{Cu}(111)$ from 0.27 to 0.25. Such sensitivity agrees, incidentally, with the observation made by E. Primorac et al. [6.48] in the comparison with different optimisation procedures that the final reduction of the R-factor requires a large number of iterations with small parameter variations.

The optimisation of the MT parameters slightly improves the final result; the influence on the structural parameters is far below the error limits. This shows that the phase shifts calculation can be done with standard parameters for the overlap and V_{XC} correction.

The new method to obtain phase shifts from a step-free potential by optimised MT radii and energy-shifted atomic potentials leads to an improved agreement in the fit of I(V) curves, as is shown in Table 6.2. We summarise the results of the phase shift calculation with the improved MT model as follows: the agreement between calculated and experimental I(V) curves can be significantly improved compared to the calculation using phase shifts from the conventional method depending on the energy range used in the analysis. The structure model and the main structural data are not changed, but the R-factor is lower and the error bars are smaller. A comparison for four different surface structures is shown in Table 6.2. The average difference in the final structural data obtained with and without overlap in the MT potentials lies in the range of 0.003–0.004 nm (0.03–0.04 Å), with a maximum shift of a single atom by about 0.01 nm (0.1 Å). Such larger shifts were found for a few oxygen positions in two structures listed in Table 6.2 and are still below the error estimate.

We should note that the influence of optimised MT radii shows up mainly in the low energy range of the I(V) curves. At energies above about 80 eV, differences in calculating phase shifts have only small effects.

Table 6.2 Comparison of best fit R-factors obtained with phase shifts from MT potential models with and without overlap

Surface structure	Energy range [eV]	Min. R-factor, using optimised MT radii <u>without overlap</u>	Min. R-factor, using optimised MT radii <u>with overlap</u>
$\text{Ag}(111)+(7 \times \sqrt{3})\text{rect}-\text{SO}_4$	10–150	0.235 [6.58]	0.211 [6.104]
$\text{Cu}(111)+(3\sqrt{3} \times 3\sqrt{3})\text{R}30^\circ-\text{TMB}$	11–200	0.32 [6.46]	0.263 [6.104]
$\text{Ru}(0001)+(\sqrt{3} \times \sqrt{3})\text{R}30^\circ-\text{Cl}$	20–300	0.19 [6.56], 0.137 [6.110]	0.107 [6.104]
$\text{Ag}(111)+(4 \times 4)-\text{O}$	25–250	0.34 [6.61]	0.268 [6.104]

The energy range of the experimental data is also listed. For Cl/Ru(0001) the best fit R-factor in the original paper was 0.19, which later could be reduced to 0.137 with new phase shifts for non-overlapping MT spheres and by including more parameters [6.110]. The comparison shows that in all cases the R-factor is noticeably improved by using phase shifts from the step-free MT potential.

6.1.6.4 Energy Dependence of the Inner Potential

In LEED multiple scattering calculations, the energy of the incident electron inside the solid is increased by the inner potential. The inner potential $V_0(E)$ is necessarily negative and the kinetic energy of the electron inside the solid is therefore higher than outside. Most LEED analyses to date have assumed an energy-independent value for the inner potential V_0 , which is also often called the MT zero V_{MTZ} . However, the inner potential does depend on the energy through the energy dependence of the electron exchange-correlation potential V_{XC} in the crystal, as discussed in Section 6.1.6.3: thus, $V_0(E) = V_{\text{MTZ}} + V_{\text{XC}}(E)$.

The calculation of V_{XC} is usually based on the result obtained by L. Hedin and B. I. Lundqvist [6.99] for the free electron gas. They generated diagrams of V_{XC} versus $k = \sqrt{E}$ for a family of atoms with different electron densities. J. Rundgren [6.97] calculated the inner potential $V_{\text{XC}}(E)$ for a selection of crystals and observed that $V_{\text{XC}}(E)$ curves have a universal shape given by three parameters; here a fourth parameter is used to limit V_0 at low energies. The energy dependence is thus approximated by the four parameters p_1 to p_4 as follows:

$$V_0(E) = \max \left(p_1 + \frac{p_2}{\sqrt{E + p_3}}, p_4 \right). \quad (6.36)$$

Here p_1 is the constant shift of the potential, p_2 determines how steeply the potential increases at low energies (p_2 is usually negative), p_3 slightly adjusts that energy dependence, while p_4 sets a lower limit to avoid unphysically low values at very low energies. The energy dependence of the XC potential is well approximated by these parameters. An example is shown in Figure 6.13, where the lower limit set by p_4 causes a constant value below 20 eV of kinetic energy. Depending on the parameters, this range may be narrower or wider and should not cause problems in the I(V) analysis.

The parameters p_1 to p_4 should be fit in the LEED I(V) analysis, especially when the low energy range is used. The fit is done for each iteration step in the optimisation of structural parameters using the theoretically calculated parameters p_1 to p_4 as start parameters. The parameters for the energy dependence of the inner potential are therefore determined in an independent fit. At higher energies, in many cases a constant value of the inner potential is used, and a fit of this value alone is certainly sufficient for the determination of the structure model. As an inherent property of diffraction, the geometrical parameters are measured in terms of the local wavelength of the electrons inside the crystal, so that the accuracy of the wavelength determines the accuracy of the structural result. Therefore, the energy dependence becomes important for precise structure determinations. This has been clearly demonstrated by S. Walter et al. [6.111], who showed that a small deviation of the substrate lattice constant from the bulk value was caused by using an inner potential that did not depend on energy. The influence of the inner potential in cases where the lattice constant is not exactly known, for example, in epitaxial layers which may be distorted, has been investigated by J. Vuorinen et al. [6.112]. They estimate that the precision is

limited to about 0.001 nm (0.01 Å) if the inner potential is taken to be independent of energy and fit in the I(V) analysis.

The value of the inner potential V_0 determined in the LEED I(V) analysis is not directly comparable to values determined by other experiments because it depends on the choice of the MT radii, although this is probably not the dominant factor. More important in surface studies are further contributions to the inner potential arising from the structure and orientation of the surface due to the surface dipole (resulting in particular from charge transfers between substrate and adsorbate and from the electron spill-over into vacuum, which is also responsible for the surface image potential). In most LEED I(V) analyses the constant part of the inner potential and frequently also the energy dependence are fit to the experimental data, so that parts of the inner potential not considered in the exchange-correlation potential V_{XC} are included in the experimentally determined V_0 .

The different contributions to the ‘mean’ inner potential of a solid have been reviewed by D. K. Saldin and J. C. H. Spence [6.105]. (Here, ‘mean’ refers to an average over the full unit cell, including both the atomic cores and the interstitial region.) The mean inner potential at high energies is determined in high-voltage transmission electron microscopy (HTEM); another contribution arises from the surface dipole layer, and a third part from the energy dependent exchange-correlation potential which is important in the low energy range. The value for the mean inner potential determined in that way differs from the inner potential used in the MT model. The MT sphere potential extends for each atom i to a radius $r_{i,MT}$, where it should meet the flat inner potential without step.

6.1.6.5

Inelastic Mean Free Path (IMFP)

The strong damping of the intensity of the electron beam by inelastic processes inside the solid is the main cause of the surface sensitivity of LEED and all other techniques that use electrons to study properties of surfaces, such as XPS, AES and PED. The knowledge of the inelastic mean free path (IMFP) of electrons in a solid is therefore essential for the quantitative analysis of surfaces. The IMFP is in general energy dependent because the inelastic processes depend on the kinetic energy of the diffracted electrons. The energy dependence is roughly described by a universal curve with a minimum around 100 eV, see Figures 2.27 and 6.6. The energy dependence of the IMFP is not related to the energy dependence of the inner potential V_0 .

The first database of IMFP values for a series of elemental solids as well as for inorganic and organic compounds was published by M. P. Seah and W. A. Dench [6.113], showing a universal curve with a minimum around 50–100 eV of kinetic energy of the incident electron. The IMFP is different from the effective attenuation length (EAL): the EAL includes the removal of the elastically scattered electrons from the incident beam due to diffraction, in addition to the inelastic scattering effect. The techniques which determine the EAL have been reviewed by A. Jablonski and C. J. Powell [6.114]. Depending on the experimental method, either the EAL or the IMFP is measured, while the EAL may or may not be corrected for diffraction effects. For LEED the IMFP determines the imaginary part of the inner potential or optical potential, called V_{0i} .

The IMFP can be experimentally determined by a variety of methods. A major approach is the ‘cover method’ where a substrate is covered by a layer of the material of which the IMFP will be determined. The attenuation of the AES or XPS signal from the covered material as a function of the thickness of the layer and the energy of the signal then gives the IMFP. A comparison of different models to calculate the IMFP with experimental data has been given by C. J. Powell and A. Jablonski [6.115]; a comparison of theoretical and experimental data down to low energies has been published by P. de Vera and R. Garcia-Molina [6.116]. Data for elemental solids have been calculated by S. Tanuma et al. [6.117], while experimental data down to energies below 100 eV have been measured by O. Yu. Ridzel et al. [6.118]. Tables with numerical data for 41 elemental solids in the energy range from 10 eV to 30 keV are available from NIST [6.102]. The numerical data can be used in the LEED programs to derive the imaginary part V_{0i} of the inner potential.

Inelastically scattered electrons are in principle filtered out in LEED, with the exceptions that the incident beam itself has a finite energy spread and that the energy resolution in most cases is not sufficient to filter out phonon losses. In the theoretically calculated intensity, strictly only elastically scattered electrons are included while the damping due to phonon losses is described by a Debye–Waller factor. The comparison to experimental intensities which include the phonon losses is justified by the fact that the thermal diffuse scattering arising from phonon losses follows mainly the elastic scattered intensity [6.119]. The other inelastic processes due to interband transitions, excitations, secondary electron emission, etc., with higher energy losses are filtered out in the experiment, while they are included in the theory through a damping parameter: it enters the theory as the imaginary part of the inner potential V_{0i} .

The damping parameter represents all non-phonon inelastic processes. Its description as the imaginary part of the inner potential V_{0i} leads to a complex wave vector \mathbf{k} inside the solid. The inner potential is usually given as a negative value so that the energy inside the solid is $E - V_0$, where E is the external energy related to the vacuum level (we now write the inner potential V_0 with a real part V_{0r} and an imaginary part V_{0i}):

$$V_0 = V_{0r} + iV_{0i} \quad (6.37)$$

$$\begin{aligned} E - V_0 &= E - V_{0r} - iV_{0i} \\ &= \frac{\hbar^2}{2m_e} k^2 = \frac{\hbar^2}{2m_e} (k_r + ik_i)^2, \end{aligned} \quad (6.38)$$

which gives

$$V_{0i} = -\frac{\hbar^2}{m_e} k_r k_i \quad (6.39)$$

and

$$E - V_{0r} = \frac{\hbar^2}{2m_e} (k_r^2 - k_i^2). \quad (6.40)$$

It follows that

$$\frac{\hbar^2}{m_e} k_r^2 = E - V_{0r} + \sqrt{(E - V_{0r})^2 + V_{0i}^2} \quad (6.41)$$

and

$$\frac{\hbar^2}{2m_e} k_r^2 \simeq E - V_{0r} \quad \text{when} \quad V_{0i}^2 \ll (E - V_{0r})^2 \quad \text{or} \quad k_i^2 \ll k_r^2. \quad (6.42)$$

The optical potential V_{0i} is related to the inelastic mean free path as follows. The phase factor of the plane wave inside the solid is

$$\exp(i\mathbf{k}\mathbf{r}) = \exp(i\mathbf{k}_r\mathbf{r}) \exp(-\mathbf{k}_i\mathbf{r}) = \exp(i\mathbf{k}_r\mathbf{r}) \exp(-k_{i,z}r_z). \quad (6.43)$$

The component of the wave vector normal to the surface has an imaginary part such that the amplitude of the wave is damped with increasing depth into the crystal. The inelastic mean free path $\lambda_e = |1/k_i|$ thus represents the penetration depth. This leads to the relation between the mean free path and the optical potential, using Eqs. (6.39) and (6.40):

$$V_{0i} = -\frac{\hbar^2}{m_e \lambda_e} \left\{ \frac{2m_e}{\hbar^2} (E - V_{0r}) + \frac{1}{\lambda_e^2} \right\}^{1/2} \quad (6.44)$$

and

$$\lambda_e = |1/k_i| \simeq \sqrt{\frac{\hbar^2}{m_e} (E - V_{0r})} \frac{1}{V_{0i}}. \quad (6.45)$$

When $|V_{0i}|$ is small compared to $E - V_{0r}$, these relations simplify to

$$\frac{\hbar^2}{2m_e} k_r^2 = E - V_{0r} \quad \text{and} \quad k_i = -\frac{V_{0i}}{\sqrt{\frac{\hbar^2}{m_e} (E - V_{0r})}}. \quad (6.46)$$

A small k_i means that the wavelength and the conditions for constructive and destructive interference are hardly affected by the optical potential, except that the peaks in the I(V) curves are broadened. The penetration depth can now be related to the peak widths, as follows. We consider lattice planes parallel to the surface with a mutual spacing d normal to the surface. Assuming for simplicity a mono-atomic lattice, we obtain in the kinematic calculation the diffracted intensity as

$$\begin{aligned} I(\mathbf{q}) &= \left| \sum_{n=0}^{\infty} f_n(\mathbf{q}) \exp(i\mathbf{q}\mathbf{r}) \exp(-q_{i,z}nd) \right|^2 \\ &= \left| F(\mathbf{q}) \sum_{n=0}^{\infty} \exp(-q_{i,z}n\alpha\lambda_e) \right|^2, \end{aligned} \quad (6.47)$$

where $q_{i,z}$ is the imaginary part of the normal component of the \mathbf{q} vector, $\mathbf{q} = \mathbf{k} - \mathbf{k}'$, and the factor α is the layer distance in units of the attenuation length, $\alpha = d/\lambda_e$. The

sum in Eq. (6.47) runs over all layers of the semi-infinite crystal. Equation (6.47) describes a broadened Bragg peak of Lorentzian shape. The width is $w \simeq \Delta q_z \simeq 2/\lambda_e$ in momentum space, which means that

$$w \simeq \frac{2V_{0i}}{\sqrt{\frac{\hbar^2}{m_e}(E - V_{0r})}} \quad (6.48)$$

The energy width is then $\Delta E \simeq 2\Delta\mathbf{q}_r \simeq 2V_{0i}$. This relationship allows estimating the optical potential from the width of the peaks (but one must beware of overlapping peaks giving a larger apparent width). The IMFP becomes large at low energies, which implies that V_{0i} is small and the peaks become narrow, as observed in the measured I(V) curves. This is illustrated in Figure 6.16. However, the width in reciprocal space remains approximately constant, as is shown in Figure 6.5.

In many LEED I(V) analyses a constant value for the optical potential is chosen. It is assumed that its influence on the structural result is small and is averaged by the energy range of the measurements. A constant value of V_{0i} is in most cases justified at energies above about 40–50 eV. In Figure 6.16 the comparison is shown for two beams, (10) and (−13), of $\text{SO}_4/\text{Ag}(111)$ in the energy range 10–150 eV; the indices

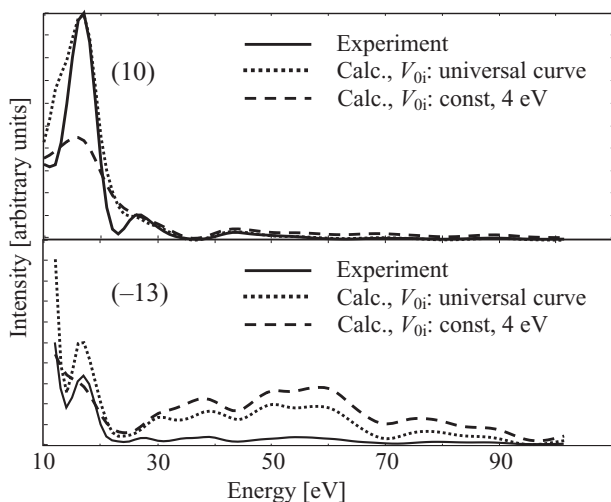


Figure 6.16 I(V) curves for two beams of $\text{Ag}(111)+(7\times\sqrt{3})\text{rect}-\text{SO}_4$. The pairs of theoretical curves are calculated with V_{0i} energy dependent according to the universal curve from M. P. Seah and W. A. Dench [6.113] (dotted curves) and with an energy independent $V_{0i} = 4$ eV (dashed curves) and identical structural data. The experimental curves (black) are taken from [6.58] R. Wyrwich, T. E. Jones, S. Günther, W. Moritz, M. Ehrenspäger, S. Böcklein, P. Zeller, A. Lünser, A. Locatelli, T. O. Menteş, M. Á. Niño, A. Knop-Gericke, R. Schlögl, S. Piccinin and J. Winterlin, *J. Phys. Chem. C*, vol. 122, pp. 26998–27004, 2018, with permission from the American Chemical Society.

refer to the superstructure. Although the agreement with the experimental data is not very good – the peak heights of the ($-1\bar{3}$) beam do not match – it is obvious that the theoretical peaks in the range 10–40 eV are too broad when calculated with constant V_{0i} . Above 50 eV the curves calculated with different models for V_{0i} are practically identical.

6.2

Quasicrystals

Quasicrystals are characterised by a state of crystalline order which is not allowed in the classical definition of a crystal. They do not show translation symmetry and exhibit unusual 5-fold, 8-fold, 10-fold, or 12-fold rotational axes which are not compatible with translation symmetry. They possess long range rotational order and produce sharp diffraction reflections which justify the classification as crystals, but they are called quasicrystals because the translational symmetry is missing; see for example the definition of crystals by the IUCr [6.120] or the discussion of three types of aperiodic crystals by W. Steurer and T. Haibach [6.121].

Quasicrystals were first observed in 1982 by D. Shechtman et al. and published in 1984 [6.122]. This new class of materials was intensively investigated in subsequent years. There are excellent reviews and descriptions of properties of quasicrystals (including [6.123–6.128]). Among the general properties of quasicrystals are low electrical conductivity, high mechanical hardness, low surface energy (leading to non-stick behaviour), low friction and high resistance to oxidation, relative to other alloys.

Quasicrystalline phases have been found in a large number of Al-rich transition metal alloys, mostly ternary alloys; a few binary alloys were also found to have quasicrystalline phases. A list is given in a review by W. Steurer [6.124]. Quasicrystals were discovered rather late because they only exist in very narrow ranges of composition, typically within a few percent variation of each component, for example, in Al-Cu-Fe, between 63 and 68% of Al, between 21 and 26% of Cu and between 12 and 13% of Fe.

Two structurally different types of quasicrystals can be distinguished. One type exhibits an icosahedral symmetry without translation symmetry in any direction: this type is often denoted by an ‘i’ in front of the chemical composition, for example, i-Al-Cu-Fe. A second type exhibits translation symmetry in one direction and consists of a sequence of layers which are quasicrystalline in two directions orthogonal to the first; these are called axial quasicrystals and are sometimes denoted by a prefix p- (pentagonal), o- (octagonal), d- (decagonal) or dd- (dodecagonal) in front of the chemical composition, for example, d-Al-Cu-Co.

The initial quasicrystalline alloys could be produced by very rapid cooling using the melt spinning technique [6.129], thus freezing the solid in the quasicrystalline state. Only micrometre-size quasicrystalline grains were obtained in this way, making surface studies difficult; their thermodynamic stability has not been sufficiently

investigated. This situation changed after the discovery of alloys whose quasicrystalline phase is stable up to the melting point; this allowed using conventional crystal growing techniques like the Bridgman method or a related technique in which a peritectic solidification reaction takes place between different high-temperature crystalline phases [6.130]. Only a few systems have been proven to exhibit thermodynamic stability at high temperatures: these are, among others, the decagonal phases d-Al-Fe-Ni, d-Al-Ni-Co and d-Al-Mn-Pd, and the icosahedral phases i-Al-Cu-Li, i-Al-Cu-Fe and i-Al-Mn-Pd [6.131; 6.132]. In these systems, quasicrystals can be grown with sufficient size for surface studies by LEED, at least a few millimetres across.

We discuss in this section only briefly the quasicrystalline order, the use of n -dimensional hyperspace to describe the diffraction by quasicrystals, the indexing of the LEED reflections, approximate multiple scattering calculations that have been performed and results of structural studies.

6.2.1 Quasicrystalline Order

The most prominent geometric example of the quasicrystalline order is the Penrose tiling in two dimensions [6.133]. A space-filling tiling of a plane with a *single* shape of tiles leads to the five symmetrically inequivalent 2-D translationally *periodic* lattices (see Section 2.1.4 for crystalline lattices). While these do not allow 5-fold axes, R. Penrose [6.133] noted that a space-filling tiling and a 5-fold axis are possible by combining *two* tiles of different shapes: an example is shown in Figure 6.17. The two tiles are ‘fat’ and ‘slim’ rhombi with acute angles of $360^\circ/5 = 72^\circ$ and $360^\circ/10 = 36^\circ$, respectively, and equal side lengths.

No translation symmetry exists in this pattern, but it exhibits orientational long range order. The pentagons formed by the central points of the fat rhombi are marked in Figure 6.17 with thick black lines, and all exhibit the same orientation or are rotated by 180° . Also, the tile edges have only five possible orientations: one such orientation is highlighted in blue in Figure 6.17; these orientations differ by multiples of $360^\circ/5 = 72^\circ$. The tile edges line up exactly across the entire infinite plane (no tile edges exist between the blue lines shown in Figure 6.17). The spacings between tile edges form the aperiodic Fibonacci sequence of short (S) and long (L) spacings; this will be further discussed in Section 6.2.2.

The atomic structure of the quasicrystal depends on the atomic contents of the tiles. An example is shown in Figure 6.18 for a 5-fold surface of an $\text{Al}_{63}\text{Cu}_{24}\text{Fe}_{13}$ quasicrystal, including a multilayer step in the side view, Figure 6.18(b): it exhibits a lack of periodicity in all three dimensions. Its surface structure has been analysed with LEED and STM [6.135]. Five-fold rings can be easily recognised, corresponding to the pentagons of Figure 6.17.

Prominently visible are relatively flat Al-dominated surfaces and interfaces, shown in Figure 6.18(b) as the two upward facing surfaces and two downward

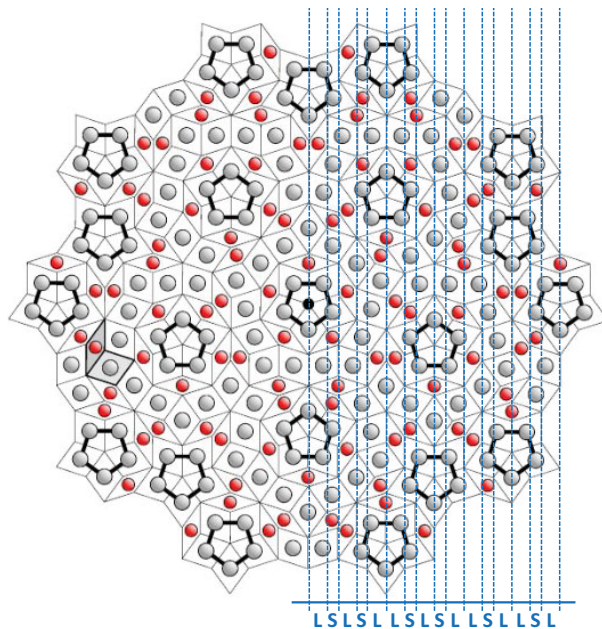


Figure 6.17 Aperiodic (quasicrystalline) arrangement of the two Penrose tiles illustrating 5-fold symmetry (emphasised by an approximately circular truncation). The slim and fat tiles are distinguished by red and grey balls, respectively, at the centre of all tiles (one pair of such tiles is highlighted at left). In real quasicrystals the tiles are occupied not by single atoms but by clusters of atoms, see for example Figures 6.16 and 6.18. The black pentagons indicate local 5-fold symmetry, which is normally only valid in the immediate neighbourhood of the 5-fold axis, while the central pentagon (with a dot at its centre) has a 5-fold axial symmetry that is global, extending to infinity in all directions. There are also five global mirror planes through the central pentagon (one of them is shown as the vertical blue dashed line through this pentagon), while the other pentagons have at most one global mirror plane. The blue lines on the right mark one orientation of tile sides and show how these sides line up across the plane (to infinity), with long (L) and short (S) spacings that form an aperiodic Fibonacci sequence. Adapted with permission from [6.134] K. Hermann, *Crystallography and Surface Structure*, 2nd edition, Wiley, 2016. © 2017 Wiley-VCH Verlag GmbH & Co. KGaA, Boschstr. 12, 69469 Weinheim, Germany.

facing surfaces of two multilayer slabs, which have typical icosahedral quasicrystalline structures consisting of high- to low-density layers with variable compositions; Al (red) is seen to strongly dominate in the denser layers, including the slab surfaces: these relatively widely spaced slab surfaces are the preferred terminations at clean surfaces. Step heights in icosahedral quasicrystals exhibit a Fibonacci series of high and low steps, similar to the line spacings in 5-fold planes exhibited in Figure 6.17, including the golden mean ratio τ discussed in Sections 6.2.2 and 6.2.3.

The combination of the two Penrose tiles is not arbitrary, but governed by matching rules, as illustrated in Figure 6.19. There are many ways to construct an

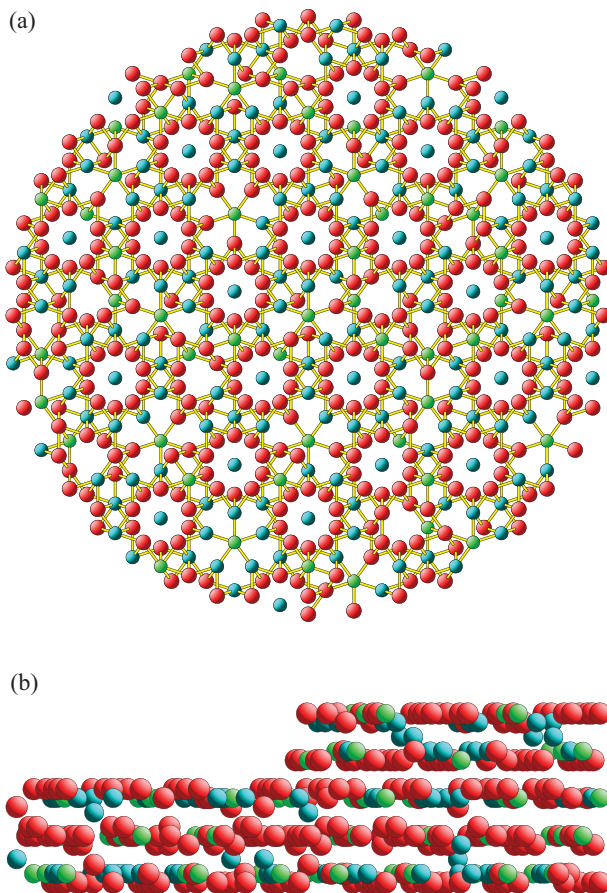


Figure 6.18 Atomic structure of an Al-Cu-Fe(000001) surface with ideal icosahedral bulk-like atomic positions: about 63% of the atoms are Al (red), about 24% Cu (light blue) and about 13% Fe (green). (a) Top-down view of a thin disk-like slice with a few atomic layers. Prominent are rings of 10 red Al atoms: each ring is not 10-fold but 5-fold symmetrical, as it is composed of two rings of five coplanar atoms in two different planes, forming a 5-fold rotational crown: these rings correspond to the 5-fold centres with pentagons in the Penrose tiling of Figure 6.17. No global 5-fold symmetry axis is present in this surface segment. (b) Side view along a step edge, with the surface at the top. The step connects a lower terrace (at left) to a higher terrace (at right). The view is slightly rotated to show rows of atoms parallel to the surface, receding toward the left. Figures by K. Hermann using his Balsac software, private communication.

aperiodic pattern, but only local (short-range) patterns are repeated across the plane (although not periodically), for example, the pentagons drawn in Figure 6.17. The matching rules must be fulfilled in a quasicrystalline pattern of infinite size, but they are not sufficient to obtain a quasicrystalline lattice by adding tiles step by step: the matching rules do not guarantee the tiling to grow without defects. This raises the fundamental question of how quasicrystals grow,

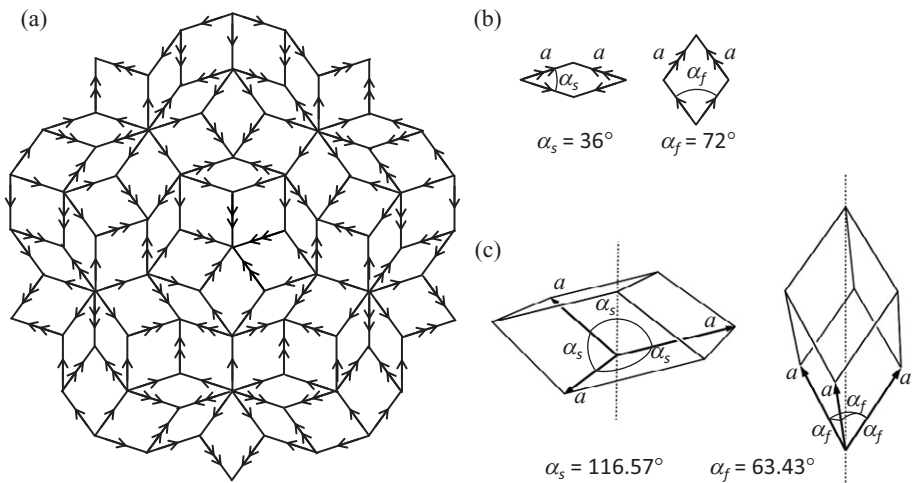


Figure 6.19 (a) Matching rules in the 2-D Penrose tiling (central part of Figure 6.17). The rhombi are combined such that the arrows at the edges match up. (b) Corresponding slim (s) and fat (f) rhombi. (c) Perspective views looking down on the two rhombohedra forming the Penrose tiling in 3-D; the vertical dotted lines indicate 3-fold rotational symmetry axes for these trigonal cells; all side lengths are equal to a to enable matching; further matching rules also exist for a 3-D Penrose tiling. Panel (a) is redrawn with permission from C. Janot, *Quasicrystals: A Primer*, 2nd edition, Clarendon Press, Oxford, 1994. © C. Janot, 1992, 1994. Panel (c) is adapted from K. Hermann, private communication.

since it is generally accepted that long-range direct interactions can be excluded. (The same problem occurs with the large unit cells in Hume–Rothery phases of alloys. It is assumed that these phases are stabilised by electronic effects and the same is probably true for quasicrystals [6.123].) Such questions will not be discussed here, but we note that most quasicrystals exhibit defects, for example, so-called phasons, which limit the resolution of X-ray and neutron diffraction analyses [6.124]. The type of defects occurring in lattices of quasicrystals is not relevant for LEED where the experimental limit of the resolution is relatively low, while approximations used in the calculation limit the resolution even more.

The Penrose tiling can be extended to 3-D: rhombohedra with $\alpha_s = 116.57^\circ$ and $\alpha_f = 63.43^\circ$ are the two building blocks in 3-D [6.123], cf. Figure 6.19. The space is filled such that an icosahedral symmetry is obtained. The structural units in many icosahedral quasicrystals are called Mackay clusters [6.136]. An example of a ‘pseudo’ Mackay cluster occurring in the system Al–Pd–Mn is shown in Figure 6.20.

Figure 6.21 gives an example of experimentally determined electron densities showing decagonal quasicrystal symmetry.

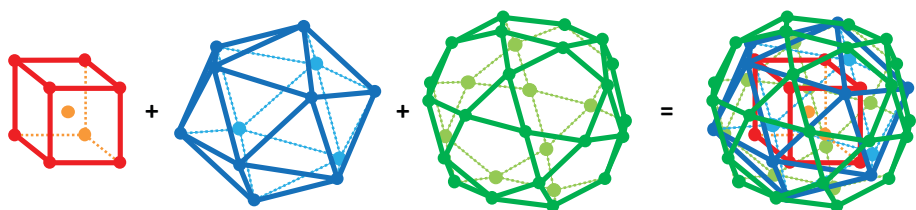


Figure 6.20 ‘Pseudo’ Mackay icosahedron (right) which is considered to be the basic building block of the icosahedral $\text{Al}_{70}\text{Pd}_{21}\text{Mn}_9$ quasicrystal. It consists of an inner shell (partially occupied, hence ‘pseudo’, small body-centred cube, left), an icosahedron (2nd from left) and an icosidodecahedron (3rd from left), combined at right. The pseudo Mackay cluster contains 51 atoms and is approximately 1 nm in diameter. Adapted with permission from [6.123] C. Janot, *Quasicrystals: A Primer*, 2nd edition, Clarendon Press, Oxford, 1994. © C. Janot, 1992, 1994.

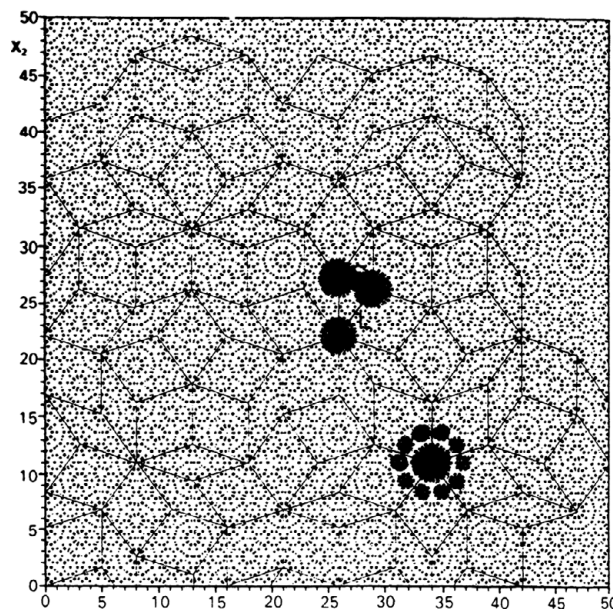


Figure 6.21 Projection of the electron density of the decagonal $\text{Al}_{70}\text{Ni}_{15}\text{Co}_{15}$ phase onto the 10-fold plane, resulting from an X-ray analysis [6.137]. The structure exhibits column-like clusters, some of which are marked as black regions. The Penrose tiling with edge length 1.979 nm is indicated as thin lines in part of the figure. Reproduced with permission of the International Union of Crystallography from [6.137] W. Steurer, T. Haibach, B. Zhang, S. Kek and R. Lück, *Acta Cryst. B*, vol. 49, pp. 661–675, 1993. <https://doi.org/10.1107/S0108768913003143>.

6.2.2 Structural Principles of Quasicrystals

Here we shall relate the structure of quasicrystals to the mathematical Fibonacci sequence and address a construction method based on projecting a simple periodic

lattice in higher dimensions to the aperiodic structure seen in physical space. It is convenient to start in 1-D with a Fibonacci sequence and to describe how it arises by projection of a 2-D periodic lattice onto a 1-D line, forming a 1-D quasicrystalline lattice. The same approach can then be extended to produce a 3-D aperiodic quasicrystalline lattice by a similar projection from a 5-D or 6-D periodic lattice; we will not present this last step, as it is difficult to picture.

In Figure 6.17, dashed vertical lines connect tile sides in a 2-D Penrose tiling: only two spacings occur between these lines, a long (L) and a short (S) spacing, which are determined by the two tile shapes. These spacings follow the Fibonacci sequence, which is aperiodic.

The infinitely long Fibonacci sequence (called Fibonacci word) can be generated as follows: strings f_1, f_2, f_3, \dots , composed of the elements L and S , are formed by the recursive rule that the n -th member of the sequence is assembled from the two preceding members by stringing them together as $f_n = f_{n-1}f_{n-2}$; we can build a Fibonacci sequence by starting with $f_1 = L$ and $f_2 = LS$ and then forming $f_3 = f_2f_1 = LSL$, $f_4 = f_3f_2 = LSLLS$, etc. Equivalently, one may start with L alone, then at each recursive step substitute $L \rightarrow LS$ and $S \rightarrow L$. Although the resulting string looks random at first sight (see Figures 6.15 and 6.20, for example), it has no randomness: it is unique by construction, even though it is aperiodic.

The long (L) and short (S) spacings in a quasicrystal have a length ratio that equals the golden mean: $L/S = \tau = (1+\sqrt{5})/2 = 1.618034\dots = 2 \cos 36^\circ$; this results from the shapes of the Penrose tiles, which reflect and induce the 5-fold rotational local symmetry.

Figure 6.22 suggests that the 1-D Fibonacci sequence can also be obtained by the ‘cut and project’ procedure: it projects onto a 1-D line grid points of a simple square periodic 2-D lattice inclined by a suitable angle α with respect to that 1-D line, namely by a projection of the dots within the shaded band in Figure 6.22 onto the 1-D line. The Fibonacci sequence of long and short spacings is obtained if $L/S = \tau = \cos\alpha/\sin\alpha$, so that $\alpha = 31.72^\circ$. The width Δ of the band is $a(\cos\alpha + \sin\alpha)$, where a is the lattice constant of the square lattice, so that the band spans one 2-D unit cell. The 1-D line is called the real or parallel space ($x_{||}$, or x_{par} in Figure 6.22), while the direction perpendicular to it (x_{\perp} , or x_{perp} in Figure 6.22) is called the perpendicular space. The electron density in 1-D real space $\rho(x_{\text{par}})$ is the density parallel to the 1-D real space line, for example, composed of one atom at each dot on the 1-D real space line in Figure 6.22.

The above mentioned ‘cut and project’ construction reduces the task of describing or producing a 1-D aperiodic quasicrystalline structure (i.e., a Fibonacci sequence) to a simple projection from a periodic 2-D square lattice, where symmetry groups and diffraction conditions can be defined, onto a 1-D line inclined at angle α . This procedure can be generalised to higher dimensions: a 2-D quasicrystal (like the 2-D Penrose tiling) can be obtained by projection from a simple periodic 4-D lattice, while a 3-D quasicrystal can be obtained by projection from a simple 6-D lattice (e.g., a 6-D bcc lattice) in the case of icosahedral quasicrystals; for axial quasicrystals (such as decagonal quasicrystals), one of the 3-D directions is not quasicrystalline but already periodic, so that a 5-D lattice suffices for generating their real 3-D structure.

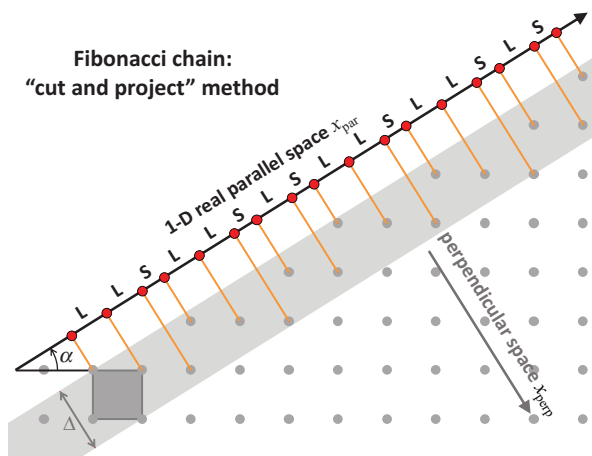


Figure 6.22 A Fibonacci sequence is shown as red dots in 1-D real parallel space. In the ‘cut and project’ procedure, the red dots result from projection onto the 1-D line called ‘real space’ or ‘parallel space’ from the grey dots within the grey strip of width Δ in a 2-D square lattice that extends into the ‘perpendicular space’ and is rotated by angle α ; the strip’s width Δ and the angle α are discussed in the text. Long and short segments between dots in the 1-D real space are labelled L and S, respectively.

However, the lattice points of the higher-dimensional space are in general not simple atoms, but ‘atomic hypersurfaces’ or ‘hyperatoms’: these could be, for example, simple rods of length Δ , as used in Figure 6.23, or spherical hyperspheres or tricontahedral hypersurfaces in 6-D [6.128], etc. The variety of options for the atomic hypersurfaces allows fitting the resulting interatomic distances and the elemental composition to experiment (typically with bulk X-ray or neutron diffraction). An example is given in Figure 6.23: here the simple rod is split into three parts (shown with three colours for Al, Cu and Fe) according to the elemental composition; in a variation of the cut and project method called ‘section method’, the colour that intersects the 1-D real space line then determines the element (Al, Cu or Fe) belonging at that position.

Since 3-D quasicrystals are conveniently described in 6-D or 5-D space, it is also practical to express directions, such as planes and beams, in higher dimensions with six or five indices, especially to highlight symmetries [6.121; 6.123; 6.131]; a loose analogy is the use of four indices for periodic hcp lattices. For example, (001) in periodic cubic lattices (sc, fcc, bcc) denotes a plane and surface with 4-fold rotational symmetry: similarly, (0001) is a plane and surface of an hcp surface with 3-fold rotational symmetry, while (000001) in quasicrystalline icosahedral lattices denotes a plane and surface with 5-fold rotational symmetry. In LEED experiments the specular reflection from a periodic crystal surface is often labelled (00), omitting the third index (perpendicular to the surface): likewise, the specular reflection from an icosahedral surface is often labelled (00000) with five instead of six indices, the last one being

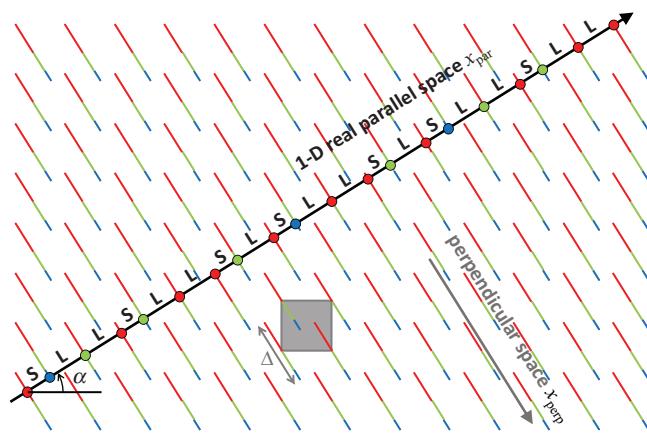


Figure 6.23 Construction of a Fibonacci chain, with ‘atomic hypersurfaces’ replacing the grey dots of Figure 6.22. Here the hypersurfaces are simple rods of length Δ with three segments of lengths proportional to the chemical composition (e.g., red = Al, green = Cu, blue = Fe). The rod colour that intersects the 1-D ‘real’ or ‘parallel space’ determines the atomic element at the intersection point, giving the correct overall composition: red dots become Al atoms, etc.

omitted. Non-specular reflected beams from a cubic surface are labelled (10), (01), ($\bar{1}, 0$), ($0, \bar{1}$), (11), etc.; similarly, non-specular beams from a 5-fold symmetrical icosahedral surface are labelled (10000), (01000), (00100), (00010), (00001), ($\bar{1}0000$), ($00\bar{1}00$), (10001), ($\bar{1}000\bar{1}$), etc., again omitting the sixth index perpendicular to the surface [6.138; 6.139].

6.2.3 Diffraction from Quasicrystalline Surfaces

One of the most striking features of quasicrystals is that they can produce sharp diffraction spots, despite their lack of periodicity. That this is possible can easily be seen from the one-dimensional example shown in Figure 6.22 by taking the Fourier transform of the grey strip. We can represent the 1-D diffraction pattern $A(q)$ of the Fibonacci sequence shown in Figure 6.22 as the Fourier transform of the convolution of the 2-D square lattice with a 1-D box function $w(x_{\perp})$ in the perpendicular space (i.e., a square pulse with $w(x_{\perp}) = 1$ for $0 \leq x_{\perp} \leq \Delta$ and 0 elsewhere) and by then selecting only the 1-D cut $A(q_{\text{par}})$. The Fourier transform $A(q_{\text{par}})$ then results from the product of the Fourier transforms of these two functions: $A(q_{\text{par}})$ comes from the product of a simple periodic square 2-D lattice of δ -functions and the 1-D transform $F(w(q_{\text{perp}}))$ of the box function centred at each lattice point, both shown in Figure 6.24. This is followed by projecting the result to the 1-D line where $q_{\text{perp}} = 0$:

$$A(q_{\text{par}}) = \left| \sum_{h,k} \delta(\mathbf{q} - h\mathbf{a}' - k\mathbf{b}') F[w(q_{\text{perp}})] \right|_{q_{\text{perp}}=0}. \quad (6.49)$$

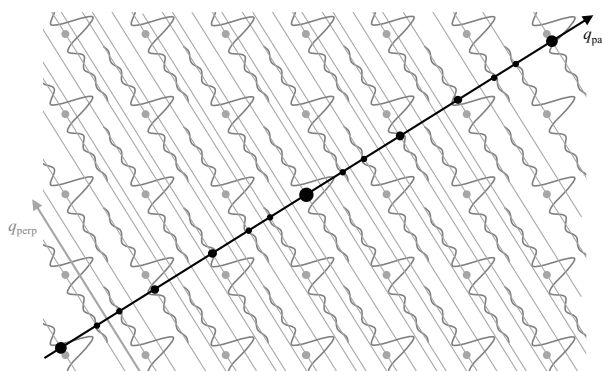


Figure 6.24 Construction of the diffraction pattern of a Fibonacci sequence according to Eq. (6.49). The 2-D square reciprocal lattice of the 2-D lattice in Figure 6.22 is shown as grey dots. The 1-D Fourier transform of the 1-D box function $F[w(q_{\text{perp}})]$ of Eq. (6.50) is schematically drawn as a grey wavelet at each 2-D reciprocal lattice point: it decays to zero along the grey lines shown. The cut along q_{par} (shown in black and oriented at angle α according to the irrational golden mean ratio as in Figure 6.22) gives the 1-D Fourier transform of the Fibonacci sequence and hence its diffraction pattern, shown here as black spots with variable intensities. Redrawn with permission from [6.123] C. Janot, *Quasicrystals: A Primer*, 2nd edition, Clarendon Press, Oxford, 1994. © C. Janot, 1992, 1994.

$F[w(q_{\text{perp}})]$ rapidly decreases with increasing distance q_{perp} from the lattice points, as schematically illustrated in Figure 6.24:

$$F[w(q_{\text{perp}})] = \Delta \frac{\sin(q_{\text{perp}}\Delta/2)}{(q_{\text{perp}}\Delta/2)}. \quad (6.50)$$

The cut along q_{par} of the Fourier transform shown in Figure 6.24 gives the positions of diffraction maxima of the 1-D Fibonacci sequence. Due to the irrational orientation α of the parallel space (q_{par}), there is an infinitely dense set of intersections (one intersection for each 2-D lattice point) and thus an infinitely dense set of reflections, but only a few of them have appreciable amplitude: amplitudes are shown qualitatively in Figure 6.24 by the size of the black spots and more quantitatively in Figure 6.25(a). Higher-intensity intersections are due to reciprocal lattice points that are closest to the parallel space. The resulting reflections are δ -functions in both the parallel space direction q_{par} and the perpendicular space direction q_{perp} for an infinite sequence.

The corresponding LEED diffraction pattern exhibits 5-fold symmetry and the reflections are arranged in circles around the specular beam at normal incidence, cf. Figure 6.25(b). The diffraction vectors of the strong reflections have the magnitudes $\tau^n q_0$ with powers $n = 0, 1, 2, \dots$, cf. Figure 6.25(a); here an appropriate q_0 must be selected, since the choice of q_0 is not unique due to the self-similarity of the quasicrystalline lattice (namely, due to its repeated scaling with the factor τ apparent in Figures 6.23(a) and (b)). One of the nearest reflections to the central specular beam

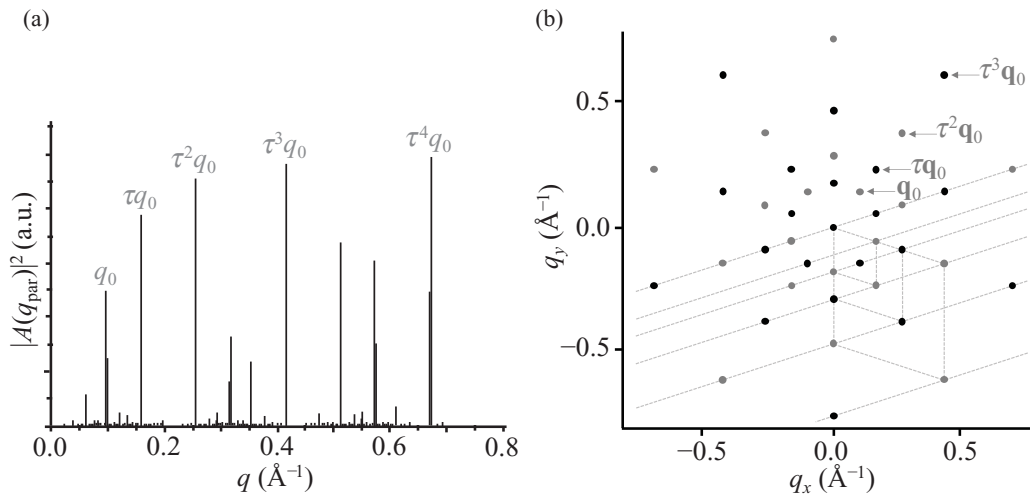


Figure 6.25 (a) 1-D Fourier transform of the Fibonacci sequence, with prominent peaks labelled to show self-similar scaling according to the golden mean τ . Here $q_0 = 2\pi\tau^2/S$, where S is the length of the shorter segment S . (b) A schematic 2-D 5-fold symmetrical LEED pattern, showing prominent spots, which lie on circles with radii $\tau^n q_0$. The dashed lines show relevant geometric relationships between spot positions, as well as the self-similarity with scaling according to the golden mean τ . The grey versus black spots highlight the 5-fold symmetry, while the spot positions exhibit 10-fold rotational symmetry (if we ignore intensities). Additional weaker reflections exist (but are not shown) between the drawn spots, both along radial lines (as in panel a) and between radial lines. Figure redrawn with permission from [6.140] M. Gierer, “Struktur und Fehlordnung an periodischen und aperiodischen Kristalloberflächen”, *Habilitation*, Faculty of Geosciences, University of Munich, 2000.

should be labelled the (10000) beam. The diffraction vector \mathbf{q}_{10000} defines the short distance in the sequence: $q_0 = 2\pi\tau^2/S$. Therefore, S is the short distance in the Fibonacci sequence.

An experimental SPA-LEED pattern of a decagonal $\text{Al}_{72.1}\text{Ni}_{11.5}\text{Co}_{16.4}$ quasicrystal is shown in Figure 6.26(a); a section through a line of reflections is shown in Figure 6.26(b), which also indicates the indices of the reflections [6.140]. The indices are chosen such that they match the L and S distances determined from an X-ray analysis. The diffraction pattern exhibits a 10-fold symmetry due to the superposition of two rotated domains: the point group of the decagonal quasicrystal is $\overline{10}m_2$ and, due to the ABAB... sequence of the 2-D quasicrystalline layers, two terminations exist that are rotated by $360^\circ/10 = 36^\circ$.

6.2.4

Quantitative Analysis of Quasicrystalline Surfaces

Only a few quantitative LEED I(V) analyses of quasicrystal surfaces have been performed, mainly due to their relatively complex structure, cf. Figure 6.18. A first

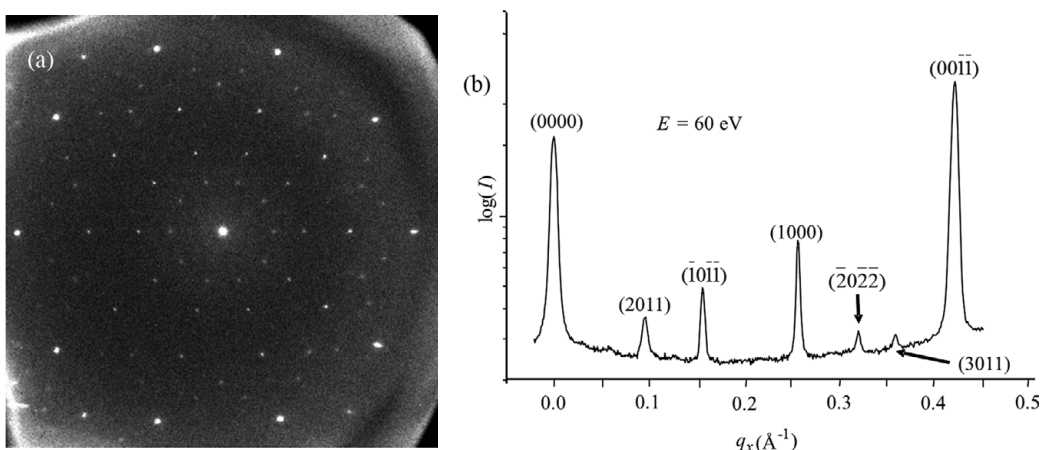


Figure 6.26 (a) SPA-LEED pattern of the 5-fold symmetrical surface of decagonal $\text{Al}_{72.1}\text{Ni}_{11.5}\text{Co}_{16.4}$ at 60 eV. (b) Line scan along $q_x = 0$ through the main reflections of the pattern shown in (a), using a logarithmic scale to emphasise the weaker intensities. Note the 4-index beam labels due to the decagonal bulk, which is periodic perpendicular to the surface. Reprinted from [6.141] M. Gierer, A. Mikkelsen, M. Gräber, P. Gille and W. Moritz, *Surf. Sci. Lett.*, vol. 463, pp. L654–L660, 2000, with permission from Elsevier.

challenge is that the experiment requires an atomically flat surface with an area of at least several square millimetres. Second, the quasicrystallinity severely complicates the multiple scattering theory of LEED, since no periodicity is present. Third, the aperiodicity implies also that there are many distinct local surface structures, as seen in Figure 6.18(a); therefore, many structural parameters should be fit to experiment, including also the alloy composition near the surface and the elemental identity of each atom. Fourth, all bulk terminations (defined as different cuts parallel to the surface) are in principle structurally distinct from each other for icosahedral crystals, since there is no periodicity perpendicular to their surface: many such terminations should therefore be explored. Fifth, steps on the surface can simultaneously expose different bulk-lattice terminations, the diffraction from which should be averaged over. Sixth, two surface orientations are normally possible, related to each other by a rotation of 180° . Seventh, the experimental I(V) database size is similar to that for simple surfaces with small unit cells, since the number of measurable strong beams is not much larger; consequently, there is a relative shortage of data to which the many structural parameters can be fit. For all these reasons, it is necessary to make approximations that in turn degrade the achievable structural detail and accuracy.

The quantitative structure analysis by LEED has the property that the effective scattering factor of a single atom depends on its neighbourhood through multiple scattering, in contrast to X-ray diffraction where the form factor of an atom is independent of its neighbourhood. That would in principle allow determining the chemical composition and atomic arrangement within the local clusters, but the resolution is lower than for normal crystal surfaces due to the lack of periodicity

and the need for approximations in the calculation. With X-ray diffraction (or neutron diffraction), on the other hand, the structure determination is also difficult, mostly due to an insufficient number of experimental reflection intensities. In many cases, it is not possible to measure enough weak reflections between the few strong reflections (see Figure 6.25(a)), probably due to disorder [6.128]: the resolution achievable with X-ray and neutron data is then also limited.

To perform LEED calculations, efficient approximations have been developed to overcome the above-mentioned challenges. A suitable approximation for quasicrystalline surfaces is the ‘average neighbourhood approximation’. The theory has been described by M. Gierer et al. [6.138; 6.139], the main aspects of which are briefly mentioned here. The structure around each atom is divided into a near cluster, where an exact multiple scattering calculation is performed, and an outer region, where an averaged scattering is assumed to be adequate. The time required for the calculation of one cluster strongly increases with the number of atoms in the cluster. Therefore, the multiple scattering calculation is done for a cluster of very limited size (typically 10 atoms) and only a limited number of different clusters is considered: among many possible clusters, the more likely cluster geometries are selected, based on knowledge of the bulk structure, including, for example, the 5-fold double ring that is prominent in Figure 6.18(a). If the cluster size and the number of distinct clusters are chosen sufficiently small, this approximation leads to acceptable computation times. A structural analysis of the 5-fold surface of $i\text{-Al}_{70}\text{Pd}_{21}\text{Mn}_9$ demonstrated that quasicrystalline structures are indeed accessible to a LEED I(V) analysis [6.138; 6.139]. Further progress would be possible if the techniques developed for nanocrystals, see Section 5.2.4, were applied to quasicrystals. This has not yet been done and NanoLEED had not been developed at the time when quasicrystals were analysed.

We next give a short description of the approximations used in the LEED analyses and show one example of the LEED study of an icosahedral Al-Pd-Mn quasicrystal [6.139].

The average neighbourhood approximation is illustrated in Figure 6.27. The atom positions in the far neighbourhood of each atom were averaged over the azimuthal angle ϕ . It was assumed that this average is sufficient for the 5-fold surface of the quasicrystal. The initial atomic positions were taken from the result of a bulk X-ray analysis. First, a large number of different terminations of the bulk lattice were considered. For each termination the z -positions (depths below the surface) of the sublayers were optimised while the lateral positions were kept fixed. The Pendry R-factors of the best-fit termination models reached values between 0.45 and 0.8: models with larger R-factors were then omitted. The best-fit R-factors favoured terminations with a large concentration of Al in the outermost two layers and a reduced outermost interlayer distance of 0.38 Å, compared to the bulk value of 0.48 Å, cf. Figure 6.27. In the next step the 10 best-fit terminations were mixed pairwise and the four topmost interlayer distances were optimised. The best-fit R-factor then reached 0.31 for a particular pair of terminations, which pair is concluded to dominate on the experimental surface. The structural result is displayed schematically in Figure 6.28 and a

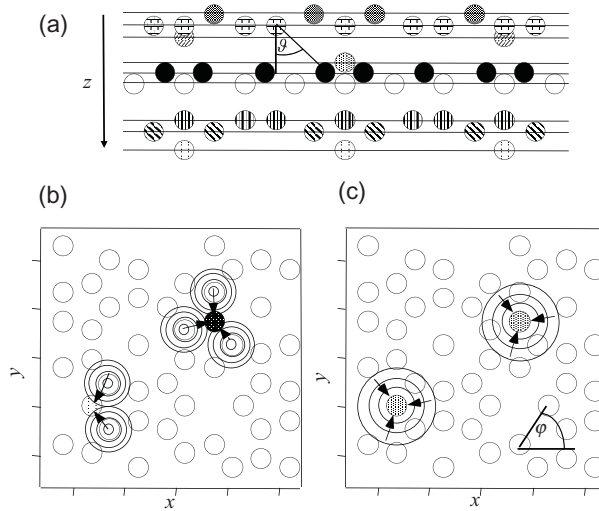


Figure 6.27 Illustration of the average neighbourhood approximation. (a) Schematic drawing of a section through the surface of a quasicrystal. Equal scattering properties of all atoms within a sublayer are assumed, different sublayers being indicated by different shading. (b) The multiple scattering within a cluster of nearest-neighbour or next-nearest-neighbour atoms is calculated exactly. (c) The surroundings further away are approximated by an average: the atom positions depend on the distance and on the polar angle θ , as shown in (a), but not on the azimuth φ shown in (c). Figure reprinted with permission from [6.140] M. Gierer, “Struktur und Fehlordnung an periodischen und aperiodischen Kristalloberflächen”, *Habilitation*, Faculty of Geosciences, University of Munich, 2000.

section through the pseudo Mackay cluster is presented for comparison in Figure 6.29. The best-fit LEED I(V) curves are shown in Figure 6.30.

Important questions in studies of the structure of quasicrystal surfaces include: Are the surfaces quasicrystalline or reconstructed (due to bond breaking or formation) or do the surface layers exhibit an approximant structure, that is, a periodic structure with a short-range structure similar to that of the corresponding quasicrystal? Are they metallic or do they have low conductivity like the bulk structure? Is the surface composition the same as in the volume or is there surface segregation?

The results mentioned for i-Al₇₀Pd₂₁Mn₉ as well as those for some other quasicrystal surfaces show that these surfaces exhibit quasicrystalline order and their surface composition resembles that of the bulk, while the surface termination favours exposing layers that are inherently rich in Al. These conclusions are not only based on LEED I(V) analyses, but also on LEED patterns, STM images [6.142–6.144] and X-ray photoelectron diffraction (XPD) analysis [6.145]; He atom diffraction and ion scattering spectroscopy (ISS) were also used to establish that the 5-fold surface of Al-Pd-Mn consists mainly of Al atoms, and that its structure is essentially a truncation of the bulk structure [6.139]. Slight deviations in the composition occur due to surface preparation by sputtering and annealing. Preferential sputtering changes the

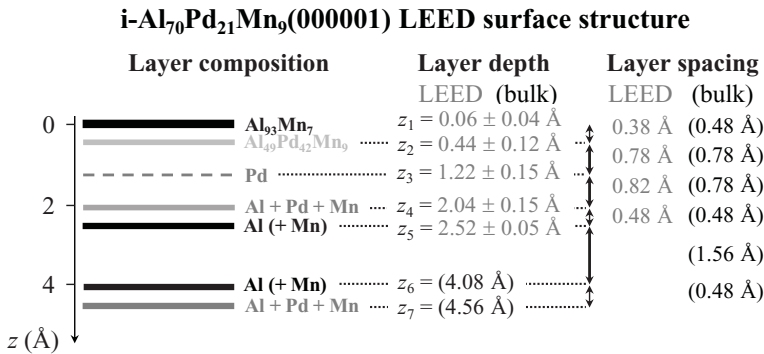


Figure 6.28 Best-fit structure of the 5-fold surface i-Al₇₀Pd₂₁Mn₉(000001) determined by LEED. The bars at the left represent individual atomic layers, with the surface at the top: the bar thickness represents the atomic density in each layer, while the grey level indicates the approximate chemical composition of each layer, spelled out to the right, where parentheses indicate small amounts. Only the composition of the two outermost layers was fit to experiment, with unknown error bars. The layer depth z_i is measured from the outermost layer of the unrelaxed bulk-like structure; values with error bars were fit to experiment by the LEED analysis. Corresponding interlayer spacings are shown on the right. Values in parentheses are for the unrelaxed bulk. Figure redrawn with permission from [6.139] M. Gierer, M. A. Van Hove, A. I. Goldman, Z. Shen, S.-L. Chang, P. J. Pinhero, C. J. Jenks, J. W. Anderegg, C.-M. Zhang and P. A. Thiel, *Phys. Rev. B*, vol. 57, pp. 7628–7641, 1998. <https://doi.org/10.1103/PhysRevB.57.7628>. © (1998) by the American Physical Society.

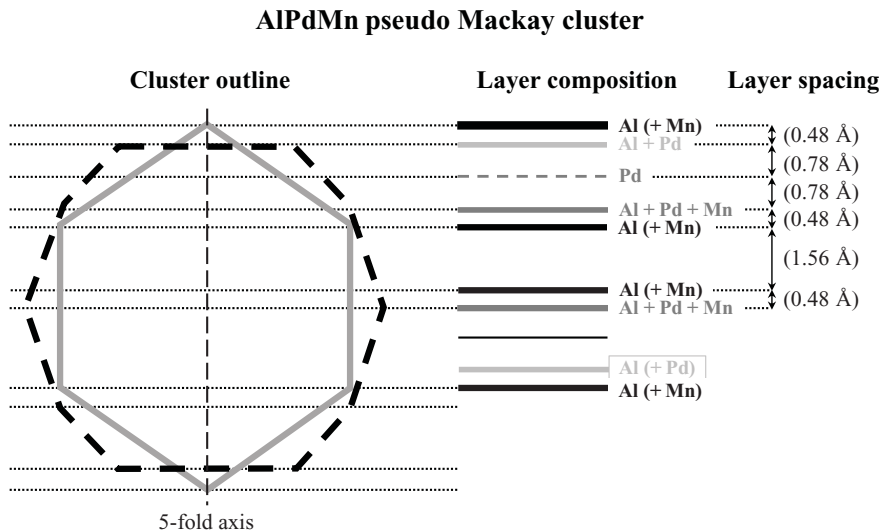


Figure 6.29 The ‘bulk-like’ geometry of the pseudo Mackay icosahedron for comparison with Figure 6.28, where the surface is also at the top and the same grey scale is used: the layer sequences near the surface are very similar in terms of spacings and compositions. Figure redrawn with permission from [6.139] M. Gierer, M. A. Van Hove, A. I. Goldman, Z. Shen, S.-L. Chang, P. J. Pinhero, C. J. Jenks, J. W. Anderegg, C.-M. Zhang and P. A. Thiel, *Phys. Rev. B*, vol. 57, pp. 7628–7641, 1998. <https://doi.org/10.1103/PhysRevB.57.7628>. © (1998) by the American Physical Society.

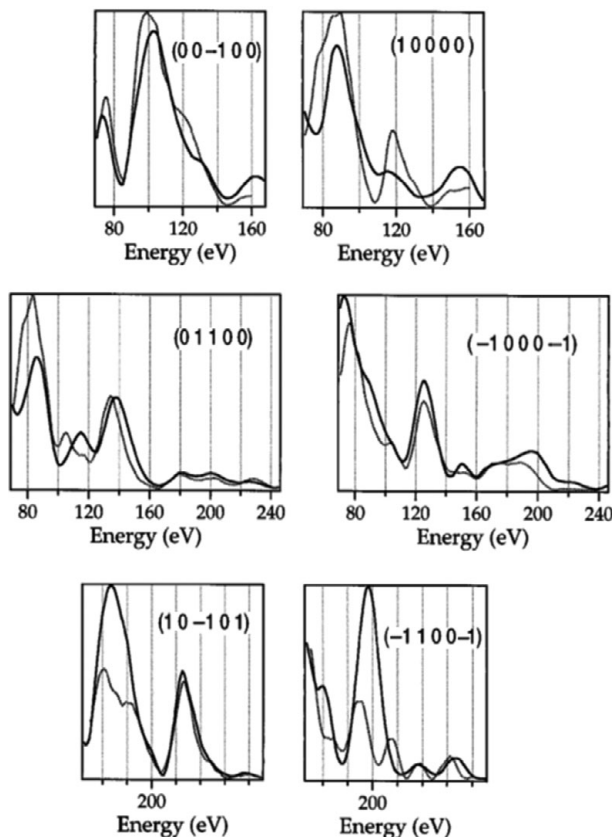


Figure 6.30 Best-fit LEED I(V) curves (experiment: thin lines; theory: thick lines) for six beams of the 5-fold surface of icosahedral $\text{Al}_{70}\text{Pd}_{21}\text{Mn}_9$. Figure reprinted with permission from [6.140] M. Gierer, ‘Struktur und Fehlordnung an periodischen und aperiodischen Kristalloberflächen.’ *Habilitation*, Faculty of Geosciences, University of Munich, 2000.

composition, which can be reversed by annealing. The quasicrystalline order is then also restored. The surface is not reconstructed (in the sense of bond breaking and formation) but some relaxation of interlayer distances occurs, which is similar to the relaxations on ‘rough’ metal surfaces such as fcc(110). These results are consistent with studies on other quasicrystal surfaces [6.146].

We next briefly mention some other LEED and STM results on quasicrystal surfaces for the interested reader. The first structural study of a quasicrystal surface was of decagonal $\text{Al}_{65}\text{Co}_{20}\text{Cu}_{15}$ [6.147]: it was investigated by STM, showing pentagonal clusters that clearly identified a quasicrystalline order of the surface. The high-resolution images showed a quasiperiodic structure similar to a 5-fold Penrose tiling and gave no indication of a reconstruction of the surface structure. Quantitative LEED I(V) analyses exist for 5-fold surfaces of icosahedral phases in the systems $\text{Al}_{70}\text{Pd}_{21}\text{Mn}_9$ [6.139] and $\text{Al}_{63.4}\text{Cu}_{24.0}\text{Fe}_{12.6}$ [6.135]. The structure of the Al-Cu-Fe phase was found to be similar to that in the Al-Pd-Mn phase, with

the exception that screw dislocations were identified in the Al-Cu-Fe sample, unlike in the Al-Pd-Mn sample. The LEED structural result for Al-Pd-Mn was qualitatively confirmed by an X-ray photoelectron diffraction analysis [6.145] with a sample of slightly different composition. The 5-fold symmetry of this surface has also been observed by secondary electron emission imaging [6.148]. However, the surfaces of icosahedral quasicrystals are stepped, forming terraces that are structurally inequivalent. A complete atomistic structural characterisation of such a surface is a very complex task indeed: a further discussion is given by P. A. Thiel [6.149].

The characterisation of 10-fold decagonal surfaces is simpler than that of icosahedral surfaces because decagonal structures are periodic in the direction perpendicular to the surface, and therefore only a few distinct bulk terminations are possible. The structure of the 5-fold decagonal $\text{Al}_{73}\text{Ni}_{10}\text{Co}_{17}$ has been determined by a combination of a quantitative LEED I(V) analysis and high resolution STM [6.150], as well as by an analysis of an approximant surface [6.151]. The LEED pattern of the decagonal quasicrystals exhibits 10-fold symmetry due to the $\overline{10}m_2$ point symmetry and two terminations by the ABAB... stacking sequence, cf. the SPA-LEED pattern in Figure 6.26 for the same system.

Oxygen adsorption has been studied on the 5-fold surface of icosahedral quasicrystals of $\text{Al}_{70}\text{Pd}_{21}\text{Mn}_9$. Oxygen forms a thin Al-oxide layer ($<1\text{ nm}$) which destroys the quasicrystalline order of the surface. A thin and stable oxide layer passivates the surface; no indication of ordered oxide structures was found [6.152]. The 2-fold and 3-fold surfaces of the same system decompose into facets more readily, indicating qualitatively that they are less stable than the 5-fold surface [6.146].

Many other studies of various aspects of quasicrystal surfaces have been performed with STM and spectroscopic methods which will not be discussed here; reviews of the results can be found elsewhere [6.131; 6.132; 6.153; 6.154]. The present state of knowledge of quasicrystals is also summarised by W. Steurer [6.155]. The surface studies by LEED I(V) analysis remain a challenging subject where further improvements seem possible by the application of calculation methods developed for nanocrystals.

6.3

Modulated Surfaces

We consider here surfaces in which different layers have different lateral 2-D periodicities: the lattice mismatch then produces local variations in atomic environments. When crystalline layers having distinct misfit 2-D periodicities are stacked against each other, the mutual interaction between the layers frequently induces deviations in their atomic positions, vibrations, charge densities, etc. These modulations tend to have large-scale periodic repetitions that form moiré-like patterns. Modulations of atomic positions can occur both parallel and perpendicular to the layers. In particular, a surface composed of an overlayer on a substrate with a different 2-D lattice can

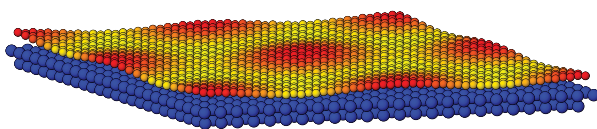


Figure 6.31 Example of a 2-D modulated surface: graphene on Ru(0001). The misfit of the lattice constants leads to an out-of-plane corrugation of the graphene layer together with a slight compression of the C-C bond lengths in the lower flat areas (yellow) and an expansion in the upper corrugation maxima (red). The corrugation is enhanced in the figure for better visibility. A slight induced modulation in the more rigid top substrate layers (blue) is not shown.

exhibit modulations in both the overlayer and the substrate. An example is shown in Figure 6.31: here a graphene layer covers a Ru(0001) substrate, causing perpendicular displacements (but also smaller parallel displacements) in the graphene, as well as minor modulations in the stiffer substrate. Surface modulations occur also in clean reconstructed metal surfaces. (A similar effect is obtained by simply rotating a layer relative to other identical layers, but such rotation is unlikely to be stable since layers with identical lattices are normally aligned as in the bulk crystal.) Aperiodic, in particular incommensurate, modulations may also exist in quasicrystals or composite crystals, for example, but are not discussed here.

The modulations in atomic positions give rise to characteristic satellite reflections in LEED and X-ray diffraction, which can be used to infer the presence, orientation and magnitude of the modulations. Specifically, the LEED patterns of modulated surfaces with overlayers are characterised by satellite reflections in the vicinity of the main reflections from substrate and adsorbate layers. In X-ray diffraction the satellite intensities are usually weak due to small modulation amplitudes, while in LEED multiple scattering effects enhance the satellite intensities. A typical LEED pattern and a short description of the origin of the satellite reflections are given in Section 4.7: see in particular Figure 4.18. In the following we will provide more detailed descriptions and analyses of such diffraction patterns.

A characteristic of modulated structures is the possibility to describe the displacements of all atoms in a large unit cell by a simple function with far fewer parameters than the many individual atomic coordinates (similar to a Fourier transform with only a few terms). The modulation function describes the deviation from a mean value. We will assume here that modulations occur only in the overlayer and top layers of a crystal while the bulk of the substrate is not modulated.

Two different types of modulations can be distinguished: ‘displacement waves’ and ‘density waves’. The displacement waves are similar to position deviations in phonons, but frozen in time. The density waves describe periodic deviations from mean values of occupation factors or thermal vibrations, as well as charge density

waves. A combination of both types of modulations occurs frequently, for example, a charge density wave may be combined with a displacive modulation. The two types of waves can be distinguished in 3-D X-ray and neutron diffraction, while analyses with LEED have not been reported until now. These waves are also less distinguishable in LEED than in X-ray diffraction, as will be discussed in Section 6.3.8. We consider only displacive modulations for LEED I(V) calculations in this section.

In X-ray crystallography, modulated structures are usually described by higher dimensional space groups, as mentioned in Section 6.2 for quasicrystals. These methods are not addressed here because the multiple scattering theory has not been worked out in higher dimensional space groups and seems not to be necessary for the cases considered in this section. We instead use a large superstructure cell or coincidence cell of finite size to describe the structure. This means that for LEED intensity calculations a commensurate superstructure is assumed. Real examples of surface modulations frequently appear to be incommensurate (at least within the coherence size of the LEED beam, i.e., on the scale of 10 nm), but for LEED I(V) calculations the approximation by a sufficiently large coincidence cell seems to be sufficient: this approximation forces the two lattices to coincide in 2-D over finite distances, thus forming a periodic moiré pattern with a finite coincidence cell.

6.3.1 Principles of Modulated Structures

The layered stacking of two (or more) different materials (e.g., a substrate and an adsorbate layer) having distinct lattices can mutually induce deviations of atomic positions in each other, leading to lattice modulations. The period of the modulation function is usually much larger than the translation vectors of the undistorted basic lattices of the component materials and may be commensurate or incommensurate with those basic lattices. The terms ‘coincidence site lattice’ or ‘high-order commensurate (HOC) lattice’ are frequently used synonymously for commensurate modulated lattices, expressing that a long but finite period exists. In STM investigations the term ‘moiré structure’ is preferred (‘moiré’ comes from a French word describing cloth with a rippled appearance). We here select the expression ‘modulated lattice’ applied to both commensurate and incommensurate structures and use the term ‘basic lattice’ for the undistorted layers, which may be an adsorbate layer or a substrate layer. In most cases, modulations occur in an adsorbate layer and/or in the top substrate layers, induced by the interaction between the outermost layer and the substrate. The modulation may be negligibly small in some cases.

Examples of 1-D displacive lattice modulations are shown in Figure 6.32. A displacive modulation wave may consist of two transverse and one longitudinal displacement, as in phonons. One transverse displacement is ‘in-plane’ and one is ‘out-of-plane’, normal to the surface. The most prominent type of modulation observed with STM or AFM is the height modulation or ‘corrugation’, which is the

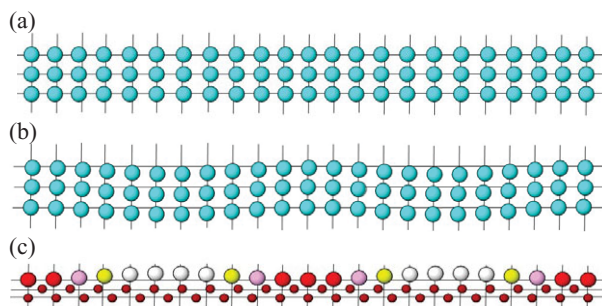


Figure 6.32 Models for three possible displacive 1-D modulations in an adsorbate layer (large spheres) on a substrate (small spheres); two periods of a sinusoidal modulation function are shown from left to right. (a) Longitudinal modulation parallel to the surface, looking down onto the surface; here the horizontal spacings between adsorbate rows varies between small at left, centre and right, and large in between those positions, as can be seen by comparison with the drawn unmodulated grid; (b) transverse modulation parallel to the surface, shown against an unmodulated grid; (c) transverse modulation normal to the surface, looking parallel to the surface. The substrate atoms here have a different average horizontal periodicity, to show a possible cause of the height modulation.

out-of-plane transverse component and may be combined with in-plane transverse and longitudinal components.

Modulations may be 1-D or 2-D. We here use the notation that a 1-D modulation function has one single wave vector, independent of the number of Fourier components or function parameters. Modulations with two modulation waves in two lattice directions are denoted as 2-D modulations, even if the two waves are related by symmetry and in fact only one independent set of parameters exists, such as, for example, in a planar hexagonal lattice with two translation vectors having the same length. The direction of the modulation wave vector is not necessarily the direction of a translation vector, as shown in the examples in Figure 6.33, and may take any oblique direction. In the latter case the symmetry of the basic lattice is not preserved. If the wave vector does not coincide with a lattice vector, incommensurate structures occur, except when the wave vector has a rational relation to a lattice vector.

The modulation wave describes the atomic positions in real space; the direction of the wave vector is conventionally given in reciprocal space because the terminology has been developed for X-ray diffraction where the modulation is observed in the diffraction pattern. At surfaces, modulations can be observed with STM or AFM in real space. To avoid confusion, we always give the indices of the wave vectors in reciprocal space. The calculation of structure factors requires the atom positions to be described by a modulation function in real space. The Fourier transform of the modulation function gives the satellite spots in reciprocal space. Therefore, for the interpretation of the diffraction pattern the indices of the satellite spots are used to describe the modulation wave. This means that the wave vectors of the modulation wave are described in reciprocal space. Modulation functions are described in Section 6.3.5. For clarity the directions in both real and reciprocal space are given in Figure 6.33.

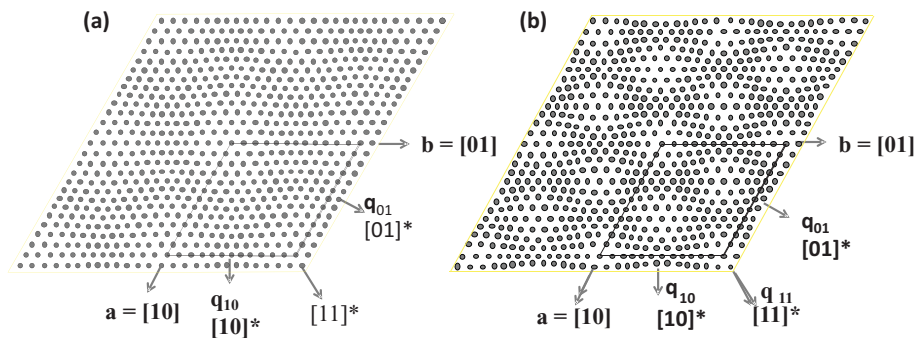


Figure 6.33 Two models of 2-D planar modulations in a hexagonal lattice. The unit cells marked in both panels at the bottom right are those for the simplified structure model for graphene on Ru(0001), with 13 basic graphene unit cells on 12 Ru unit cells in each dimension. The symmetry p3m1 is assumed, which would apply for graphene; for monoatomic structures the models also apply for the symmetry p6mm. (a) Longitudinal waves along the $a = [10]$ and $b = [01]$ axes in real space. (b) Longitudinal wave in the $[11]$ and rotationally equivalent directions in real space. The directions in real and reciprocal space are indicated in the figure; for the wave vectors \mathbf{q} the direction in reciprocal space is always used. The $*$ indicates reciprocal space vectors (see Chapter 2 for the crystallographic conventions). Reprinted from [6.156] W. Moritz, S. Günther and K. Pussi, ‘Quantitative LEED Studies on Graphene’, in K. Wandelt, ed., *Encyclopedia of Interfacial Chemistry: Surface Science and Electrochemistry*, vol. 4, pp. 370–377, 2018, with permission from Elsevier.

There exist symmetry restrictions on the possible modulation functions if the symmetry of the unmodulated structure is to be conserved. In the space group p3m1, only longitudinal modulations are allowed in the directions $[10]$ and $[11]$. In-plane transverse and longitudinal modulations are coupled due to the 3-fold axis and the mirror plane, as can be seen in Figure 6.33. A transverse wave is not compatible with the mirror plane in the p3m1 symmetry. Symmetry restrictions will be discussed in Section 6.3.6.

The modulation period can only be determined within the resolution limit of the LEED instrument or the diffractometer (normally about 10 nm, but more for SPA-LEED, for example). In STM or AFM investigations the resolution limit is frequently given by the domain size or terrace size of the sample. The question whether the modulation is truly incommensurate or high-order commensurate remains, therefore, unresolved in most cases. Often, the modulation period is locally commensurate and varies on a larger scale around an average such that it appears to be incommensurate in the diffraction pattern. This may be observable by a characteristic broadening of satellite reflections if the variation of the modulation period is broad enough. In this chapter, we will only treat idealised well-ordered cases.

For modulated surfaces, two different lattice constants must be considered and the two lattices may be commensurate or essentially incommensurate; both cases occur, but here we will only discuss the commensurate case. For quantitative LEED intensity calculations, the essentially incommensurate case is approximated by a coincidence

lattice of sufficient size, so that the deviations from a truly incommensurate case are small and can be neglected.

With commensurate modulations, the structure may be described as a superstructure of the substrate lattice. However, the term ‘modulated surface’ is preferred when the atomic parameters within the superstructure cell are more easily described with a modulation function that has only a few adjustable parameters than with a long list of all individual coordinates. A structure refinement of modulated structures with all atomic coordinates as free parameters will most likely fail because the parameters are highly correlated and too numerous. A reduction of the number of free parameters by use of modulation functions is therefore necessary. In most cases, a few Fourier components are sufficient to describe the modulation function; if this is not the case, other functions can be used, for example, Gaussian functions, step functions or sawtooth functions for periodic antiphase domains and stepped surfaces.

Modulated lattices exhibit long range order and produce sharp reflections in the diffraction pattern. Sharp reflections also occur when the modulations are incommensurate with the substrate lattice, in which case no translation symmetry exists. Both the modulation function and the basic lattice are periodic. The Fourier transform of their combination produces discrete Fourier coefficients, that is, sharp reflections. The diffraction pattern of modulated structures is characterised by the occurrence of satellite reflections around each reflection of the basic lattice. Since two different lattices are combined with the same modulation period, two sets of satellites occur; for commensurate modulations both sets coincide.

6.3.2 Examples of Modulated Surfaces

Modulated surfaces are found in a series of adsorbate layers and some reconstructed clean metal surfaces. The first detected examples of surface modulations were the clean, reconstructed (100) surfaces of Pt [6.157] and Au [6.158]. The reconstruction of Pt(100) was initially identified as a (5×25) superstructure consisting of a quasi-hexagonal top Pt layer on the square Pt substrate lattice [6.159; 6.160]. Two phases could be identified depending on preparation conditions, one aligned to the lattice of the bulk – the so-called unrotated phase – and a slightly rotated phase. The orientation of the quasi-hexagonal layer and its temperature dependence were also investigated by X-ray diffraction, showing rotational transformations at 1,580 K and above 1,685 K [6.161]. A later study by high resolution He diffraction showed that the surface lattice is indeed incommensurate to the substrate [6.162]. The possibility that the second layer is also reconstructed was examined by a detailed STM and theoretical investigation, which found it to be unlikely [6.163]. A high resolution STM image showing the *unrotated* phase of Pt(100) is shown in Figure 6.34(a), while in Figure 6.34(b) the diffraction pattern of the *rotated* phase obtained with SPA-LEED is shown. The LEED pattern shows the superposition of four domains due to the substrate symmetry [6.164] (this study confirmed the existence of several discrete rotation angles depending on annealing temperature, ranging from ~0.75° to 0.94°). The size of the quasi-hexagonal unit cell has been determined from the LEED pattern;

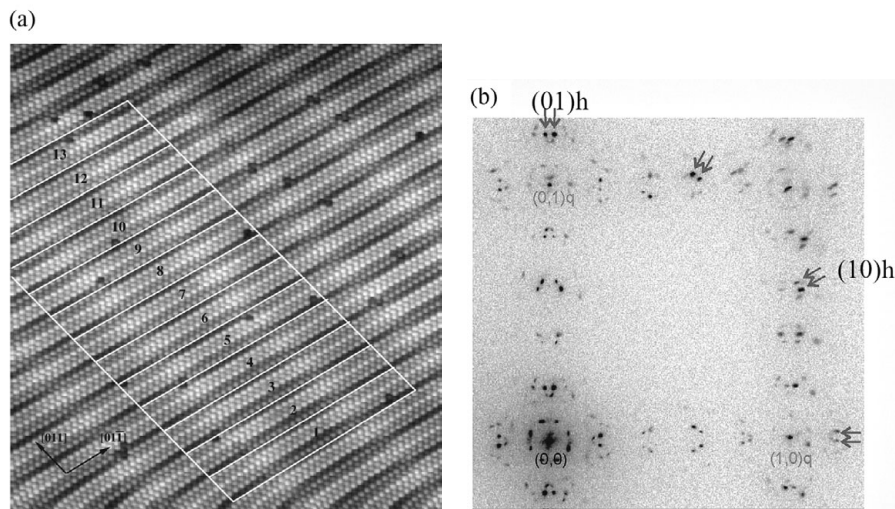


Figure 6.34 (a) Large atom-resolved STM scan of the unrotated hexagonally reconstructed Pt(100) surface. The image size is $20 \text{ nm} \times 20 \text{ nm}$. Thirteen (29×5) unit cells, each containing 30×6 top-layer atoms, are outlined and marked. The reconstruction unit cell is slightly smaller than six surface atom distances in the $[011]$ direction, so the cell is shifted in the $[011]$ direction with respect to the cubic substrate, which yields a modulation of the corrugation pattern inside the (29×5) unit cell. From this modulation the periodicity of the superstructure can be estimated. (b) SPA-LEED pattern (in reverse contrast to enhance visibility) of a hexagonally reconstructed Pt(100) surface rotated by 0.94° . The image shows a diffraction area that includes both the (00) and (11) spots (the latter unmarked at upper right). The (10)q and (01)q spots of the square (quadratic) bulk layers are marked in grey in the figure. The grey arrows marked by (10)h and (01)h are the first order reflections of the hexagonal top layer. The characteristic splitting of the spots is due to the rotation by 0.94° and two symmetrically equivalent domains, indicated by the pairs of grey arrows. The other split spots marked by grey arrows belong to two domains rotated by 90° . Panel (a) reproduced with permission from [6.163] G. Ritz, M. Schmid, P. Varga, A. Borg and M. Rønning, *Phys. Rev. B*, vol. 56, pp. 10518–10526, 1997. <https://doi.org/10.1103/PhysRevB.56.10518>. © (1997) by the American Physical Society. Panel (b) reproduced with permission from [6.164] R. Hammer, K. Meinel, O. Krahn and W. Widdra, *Phys. Rev. B*, vol. 94, p. 195406, 2016. <https://doi.org/10.1103/PhysRevB.94.195406>. © (2016) by the American Physical Society.

all satellite reflections could be identified but a quantitative analysis of the complicated structure has not been possible until now.

The clean Au(100) surface also exhibits a reconstruction similar to that of Pt(100) with a quasi-hexagonal top layer. From the LEED pattern a $c(26 \times 68)$ reconstruction was determined [6.165]; the structure was later investigated by X-ray diffraction and shown to be incommensurate [6.166–6.169].

A surface modulation resulting from a closer packed top layer was also found on the clean (111) surface of Au; this was unexpected, since the close packed (111) surface is the most stable surface of fcc metals. The reconstruction of Au(111) was first observed by LEED [6.170] and was assigned to a 1-D modulation with a $(\sqrt{3} \times 22)\text{rect}$ unit cell

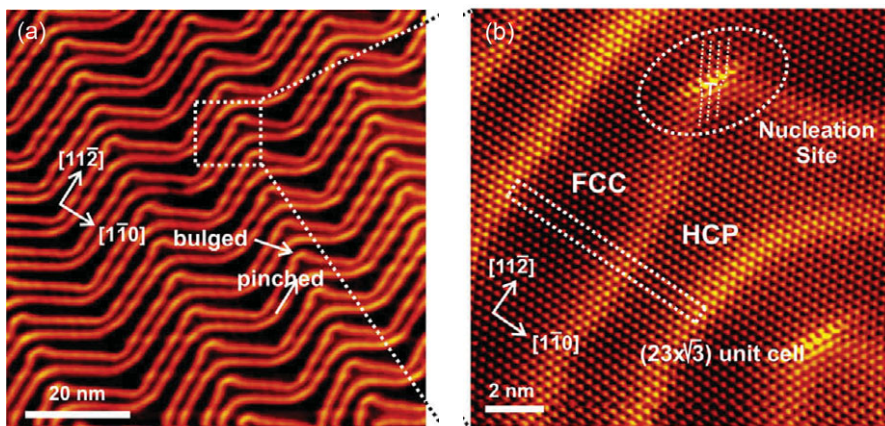


Figure 6.35 (a) STM image of the clean Au(111) surface ($80 \text{ nm} \times 80 \text{ nm}$), showing its herringbone or chevron reconstruction. (b) Atom-resolved STM image showing details of the atomic structure of the reconstruction on Au(111) ($14 \text{ nm} \times 14 \text{ nm}$), blown up from panel (a). Reprinted from [6.172] F. Besenbacher, J. V. Lauritsen, T. R. Linderøth, E. Lægsgaard, R. T. Vang and S. Wendt, *Surf. Sci.*, vol. 603, pp. 1315–1327, 2009, with permission from Elsevier.

by M. A. Van Hove et al. [6.165]. The resolution with LEED only allowed observing the 1-D modulation with a superposition of three domains; the structure was later named $(23 \times \sqrt{3})$ and called a striped domain phase [6.166]. STM images revealed that indeed a 2-D modulation exists and that it has a herringbone pattern. The herringbone structure was investigated with the higher resolution of X-ray diffraction and phase transitions could be observed at higher temperatures [6.171]. In these papers the structure was called ‘chevron structure’. The X-ray results were confirmed by STM images shown in Figure 6.35 [6.172]. The indexing of satellite reflections and possible modulation functions in this surface are discussed in more detail in Section 6.3.5. The basic reconstruction consists of a 1-D compression of the top hexagonal layer in the $[1\bar{1}0]$ direction and a second compression in a symmetrically equivalent direction, either $[\bar{1}01]$ or $[01\bar{1}]$, leading to a herringbone structure, as can be seen in Figure 6.35. Lateral compression of the outermost metal layer is the common feature of the reconstruction of fcc(100) and fcc(111) metal surfaces observed to date.

Modulated structures have also been observed for metal adsorption on other metal surfaces, for example, Cu/Ru(0001) [6.173] and Ag/Ru(0001) [6.174], in physisorbed layers of noble gases on metals [6.175] and for alkali metals on transition metal substrates, for example, K/Ni(100) [6.176]. The cause of the modulation in the latter two cases is the balance between adsorption energy and repulsion between adsorbate atoms; the modulation period therefore depends on coverage or vapour pressure.

An example for lattice modulations occurring in adsorbed molecular layers is given by C₆₀ on Pb(111) [6.177]; STM images of two phases at different coverages are shown in Figure 6.36. The moiré pattern indicates a height modulation of the C₆₀ molecules, which is probably caused by a reconstruction or modulation of the Pb

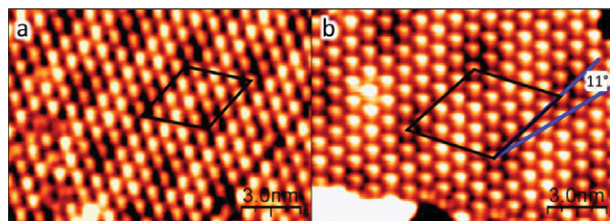


Figure 6.36 Constant current STM images of two different phases of C_{60} on $Pb(111)$: (a) the 3.49 nm moiré structure and (b) the 4.56 nm moiré structure. The fullerenes are in a close-packed structure, each molecule forming a bright spot. The moiré superstructures appear as faint hexagonal height modulations in the STM images. The unit cells of the moiré structures are indicated by rhombi. The 3.4 nm moiré structure is aligned with the C_{60} lattice, whereas the 4.6 nm moiré structure is rotated 11° with respect to the C_{60} lattice. Figure reproduced with permission from [6.177] H. I. Li, K. J. Franke, J. I. Pascual, L. W. Bruch and R. D. Diehl, *Phys. Rev. B*, vol. 80, p. 085415, 2009. <https://doi.org/10.1103/PhysRevB.80.085415>. © (2009) by the American Physical Society.

substrate. An interpretation of the STM images is discussed in Section 6.3.3, see Figure 6.39.

Examples which have attracted much interest are the modulated structures of graphene layers on metal surfaces. The origin of the modulation in these cases is a lattice mismatch between the graphene layer and the substrate. Lattice modulations are easily observed by LEED where satellite reflections occur around the main reflections. As an example, an STM image [6.178] and a LEED pattern of graphene on the Ru (0001) surface are shown in Figure 6.37.

Modulated structures have mostly been observed by STM or AFM, where the modulation is seen directly, and by LEED, where characteristic satellites occur around the main reflections. The diffraction pattern is often rather complicated and, in most cases, it has not been possible to analyse the structures quantitatively. A detailed structure determination of modulated surfaces is rare. Apart from the above-mentioned X-ray analyses of $Pt(100)$, $Au(111)$ and metal on metal systems, only two graphene adsorption systems have been investigated quantitatively. On these surfaces, quantitative LEED I(V), X-ray and DFT analyses have been performed so that the results from different methods can be compared. For graphene on Ru(0001) [6.179; 6.180], qualitative agreement between both experimental methods and the DFT calculation was found, but quantitative differences remained in the amplitude of the corrugation, while the other parameters agreed within the error limits. In the LEED study a height variation up to 0.15 nm was found, while the X-ray results showed 0.08 nm. The discrepancy could not be resolved yet but is probably caused by a small database in the X-ray study and an overestimate of the corrugation in the LEED study due to an insufficient fit and a large R-factor. A further LEED analysis has been made of graphene on Ir(111) [6.181], where the result matches well the structural parameters found in DFT calculations, but some differences remain in the corrugation height found by X-ray diffraction on the same system [6.182].

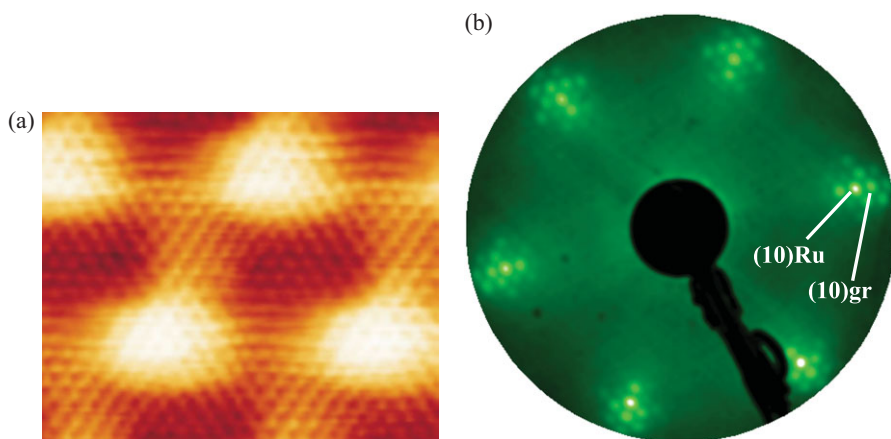


Figure 6.37 (a) STM image of a monolayer of graphene on Ru(0001), $5 \text{ nm} \times 4 \text{ nm}$, $I_t = 1 \text{ nA}$, $V_{\text{sample}} = -0.05 \text{ V}$. (b) LEED pattern of graphene on Ru(0001), at energy 60 eV. The (10) beams of the substrate and the graphene lattice are marked. Panel (a) reproduced with permission from [6.178] S. Marchini, S. Günther and J. Wintterlin, *Phys. Rev. B*, vol. 76, p. 075429, 2007. <https://doi.org/10.1103/PhysRevB.76.075429>. © (2007) by the American Physical Society. Panel (b) courtesy of S. Günther, private communication.

It is often extremely useful to combine diffraction methods with STM or AFM investigations. The existence of different domains and the symmetry of a single domain can be directly observed by STM and AFM, as well as fluctuations of the modulation period, which cannot always be simply derived from the diffraction pattern.

While the modulation period and symmetry may be identified from the diffraction pattern, the quantitative analysis is complicated, as will be discussed in the following sections. The most appropriate methods to analyse surfaces with large modulation wavelengths are SXRD and LEED. Standard multiple scattering programs for LEED are limited in the size of the unit cell, but the application of NanoLEED (see Section 5.2.4) could help, while low energy electron microscopy (LEEM) provides sufficient resolution to measure satellite intensities in the case of very large modulation vectors. LEED therefore is appropriate for analysing modulated surfaces. In this respect, both LEED and X-ray diffraction have advantages and disadvantages.

In the case of X-ray diffraction, the intensity of satellite reflections arising from a single atomic layer is extremely low and difficult to measure, so that the experimental database is naturally small. Surface X-ray diffraction requires well-ordered surfaces and a well-collimated primary beam of high intensity. The quantitative analysis is easier than with LEED, since the kinematic theory can be used. A further advantage is that modulations in the substrate can be detected in deeper layers due to the large penetration depth of X-rays. The high instrumental resolution parallel to the surface allows a more precise determination of the modulation period than with a standard LEED system.

LEED, on the other hand, has the advantage of higher surface sensitivity, that is, less deep penetration. The diffraction geometries for both methods are different: for

SXRD mostly grazing incidence angles are used, to enhance the ratio of surface signal to background, while LEED is operated in backscattering geometry nearer normal incidence. The resolution normal to the surface is in principle larger for LEED, while for SXRD the resolution parallel to the surface is larger (see Figures 2.30–2.32, which illustrate the different diffraction geometries for LEED and X-ray diffraction).

6.3.3 Identification of Modulated Lattices from STM Images

We here describe modulated lattices simply as commensurate superstructures. This is the easiest approach for LEED I(V) calculations, as the standard programs can be used, except that the parameters of the modulation functions must be introduced. For truly incommensurate structures, in most cases, an approximation with a commensurate model will be appropriate and sufficient. The more sophisticated theory of higher-dimensional space applied in X-ray diffraction for (3+d)-dimensional space groups [6.183] is not described here and would not be directly applicable in the multiple scattering theory necessary for LEED.

In contrast to 3-D crystals, where in many cases just one basic lattice is modulated, there exist two different modulated 2-D lattices at surfaces: the lattice of the substrate and the lattice of a surface layer, which is usually an adsorbate or a reconstructed layer (for brevity, the latter will not be mentioned explicitly in the following, but assumed implicitly). In 3-D crystals, equivalent systems exist, for example, in intercalation compounds where two different lattices are combined. On modulated surfaces there exist in general three different periodicities, see Figure 6.38:

- (1) the bulk-like substrate layer with unmodulated 2-D lattice constants (\mathbf{a}_{sub} , \mathbf{b}_{sub});
- (2) the adsorbate layer with 2-D lattice constants (\mathbf{a}_{ad} , \mathbf{b}_{ad}); here we must use the lattice constants of the undistorted adsorbate layer;
- (3) the modulation period (\mathbf{a}_{mod} , \mathbf{b}_{mod}).

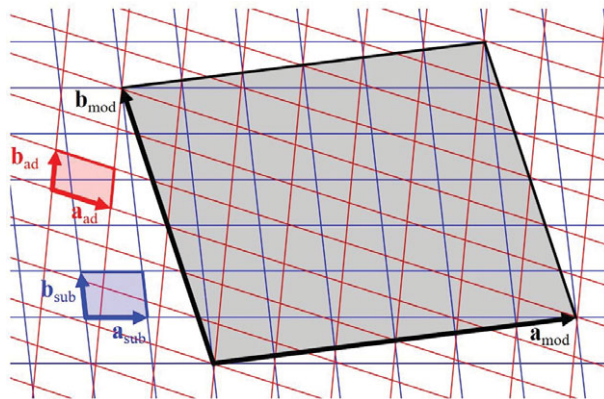


Figure 6.38 Schematic illustration of the basic unit cells of substrate (blue) and adsorbate (red). The coincidence cell (black) defines the modulation vectors.

The modulation period is common to the substrate and adsorbate lattice: if the adsorbate layer is modulated, the underlying substrate layer will be influenced by the adsorbate and will then be modulated with the same period.

Also, in contrast to X-ray studies of modulated 3-D crystals, the modulation lattice can be directly observed by STM or AFM. The moiré pattern occurring by the superposition of two rigid lattices with differing misfit lattice constants or orientations has been described in detail by K. Hermann in Section 6.5 of [6.134], where several examples illustrate how the moiré pattern changes with rotation of one of the lattices or with changes of the lattice constants. The knowledge of these relations is required for the correct interpretation of the STM images, since the orientation of the two basic lattices cannot be directly derived from the moiré pattern alone when they are not resolved in the STM images. In this section we describe how the orientation of the two superposed lattices can be derived when the size and orientation of the modulation vectors have been measured in the STM images and no diffraction pattern is available.

We shall assume that the modulation vectors are known from the moiré pattern observed in the STM images, as well as the lattice constants of the substrate but not the substrate orientation. The lattice constants of the adsorbate are only approximately known because of the possibility of compression or expansion of the adsorbate lattice.

With a procedure similar to that described in the following, the superstructures of C₆₀ related to the Pb(111) substrate lattice have been determined by H. I. Li et al. [6.177]. The two different observed hexagonal moiré patterns (visible in Figure 6.36) were found to have lattice constants of 3.49 and 4.56 nm, respectively (the initial estimates were 3.4 and 4.6 nm, respectively). The C₆₀ molecules are arranged in a hexagonal lattice with a C₆₀–C₆₀ distance of about 1.0 nm, as is common for C₆₀ monolayers on other (111) surfaces of metals. The commensurate superstructures related to the Pb(111) lattice are given by $\begin{pmatrix} 2 & -12 \\ 12 & 14 \end{pmatrix}$ for the 3.49 nm moiré pattern shown in Figure 6.36(a) and $\begin{pmatrix} 9 & -14 \\ 14 & 23 \end{pmatrix}$ for the 4.56 nm moiré pattern in Figure 6.36(b). The resulting structures are shown in Figure 6.39(a) and (b).

In the following, we describe a general procedure to derive the superstructures, applicable to all lattices, without assuming hexagonal symmetry. First, we give some relations between the lattices in real and reciprocal space and assume that the orientation of the lattices is known. The relations between the different lattice constants are described by matrices (see Section 2.1.11 for the matrix notation):

$$\begin{pmatrix} \mathbf{a}_{\text{mod}} \\ \mathbf{b}_{\text{mod}} \end{pmatrix} = \begin{pmatrix} M_{11}M_{12} \\ M_{21}M_{22} \end{pmatrix} \begin{pmatrix} \mathbf{a}_{\text{sub}} \\ \mathbf{b}_{\text{sub}} \end{pmatrix} = \begin{pmatrix} R_{11}R_{12} \\ R_{21}R_{22} \end{pmatrix} \begin{pmatrix} \mathbf{a}_{\text{ad}} \\ \mathbf{b}_{\text{ad}} \end{pmatrix}, \\ = \mathbf{M} \begin{pmatrix} \mathbf{a}_{\text{sub}} \\ \mathbf{b}_{\text{sub}} \end{pmatrix} = \mathbf{R} \begin{pmatrix} \mathbf{a}_{\text{ad}} \\ \mathbf{b}_{\text{ad}} \end{pmatrix}, \quad (6.51)$$

where M_{ij} and R_{ij} are integers for commensurate lattices, and at least one matrix element is an irrational number for truly incommensurate lattices.

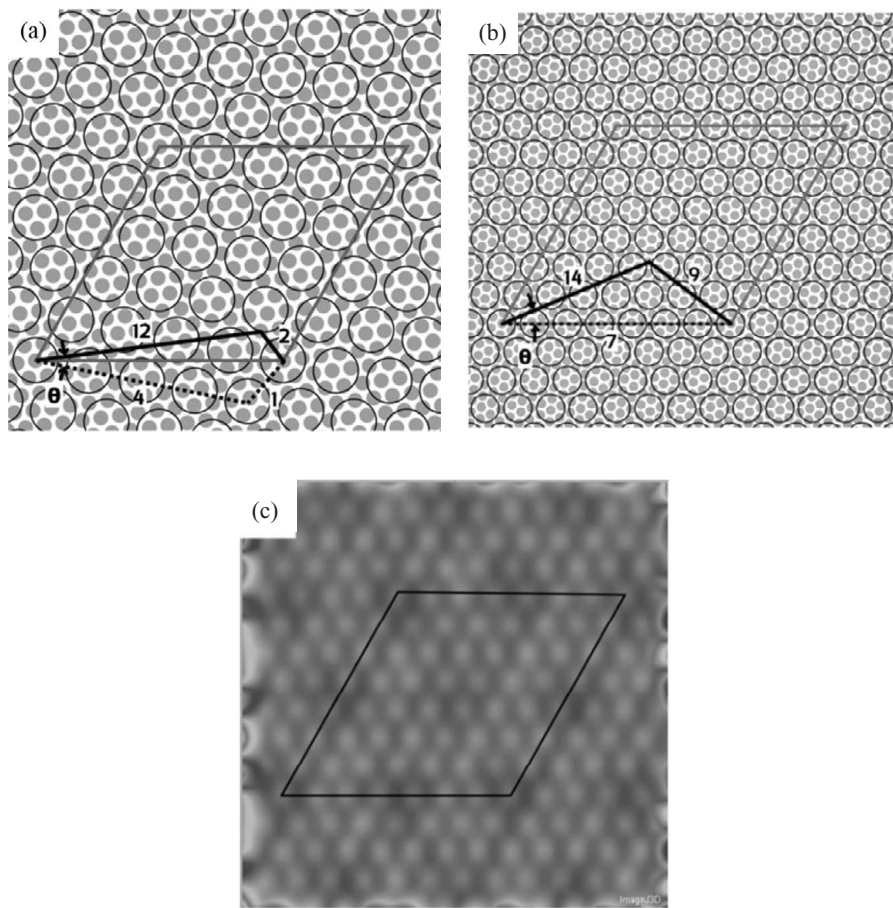


Figure 6.39 Superstructures related to the Pb substrate derived from the moiré patterns shown in Figure 6.36 for C₆₀ on Pb(111). The grey dots mark the positions of the Pb atoms; the circles represent the C₆₀ molecules. (a) The 4.56 nm moiré structure from Figure 6.36(b); (b) the 3.49 nm moiré structure from Figure 6.36(a); (c) contrast enhanced STM image of the moiré pattern of Figure 6.36(a), showing that the modulation vectors are doubled compared to the initial estimate of 3.4 nm. Figure reproduced with permission from [6.177] H. I. Li, K. J. Franke, J. I. Pascual, L. W. Bruch and R. D. Diehl, *Phys. Rev. B*, vol. 80, p. 085415, 2009. <https://doi.org/10.1103/PhysRevB.80.085415>. © (2009) by the American Physical Society.

Conventionally, the superstructure is related to the substrate lattice and the matrix \mathbf{M} characterises the superstructure unit cell, or, if the lattices are incommensurate, the direction and length of the modulation vectors in real space. To calculate atomic positions in the adsorbate layer the matrix \mathbf{R} is required as well, characterising the relation between the mean adsorbate lattice and the modulation lattice. The matrix \mathbf{R} can be calculated from \mathbf{M} if the lattice constants and the orientation of the mean adsorbate lattice with respect to the substrate lattice are known. We use Cartesian

coordinates to describe the orientation of the lattice constants by using the following matrix notation:

$$\begin{pmatrix} \mathbf{a}_{\text{sub}} \\ \mathbf{b}_{\text{sub}} \end{pmatrix} = \begin{pmatrix} a_{x,\text{sub}} & a_{y,\text{sub}} \\ b_{x,\text{sub}} & b_{y,\text{sub}} \end{pmatrix} \quad \text{and} \quad \begin{pmatrix} \mathbf{a}_{\text{ad}} \\ \mathbf{b}_{\text{ad}} \end{pmatrix} = \begin{pmatrix} a_{x,\text{ad}} & a_{y,\text{ad}} \\ b_{x,\text{ad}} & b_{y,\text{ad}} \end{pmatrix}. \quad (6.52)$$

The matrix \mathbf{R} is then simply calculated by:

$$\begin{pmatrix} R_{11}R_{12} \\ R_{21}R_{22} \end{pmatrix} = \begin{pmatrix} M_{11}M_{12} \\ M_{21}M_{22} \end{pmatrix} \begin{pmatrix} a_{x,\text{sub}} & a_{y,\text{sub}} \\ b_{x,\text{sub}} & b_{y,\text{sub}} \end{pmatrix} \begin{pmatrix} a_{x,\text{ad}} & a_{y,\text{ad}} \\ b_{x,\text{ad}} & b_{y,\text{ad}} \end{pmatrix}^{-1}. \quad (6.53)$$

For the lattice vectors in reciprocal and real space the following relations hold (vectors in reciprocal space are indicated by *),

$$\begin{pmatrix} \mathbf{a}_{\text{sub}} \\ \mathbf{b}_{\text{sub}} \end{pmatrix} = \mathbf{G}_{\text{sub}} \begin{pmatrix} \mathbf{a}_{\text{sub}}^* \\ \mathbf{b}_{\text{sub}}^* \end{pmatrix}, \quad (6.54)$$

where \mathbf{G} is the metric matrix of the corresponding lattice indicated in the subscript (see Appendix C). We need only the 2-D lattice constants here, namely the lengths of the translation vectors \mathbf{a} , \mathbf{b} and the angle γ between them:

$$\mathbf{G} = \begin{pmatrix} G_{11} & G_{12} \\ G_{21} & G_{22} \end{pmatrix} = \begin{pmatrix} a^2 & ab \cos \gamma \\ ab \cos \gamma & b^2 \end{pmatrix} \quad (6.55)$$

Finally, the wave vectors of the modulation must be calculated from the observed lattice constants \mathbf{a}_{mod} and \mathbf{b}_{mod} . Modulation functions are waves: in this section we generally define the wave vectors in reciprocal space to avoid confusion; the modulation describes the displacements in real space and the period is also measured in real space by STM or AFM. The wave vectors $\mathbf{q}_{\text{mod},1}$ and $\mathbf{q}_{\text{mod},2}$ are identical to the reciprocal lattice vectors of the modulation lattice $\mathbf{a}_{\text{mod}}^*$ and $\mathbf{b}_{\text{mod}}^*$. A combination of both may also occur; we assume here

$$\mathbf{q}_{\text{mod},1} = \mathbf{a}_{\text{mod}}^* \quad \text{and} \quad \mathbf{q}_{\text{mod},2} = \mathbf{b}_{\text{mod}}^*. \quad (6.56)$$

The wave vectors of the modulation $\mathbf{q}_{\text{mod},1}$ and $\mathbf{q}_{\text{mod},2}$ are usually related to the reciprocal lattice vectors of the substrate $\mathbf{a}_{\text{sub}}^*$ and $\mathbf{b}_{\text{sub}}^*$. We can define a matrix $\boldsymbol{\sigma}$ describing the wave vectors \mathbf{q} in terms of the reciprocal lattice of the substrate:

$$\begin{aligned} \mathbf{q}_{\text{mod},1} &= \sigma_{11}\mathbf{a}_{\text{sub}}^* + \sigma_{12}\mathbf{b}_{\text{sub}}^*, \\ \mathbf{q}_{\text{mod},2} &= \sigma_{21}\mathbf{a}_{\text{sub}}^* + \sigma_{22}\mathbf{b}_{\text{sub}}^*. \end{aligned} \quad (6.57)$$

In the case of a 1-D modulation, only one vector \mathbf{q}_{mod} exists and there is no modulation in another direction. We assume here always 2-D modulations with wave vectors parallel to the surface and the vector \mathbf{c} normal to it. With a matrix \mathbf{G}_{mod} defined for the modulated lattice, analogous to \mathbf{G}_{sub} defined for the substrate lattice in Eq. (6.54), namely

$$\begin{pmatrix} \mathbf{a}_{\text{mod}}^* \\ \mathbf{b}_{\text{mod}}^* \end{pmatrix} = \mathbf{G}_{\text{mod}}^{-1} \begin{pmatrix} \mathbf{a}_{\text{mod}} \\ \mathbf{b}_{\text{mod}} \end{pmatrix}, \quad (6.58)$$

we obtain

$$\sigma = \mathbf{G}_{\text{mod}}^{-1}. \quad (6.59)$$

The matrix σ gives the positions of the first order satellite spots in the reciprocal lattice of the substrate. Equation (6.59) describes the transformation of the matrix \mathbf{M} in real space to the matrix σ defining the superstructure in reciprocal space. These general relations hold for commensurate as well as for incommensurate modulated lattices.

Now, if we want to determine the possible orientations of the lattices of substrate and adsorbate which give the measured modulation periods, that is, the moiré structure, we must find the matrices \mathbf{M} and \mathbf{R} (Eq. (6.51)). Frequently, only the modulation lattice, that is, the moiré pattern, is observed. We consider the case where the lattice constants of the substrate are known and those of the adsorbate are approximately known, but neither the orientation of the substrate lattice nor that of the basic adsorbate lattice is resolved in the images. The lattice constants of the adsorbate are only known within certain limits because its lattice probably is distorted in the adsorbed state. It is also not always clear whether the structure is commensurate with the substrate lattice or not. Especially on polycrystalline samples, differently oriented moiré structures often occur with different lattice constants. If a limited set of moiré structures is found with fixed angles relative to the substrate, then it may be assumed that these are commensurate lattices, otherwise arbitrary orientations of the moiré lattice should occur. It can generally be assumed that commensurate lattices are energetically preferred.

If the lattice constants are known for the freestanding overlayer, then limits must be set to allow for elastic distortions in the adsorbed state. There exists a finite set of rotation angles between the two basic lattices which produce a coincidence structure within these limits for the lattice constants of the adsorbate structure. For the superposition of two rigid lattices without elastic distortion, a coincidence lattice does not necessarily exist. A formalism to find the possible relative orientations for coincidence structures has been worked out for hexagonal layers by P. Zeller and coworkers [6.184–6.186] and for general cases by K. Hermann [6.187]. Hermann investigated in detail the geometrical relations of the superposition of two lattices and how the moiré pattern rotates when the angle between the two lattices is changed. The method used by P. Zeller et al. is to calculate the modulated lattice from the product of the two lattice functions, as also used by Hermann. This is done in reciprocal space by the convolution of the Fourier transforms of the two lattices, that is, the two reciprocal lattices. The angle φ between \mathbf{a}_{sub} and \mathbf{a}_{ad} is taken as a variable parameter. The smallest vectors occurring in the convolution are the modulation vectors $\mathbf{q}_1 = \mathbf{a}_{\text{mod}}^*$ and $\mathbf{q}_2 = \mathbf{b}_{\text{mod}}^*$. The vectors in real space, \mathbf{a}_{mod} and \mathbf{b}_{mod} , can be derived from these via Eq. (6.58).

If the two layers are hexagonal, then the modulation lattice is also hexagonal; this occurs frequently in graphene layers on (111) surfaces of fcc metals. For two hexagonal lattices with $|\mathbf{a}_{\text{sub}}| = |\mathbf{b}_{\text{sub}}|$, $|\mathbf{a}_{\text{ad}}| = |\mathbf{b}_{\text{ad}}|$ and $\gamma_{\text{sub}} = \gamma_{\text{ad}} = 120^\circ$, Eq. (6.53) is reduced to:

$$a_{\text{sub}} \sqrt{M_{11}^2 + M_{12}^2 - M_{11}M_{12}} = a_{\text{ad}} \sqrt{R_{11}^2 + R_{12}^2 - R_{11}R_{12}}. \quad (6.60)$$

The reduction to two parameters allows an analytical solution to find all possible commensurate structures of graphene on hexagonal substrates where only the ratio $a_{\text{sub}}/a_{\text{ad}}$ and the angle φ between the vectors \mathbf{a}_{sub} and \mathbf{a}_{ad} appear as parameters. This formalism allows a quick and complete overview of possible commensurate superstructures for hexagonal lattices. It can be extended to square lattices as well. The more general description derived by K. Hermann [6.187] leads to the same results.

We do not describe the above-mentioned methods in detail here, but use a simpler, less sophisticated search method to find the possible orientations applicable for all 2-D space groups. In the following, we assume commensurate structures with known (or approximately known) lattice constants and unknown orientation. The interpretation of the observed moiré pattern then requires the determination of the angles between adsorbate and substrate lattice for which integer values can be expected in the matrices \mathbf{M} and \mathbf{R} . We can search the integer values of R_{11} and R_{12} by checking possible combinations of M_{11} and M_{12} in Eq. (6.53). A distortion of the adsorbate layer is included by allowing a small deviation from integer values for R_{11} and R_{12} . Only two of the four elements in matrix \mathbf{M} need to be independently varied. This gives a list of possible values for M_{11} and M_{12} ; there is a very small set of possible values, M_{21} and M_{22} , which can be combined with M_{11} and M_{12} , mostly defining symmetrically equivalent unit cells. If the lattices are aligned (having parallel basis vectors), the test of all possible combinations is straightforward. If an arbitrary mutual orientation of the lattices is allowed, a systematic search on a sufficiently fine grid of rotations of the adsorbate lattice becomes necessary. The method is outlined as follows, assuming that the lattice parameters of the substrate \mathbf{a}_{sub} , \mathbf{b}_{sub} and γ_{sub} are known; we also assume narrow limits for \mathbf{a}_{ad} , \mathbf{b}_{ad} and γ_{ad} for the adsorbate layer:

- (1) The vectors \mathbf{a}_{ad} , \mathbf{b}_{ad} are calculated assuming an angle φ between \mathbf{a}_{sub} and \mathbf{a}_{ad} . The vector components in Cartesian coordinates are used. We need only the 2-D matrices.
- (2) Equation (6.53) can then be written as:

$$\begin{pmatrix} R_{11} & R_{12} \\ R_{21} & R_{22} \end{pmatrix} = \begin{pmatrix} M_{11} & M_{12} \\ M_{21} & M_{22} \end{pmatrix} \begin{pmatrix} a_{x,\text{sub}} & a_{y,\text{sub}} \\ b_{x,\text{sub}} & b_{y,\text{sub}} \end{pmatrix} \frac{1}{D} \begin{pmatrix} b_{y,\text{ad}} & -a_{y,\text{ad}} \\ -b_{x,\text{ad}} & a_{x,\text{ad}} \end{pmatrix} \quad (6.61)$$

with

$$D = (a_{x,\text{ad}}b_{y,\text{ad}} - a_{y,\text{ad}}b_{x,\text{ad}}). \quad (6.62)$$

We define

$$\begin{pmatrix} c_{11} & c_{12} \\ c_{21} & c_{22} \end{pmatrix} = \begin{pmatrix} a_{x,\text{mod}} & a_{y,\text{mod}} \\ b_{x,\text{mod}} & b_{y,\text{mod}} \end{pmatrix} \frac{1}{D} \begin{pmatrix} b_{y,\text{sub}} & -a_{y,\text{sub}} \\ -b_{x,\text{sub}} & a_{x,\text{sub}} \end{pmatrix}, \quad (6.63)$$

and obtain four equations for the four elements of matrix \mathbf{R} ; only two of these need to be checked: $M_{11}c_{11} + M_{12}c_{21} = R_{11}$ and the analogous equation for R_{12} . The values for R_{21} and R_{22} are not independent and are derived from these.

- (3) We can assume integer values M_{ij} and look for integer R_{ij} . The possible combinations of integer values M_{11} and M_{12} are easily checked while the maximum values are limited by a reasonable assumption for the size of the unit cell. A tolerance factor can be set for the allowed deviation of R_{11} and R_{12} from integer values. The calculation must be repeated for all combinations of M_{11} and M_{12} .
- (4) Steps 1–3 must be repeated with a sufficiently fine grid of φ and, if necessary, for a grid with the lengths a_{ad} and b_{ad} for the translation vectors or with the ratio $a_{\text{ad}}/b_{\text{ad}}$, allowing a deformation of the adsorbate lattice within reasonable limits. Finally, the deviation from integer values of $\det(\mathbf{R}) = R_{11}R_{22} - R_{12}R_{21}$ can be plotted as a function of φ to visualise angular regions where coincidence structures can be expected. The quantities $\det(\mathbf{M})$ and $\det(\mathbf{R})$ give the size of the modulation unit cell in terms of the substrate unit cell and the adsorbate unit cell, respectively. These values and \mathbf{a}_{mod} , \mathbf{b}_{mod} and γ_{mod} can be checked against the observed values in the moiré pattern.

It should be noted that the acceptable matrices \mathbf{M} with integer components include all possible coincidence structures. The superstructure can be related to the primitive vectors \mathbf{a}_{sub} and \mathbf{b}_{sub} or to a superstructure of the substrate lattice. For example, the matrix \mathbf{M} may have integer components when related to the single hexagonal unit cell but not when related to a $(\sqrt{3} \times \sqrt{3})R30^\circ$ superstructure. Of course, integer components of \mathbf{M} may occur in both cases.

As an example, we show in Figure 6.40 the results for a possible quasi-hexagonal superstructure due to top-layer reconstruction of the square lattice of clean Pt(100). The data are taken from R. Hammer et al. [6.164]. On this surface two reconstructions have been observed, as mentioned in Section 6.3.2: a non-rotated and a rotated quasi-hexagonal structure. The purpose here is to show that we can easily find the lattice constants of the rigid, distorted hexagonal layer and the orientation with respect to the substrate, if the modulation vectors are known; these are seen in the STM images. For the non-rotated case, the authors of the study find a rectangular superstructure cell with approximate dimensions 7.2×32.7 nm aligned to the square lattice of the (100) surface.

We look for possible quasi-hexagonal lattices, and their orientations, which are commensurate with this superstructure. The solution can of course be found directly by a simple calculation, but we want to illustrate the search method and use this as a test case. As input values we take the square lattice of Pt(100) with lattice constants $a_{\text{sub}} = 0.2772$ nm, the rectangular modulation lattice with $a_{\text{mod}} = 7.2$ nm, $b_{\text{mod}} = 32.7$ nm and a hexagonal lattice with 120° angle between the lattice vectors; we allow a contraction of the lattice in the range between 1 and 6%, that is, $a_{\text{ad}} = b_{\text{ad}}$ ranging

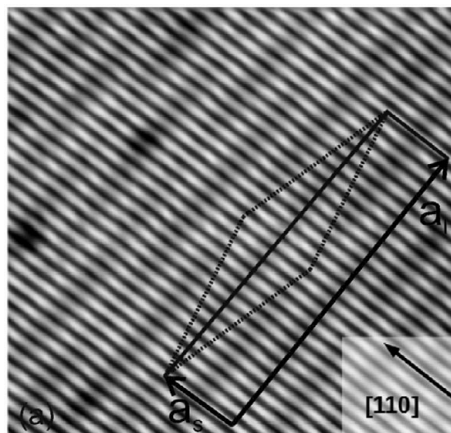


Figure 6.40 STM image of the non-rotated quasi-hexagonal reconstruction of Pt(100), 44 nm × 42 nm. Reproduced with permission from [6.164] R. Hammer, K. Meinel, O. Krahn and W. Widdra, *Phys. Rev. B*, vol. 94, p. 195406, 2016. <https://doi.org/10.1103/PhysRevB.94.195406>. © (2016) by the American Physical Society.

from 0.2744 to 0.2606 nm, in steps of 0.002 nm. A hexagonal lattice is assumed in the search procedure; a quasi-hexagonal layer or distorted hexagonal layer is obtained by allowing a deviation from integer values in the elements of the matrix \mathbf{R} .

The search procedure then finds all possible combinations of M_{11} and M_{12} which give R_{11} in the vicinity of an integer value within an error bar of 0.1. The integer values are taken to calculate the vector components $a_{x,\text{ad}}$, $a_{y,\text{ad}}$, $b_{x,\text{ad}}$ and $b_{y,\text{ad}}$ of the distorted hexagonal lattice and the angle between the translation vectors. The corresponding vectors \mathbf{a}_{mod} , \mathbf{b}_{mod} are also calculated using the calculated vectors \mathbf{a}_{ad} , \mathbf{b}_{ad} and the unchanged substrate vectors \mathbf{a}_{sub} , \mathbf{b}_{sub} .

Solutions occur only for a hexagonal lattice with 4% contraction: no solutions exist for other values in the grid of \mathbf{a}_{ad} . The distortion of the hexagonal lattice is calculated with the integer values of the matrix elements of \mathbf{R} . Several possible structures are found: only two structures occur in the vicinity of 90° between \mathbf{a}_{mod} and \mathbf{b}_{mod} ; both are aligned with the \mathbf{a} -axis of the adsorbate layer parallel to the \mathbf{a} -axis of the substrate. Six further solutions can be excluded as their modulation lattice deviates too much from the observed rectangular lattice. The details of the two solutions are the following, with lengths given in nanometres and matrices written by rows as (m_{11} , m_{12} / m_{21} , m_{22}):

Solution 1:

$$\mathbf{M} = (26.0/1, 118), \mathbf{R} = (27.0/72, 142)$$

$$\mathbf{a}_{\text{ad}} = (0.26693, 0.00000), \mathbf{b}_{\text{ad}} = (-0.13339, 0.230350), |\mathbf{a}_{\text{ad}}| = 0.26693, |\mathbf{b}_{\text{ad}}| = 0.266190$$

$$\mathbf{a}_{\text{mod}} = (7.20720, 0.00000), \mathbf{b}_{\text{mod}} = (0.27720, 32.70960), \gamma = 89.5144^\circ.$$

Solution 2:

$$\mathbf{M} = (26, 0/0, 118), \mathbf{R} = (27, 0/71, 142)$$

$$\mathbf{a}_{\text{ad}} = (0.26693, 0.00000), \mathbf{b}_{\text{ad}} = (-0.13347, 0.23035), |\mathbf{a}_{\text{ad}}| = 0.26693, |\mathbf{b}_{\text{ad}}| = 0.26622$$

$$\mathbf{a}_{\text{mod}} = (7.20720, 0.00000), \mathbf{b}_{\text{mod}} = (0.00000, 32.70960), \gamma = 90^\circ.$$

The second solution is exactly that given in R. Hammer et al. [6.164], the only difference being one of notation: there a centred lattice for the reconstructed layer is used while here a distorted hexagonal lattice has been assumed. In the first solution the vector \mathbf{b}_{mod} is shifted by one lattice constant in the \mathbf{a} -direction, which leads to an oblique lattice that is not consistent with the observation but remains within the tolerance limits. The number of possible solutions depends strongly on the tolerance allowed in filtering integer values of the elements in \mathbf{R} . A tolerance of 0.1 for the large values of the modulation vectors occurring in this superstructure is fairly small and therefore requires small steps in the variation of the adsorbate lattice constants.

6.3.4 Reflection Indexing

In this section, we address the question of how to label, that is, how to index, the relatively complex sets of reflections that occur with modulated structures. Modulation waves are periodic functions and produce sharp reflections even for incommensurate modulations where no translation symmetry exists. For commensurate modulations a superstructure unit cell exists, so that the reflections could be indexed either according to that superstructure cell by integer indices or with respect to the substrate cell using fractional indices, as is the usual practice in LEED I(V) analyses. The use of superstructure indices is, however, not very convenient in the case of large modulation vectors; for incommensurate modulated structures it is not practical anyway.

When all possible reflections within the reciprocal unit cell are visible, as in the (7×7) reconstruction of Si(111), a description as a modulated structure does not make sense, since the reduction of the number of parameters is not possible by use of modulation functions. This reconstruction is therefore not considered to be a modulated structure.

Modulated surface structures are characterised by satellite reflections visible in the vicinity of main reflections; we define the main reflections as being due to the undistorted substrate lattice, while a secondary set of reflections is due to the undistorted adsorbate lattice. For the diffraction pattern of modulated surfaces, we use an indexing scheme following the usual practice in X-ray diffraction, where additional indices are used to describe the positions of satellite reflections relative to the associated main reflections. For 2-D modulated surfaces, two additional indices are used. In surface X-ray diffraction conventionally three indices are used for the main reflections, while for LEED usually only two indices are used for the reflections (since the component of the scattering vector normal to the surface can be derived from the electron energy and is therefore usually omitted). To avoid misunderstandings, we

propose here to separate the three indices of the main X-ray reflection or the two indices of the LEED beam from the indices of the satellites by a semicolon; commas can be used to separate the indices when ambiguities still occur. As an example, assume that the 3-D diffraction vector of the reflection $\mathbf{I}(\mathbf{k}' - \mathbf{k}_0)$ is:

$$\mathbf{k}' - \mathbf{k}_0 = h\mathbf{a}_{\text{sub}}^* + k\mathbf{b}_{\text{sub}}^* + l\mathbf{c}_{\text{sub}}^* + m_1\mathbf{q}_1 + m_2\mathbf{q}_2. \quad (6.64)$$

The three indices h , k and l define the main reflections, while the satellite reflection indices are m_1 and m_2 : then the index is written as $(hkl; m_1m_2)$ or $(h, k, l; m_1, m_2)$ in X-ray diffraction. As the index l is usually omitted in LEED analyses, the index notations $(hk; m_1m_2)$ or $(h, k; m_1, m_2)$ can be used, as illustrated in Figure 6.41. For a 1-D modulation only one modulation wave exists, with one index m , yielding the index notations $(h, k; m)$ or $(hk; m)$ in LEED. This notation is used for commensurately as well as for incommensurately modulated lattices. The alternative for commensurate lattices when the modulation period is not too large is, of course, to use superstructure indices. In order to ensure a unique notation of the experimental data, the substrate reciprocal lattice is always used as a reference.

As an example with satellite reflections in large modulated cells, we consider the reconstruction of the Au(111) surface. At first, we consider a simplified model of the so-called $(\sqrt{3}\times 22)\text{rect}$ reconstruction of Au(111) [6.165]. The notation $(\sqrt{3}\times 22)\text{rect}$ defines a rectangular unit cell of dimensions $\sqrt{3}\times 22$ in units of the nearest-neighbour

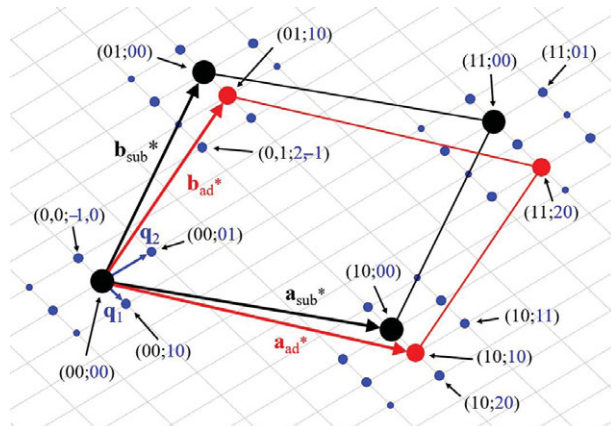


Figure 6.41 Example of indexing satellite reflections (red and blue spots) in LEED for a commensurate adsorbed overlayer on a substrate. The indices (defined in the text) refer to the main substrate reflections (black spots) for uniqueness. The red spots are reflections of the unmodulated adsorbate layer. The reciprocal lattice vectors of the substrate ($\mathbf{a}_{\text{sub}}^*$ and $\mathbf{b}_{\text{sub}}^*$) are coloured black, while those of the overlayer (\mathbf{a}_{ad}^* and \mathbf{b}_{ad}^*) are red and those of the modulation (\mathbf{q}_1 and \mathbf{q}_2) are blue. The reciprocal lattice of the modulation is shown as a grey grid: all its lattice points are potential diffraction spots, but spot intensities tend to decay away from the main reflections, most being too weak to detect, which is symbolised here as smaller spots. Black indices refer to the reciprocal lattice of the substrate, while blue indices refer to the reciprocal lattice of the modulation.

distance on the Au(111) surface. However, this label does not give the full picture of the reconstruction, since it was chosen based on the initial observations by LEED, which had limited resolution. The model proposed then consisted of a simple 1-D compression of the top layer and neglected the complex ‘herringbone’ or ‘chevron’ structure which was later found to correspond to a 2-D modulation. STM images of the actual structure are shown in Figure 6.35.

The model for the earlier 1-D modulation is shown in Figure 6.42(a): there are 24 unit cells in the top layer covering 23 unit cells in the second layer (the numbers 24 and 23 are based on later more accurate determinations). This corresponds to a 1-D compression by about 4.2%. The compression is in the $[1\bar{1}0]$ direction, referring to the cubic lattice of Au. The $[1\bar{1}0]$ direction is taken as the x direction. The stripes occur in the direction normal to it, that is, in the $[11\bar{2}]$ direction. (We use here the notation $(23 \times \sqrt{3})\text{rect}$ for comparison with the STM image shown in Figure 6.35).

The observed corrugation with two stripes in the $(23 \times \sqrt{3})\text{rect}$ unit cell can be easily modelled by two parameters. The compressed layer is modulated in three directions: there occur lateral shifts in the x and y directions and vertical shifts in the z direction, the latter being the corrugation observed in the STM images. In Figure 6.42(a) the corrugation is not calculated by a global modulation function but by assuming a local rigid ball model so that top Au atoms in bridge sites are higher than in fcc and hcp hollow sites. The corrugation is therefore determined indirectly by the lateral modulations. The lattice constants of the compressed top layer are $a' = \frac{23}{24}a_0\sqrt{2}$ and $b' = \sqrt{3}a_0$, where a_0 is the cubic lattice constant. A transverse modulation by a cosine function with an amplitude $(1/12)b'$ shifts the atoms from an fcc site to an hcp site. As is obvious from the STM images in Figure 6.35, the region with hcp sites is smaller than that with fcc sites (because fcc sites are energetically more favourable than hcp sites). This can be simulated by an additional longitudinal modulation with a sine function: in Figure 6.42(a) and (b), an amplitude of 0.14 nm has been used. The diffraction pattern from a single domain is shown in Figure 6.42(c) and the superposition due to three domain orientations in Figure 6.42(d). The indices refer to the substrate unit cell; the satellite reflection can be indexed by a single index counting the distance from the main reflections. There are no cross-satellites visible – such as $(10;21)$ – indicating that we have a superposition pattern from three separate 1-D modulated domains.

Figure 6.42(a) shows a simplified model with a 1-D modulation: the actual structure model exhibits a 2-D modulation, with a second modulation vector in the $[10\bar{1}]$ or $[01\bar{1}]$ direction of the cubic lattice. The satellite reflections corresponding to the 2-D modulation have been measured by A. R. Sandy et al. [6.171] with X-ray diffraction. A schematic structure model with two symmetrically equivalent 1-D modulated domains and the corresponding pattern with satellite reflections around the main reflections are shown in Figure 6.43. The structure model is taken from [6.171] and the directions indicated in the figure refer to the surface unit cell.

The modulation vectors of the Au(111) reconstruction have been determined in the detailed X-ray study by A. R. Sandy et al. [6.171]. The modulation periods are $L_K = 112.4a$ (32.43 nm) and $L_D = 22.5a - 22.9a$ (6.49–6.61 nm), where a is the NN-distance between Au atoms in the bulk, $a = a_0/\sqrt{2}$ and a_0 is the cubic lattice constant of Au.

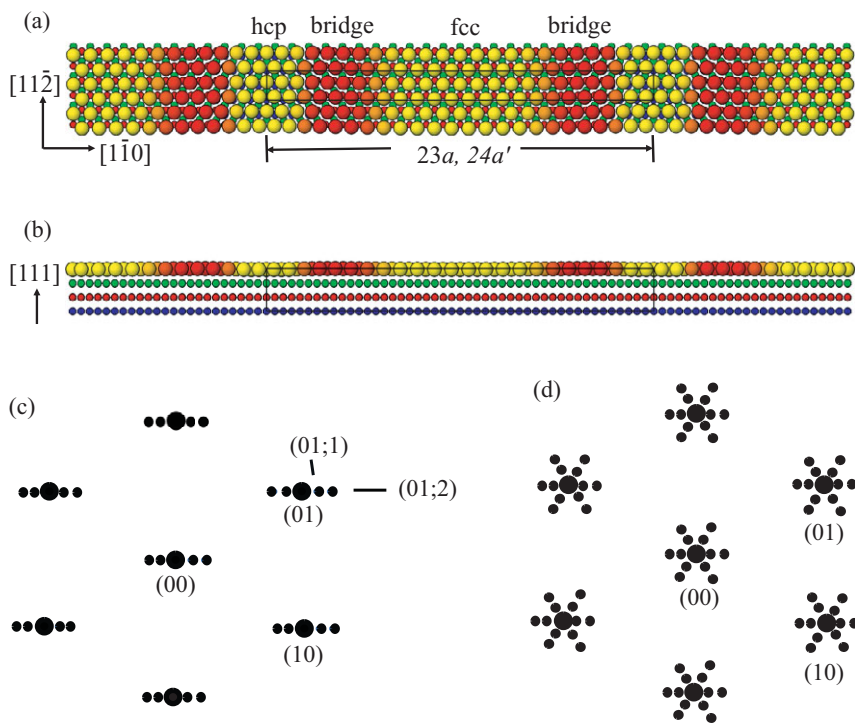


Figure 6.42 (a) Model of $\text{Au}(111)-(23 \times \sqrt{3})\text{rect}$ with 1-D compression and transverse and longitudinal sinusoidal modulations, in top view. The modulation parameters are explained in the text, where the lengths a and a' are also defined. (b) Side view of the corrugation derived from a rigid ball model, which is small and almost invisible in the drawing but indicated by the colours in the outermost layer: the Au atoms at bridge sites (red) are 0.023 nm (0.23 \AA) higher than at fcc and hcp hollow sites (yellow). (c) Diffraction pattern of a single domain (using spot indexing for a single modulation direction). (d) Superposition of diffraction patterns for three domain orientations.

To obtain a unique identification, the satellite reflections are related to the main reflections of the substrate and a single domain. Some indices are given in Figures 6.39 and 6.40. The use of superstructure indices would not be useful; furthermore, the use of scattering vectors gives the position in reciprocal space but offers no hint by which modulation vectors the satellite intensities are generated. The use of two additional indices m_1 and m_2 provides the easiest way to identify satellite reflections.

6.3.5 Modulation Functions

The modulation function of a lattice is frequently represented by a Fourier series as the easiest way to describe a modulation wave, even though this is not the only

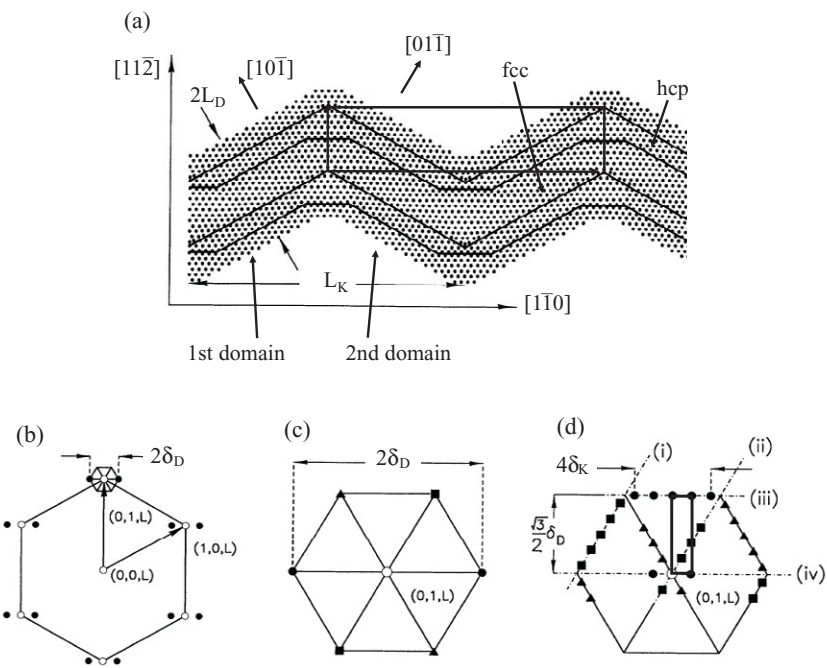


Figure 6.43 (a) Real space model of the 2-D reconstruction of Au(111) consisting of a regular sequence of two domains of the model shown in Figure 6.42 connected with rounded corners that give a ‘herringbone’ or ‘chevron’ appearance. The modulated superstructure cell is shown by the blue rectangle, with side lengths L_D and L_K . There exist three rotational domains of this model. (b–d) Reciprocal space representations near certain integer-order reflections: (b) First-order satellite reflections from a single domain of the striped phase, as in Figure 6.42(c). (c) Blow-up from panel (b) showing first-order satellite reflections around the $(0, 1, L)$ reflection from three domains of the striped phase. The distance to the main reflection is $\delta_D = 2\pi/L_D$. The modulation length of the striped phase, L_D , is shown in panel (a). (d) Satellites due to the ‘herringbone’ or ‘chevron’ structure around the (01) reflection measured by scans in different directions, in the same region shown in panel (c). The reciprocal cell of the modulation is indicated by the black rectangle. The wave vectors of the modulation are $q_1 = \delta_K = 2\pi/L_K$ and $q_2 = 2\pi/(\sqrt{3}/2L_D)$. Panels (b–d) use X-ray diffraction notation for the main reflections. The same patterns would be observable in LEED. Figure adapted with permission from [6.171] A. R. Sandy, S. G. J. Mochrie, D. M. Zehner, K. G. Huang and D. Gibbs, *Phys. Rev. B*, vol. 43, pp. 4667–4687, 1991. <https://doi.org/10.1103/PhysRevB.43.4667>. © (1991) by the American Physical Society.

possibility: other representations of the shift of the atoms may be preferred to avoid high-order Fourier coefficients in the Fourier series. Modulation functions are waves and are described by wave vectors \mathbf{q} in reciprocal space. For 2-D modulations two vectors are required and for each modulation vector one longitudinal and two transverse displacement directions are possible, as illustrated in Figure 6.32 for a 1-D modulation. On surfaces one of the two transverse waves describes the corrugation (or z modulation) of the layer. The second transverse modulation describes the in-plane lateral displacement, while the longitudinal wave describes the in-plane

compression or expansion. For simplicity, we consider here only the modulation within an adsorbate layer; the modulation of the substrate layers can be described analogously.

There are N atoms in the unit cell of the modulated lattice, with positions

$$\mathbf{r}_n = x_n \mathbf{a}_{\text{mod}} + y_n \mathbf{b}_{\text{mod}} + \Delta \mathbf{r}_n. \quad (6.65)$$

Here x_n and y_n are the atomic positions in units of the translation vector of the modulated lattice, ranging from 0 to 1; the perpendicular coordinate z_n is set to 0, as it is constant in the layer. The N displacements $\Delta \mathbf{r}_n$ of the N atoms are described by a Fourier series in which we use coefficients A and B for the cosine and sine terms, respectively; alternatively, a sine term and a phase could be used. The displacement of the n -th atom is in general given by:

$$\Delta \mathbf{r}_n = \{\Delta_n^x, \Delta_n^y, \Delta_n^z\}, \text{ with}$$

$$\Delta_n^j(x_n, y_n) = A_{00}^j + \sum_{s,t} \{A_{st}^j \cos(2\pi(sx_n + ty_n)) + B_{st}^j \sin(2\pi(sx_n + ty_n))\}. \quad (6.66)$$

The integer-valued indices s and t of the Fourier coefficients A_{st}^j and B_{st}^j refer to the wave vector \mathbf{q}_{st} , where s and t both range in the interval $\{0, \dots, M - 1\}$ and M is the highest useful frequency, given by the number of basic cells in the superstructure. Usually low-order Fourier coefficients suffice. The index j , with $j = 1, 2, 3$ (or x, y, z) indicates the type of displacement, that is, one longitudinal and two transverse displacements in two possible directions. It should be noted that for transverse modulations the shift vector is normal to the wave vector. An equivalent formulation of the Fourier series by sine terms and phases is frequently used in the literature on modulated structures:

$$\Delta_n^j(x_n, y_n) = A_{00}^j + \sum_{s,t} \left\{ A'_{st}^j \sin(2\pi(sx_n + ty_n + \Phi_{st}^j)) \right\}, \quad (6.67)$$

with

$$\tan(\Phi_{st}^j) = \frac{A_{st}^j}{B_{st}^j} \quad \text{and} \quad A'_{st}^j = \sqrt{(A_{st}^j)^2 + (B_{st}^j)^2}. \quad (6.68)$$

In the following, we shall use the description by coefficients A and B for the cosine and sine terms, respectively.

In structures with more than one atom per primitive unit cell of the adsorbate layer, each atom may have its own amplitude and phase of the modulation. For instance, the graphene layer has two atoms per unit cell, so that the number of atoms in the superstructure cell is doubled. The coordinates of the k -th atom in the n -th unit cell are:

$$\mathbf{r}_{k,n} = \{x_{k,n}, y_{k,n}, z_{k,n}\} = \{(m_1 + x_k) \mathbf{a}_{ad}, (m_2 + y_k) \mathbf{b}_{ad}, \Delta z(x_n, y_n)\}, \quad (6.69)$$

with $k = \{1, 2\}$, while m_1 and $m_2 = \{0, \dots, M - 1\}$ and $n = \{1, \dots, 2M^2\}$ label the unit cells; a $(M \times M)$ superstructure is assumed. The coordinates x_k and y_k refer here to

the mean lattice of the adsorbate layer, \mathbf{a}_{ad} and \mathbf{b}_{ad} . The shift of the z position of the k -th atom in the n -th unit cell is given by:

$$\Delta_{k,n}^z(x_{k,n}, y_{k,n}) = A_{00} + \sum_{s,t} \left\{ A_{s,t}^z \cos(2\pi(sx_{k,n} + ty_{k,n})) + B_{s,t}^z \sin(2\pi(sx_{k,n} + ty_{k,n})) \right\}. \quad (6.70)$$

In Eq. (6.70) we have used the same Fourier coefficients for all atoms of the layer, which is probably appropriate for graphene. It might be different for a modulated compound layer. For example, in a layer of hexagonal boron nitride on Rh(111) the modulation of the boron and nitrogen sublattices may have different Fourier components as the interaction with the substrate is expected to be different.

For less smooth modulations, such as a step function or sawtooth function, high-order Fourier coefficients would be required, but in these cases simpler functions would be more appropriate. Even though Fourier coefficients are linearly independent, their influence on the structure and on the diffracted intensity is highly correlated, especially for LEED where multiple scattering effects play a dominant role. Therefore, it may be appropriate to use Gaussian functions for a corrugation instead of Fourier coefficients where the height and width of a maximum is more easily controlled by two parameters than with many Fourier coefficients. Whatever function is used to describe the modulation, the Fourier series is in general valid for the cases occurring in structure analyses and we use it here to illustrate the principal characteristics of the diffraction pattern: for our qualitative discussion, the kinematic theory is adequate and will thus be used.

To illustrate modulation functions in a 2-D lattice with symmetry p3m1, two examples for the possible modulation vectors \mathbf{q}_{10} and \mathbf{q}_{11} with sinusoidal functions are shown in Figure 6.33. It should be noted that the wave functions describe the displacement of atoms in real space (Eq. (6.66)) and the waves are also observed in real space in the STM images, while the wave vectors are conventionally described in reciprocal space because they are observed in the diffraction pattern. The directions in real and reciprocal space for the hexagonal lattice are indicated in Figures 6.31(a) and (b).

6.3.6

Symmetry Restrictions of the Modulation

Symmetry restricts the Fourier coefficients A and B for the cosine and sine terms of Eqs. (6.66) and (6.70) or for the phases of these waves, depending on the space group of the modulated surface. For the symmetry p3m1 shown in Figure 6.33, the indices of the basis wave vectors are (10) and (01): the 3-fold symmetry makes them mutually equivalent. Besides multiples like (20), (30), etc., representing higher-order Fourier coefficients, combinations like (12), etc., may also occur in the symmetry group p3 but not in p3m1. We can distinguish the symmetries of the (10) and the (11) waves. There are three symmetrically equivalent directions for the (10) wave and six for the (11) wave. The (11) wave produces a 6-fold modulation pattern. For monoatomic lattices as shown in Figure 6.33 the (10) wave also produces a 6-fold pattern. The 3-fold

symmetry observed in the diffraction pattern results from the bulk crystal structure, that is, the underlying layers. Therefore, both directions are distinguished in the tables of the symmetry groups of modulated lattices (see for example in the International Tables [6.188]). This is of special interest for incommensurate structures. The symmetry of the commensurate superstructures considered here is not changed, of course: it remains p3m1. In this space group, only the z modulation and the longitudinal displacement are allowed. A longitudinal shift in the [10] direction implies a transverse shift in the [01] direction and vice versa, see for example Figure 6.33. An independent in-plane transverse wave in the [10] direction therefore does not occur; the same holds for the square lattices. Further symmetry restrictions exist for the cosine and sine terms of the Fourier coefficients or for the phases of the waves, respectively. The symmetry properties of the cosine and sine functions require that some coefficients vanish:

- | | | |
|-----------------------|---------------------------------|--------|
| (10) x displacement | $A_{10} = 0, B_{10} \neq 0$ | (6.71) |
| z displacement | $A_{10} \neq 0, B_{10} \neq 0,$ | |
| (11) x displacement | $A_{11} = 0, B_{11} \neq 0$ | (6.71) |
| z displacement | $A_{11} \neq 0, B_{11} = 0.$ | |

Similar restrictions exist for the other 2-D space groups. A list can be found in the International Tables [6.188]: see, for example, Table 9.8.3.4(b), entitled ‘(2+2)-Dimensional superspace groups’.

6.3.7 Diffraction from Modulated Surfaces

We consider first the characteristic features of the diffraction pattern in the kinematic theory, as these can be analytically calculated. A brief description has been given in Section 4.7 in connection with the interpretation of the diffraction pattern. The characteristic feature of the diffraction pattern from a modulated surface is a set of satellite reflections surrounding main reflections. We derive this feature in the kinematic theory, but the main characteristics of the diffraction pattern remain valid for LEED and in the multiple scattering theory.

The theory is only very briefly outlined here to explain the occurrence of satellite intensities and the characteristics of their intensity. The reader is referred to a textbook for a full description of the theory [6.183]. In the kinematic theory the amplitude of the diffracted wave is given by

$$A(\mathbf{k}' - \mathbf{k}_0) = \sum_n f_n(\mathbf{k}' - \mathbf{k}_0) e^{i(\mathbf{k}' - \mathbf{k}_0)\mathbf{r}_n}. \quad (6.72)$$

We consider displacive modulations. The atomic position vectors are then given by the position in the undistorted lattice and a shift which is described by the Fourier series in Eq. (6.66):

$$\mathbf{r}_n = \mathbf{r}_{0,n} + \Delta\mathbf{r}_n. \quad (6.73)$$

The diffraction amplitude can thus be written as

$$A(\mathbf{k}' - \mathbf{k}_0) = \sum_n f_n(\mathbf{k}' - \mathbf{k}_0) e^{i(\mathbf{k}' - \mathbf{k}_0)\mathbf{r}_{0,n}} e^{i(\mathbf{k}' - \mathbf{k}_0)\Delta\mathbf{r}_n}, \quad (6.74)$$

or, using the indices h, k, l for the main reflections,

$$A(hkl) = \sum_n f_n(hkl) e^{2\pi i(hx_{0,n} + ky_{0,n} + lz_{0,n})} e^{2\pi i(h\Delta_n^x + k\Delta_n^y + l\Delta_n^z)}. \quad (6.75)$$

The first phase factor in the sum of Eq. (6.75) refers to the undistorted lattice and gives the structure factor of the main reflections. The second phase factor contains the shift vectors and in a Fourier series expansion the sine and cosine terms occur in the exponential. These can be expanded into a sum over Bessel functions as

$$e^{iy \sin \theta} = \sum_{p=-\infty}^{\infty} J_p(y) e^{ip\theta}, \quad (6.76)$$

where J_p is the Bessel function of order p . After some rearrangement of the different factors, we obtain the reflection intensity for the simple example of a mono-atomic lattice and a 1-D sinusoidal modulation with the period M :

$$I(hkl) = |F(hkl)|^2 \cdot \left| \sum_{h,k,l} \sum_p \delta\left(h + \frac{p}{M}\right) \delta\left(k + \frac{p}{M}\right) \delta\left(l + \frac{p}{M}\right) J_p(D_x) J_p(D_y) J_p(D_z) \right|^2, \quad (6.77)$$

with $D_x = 2\pi h A^x$, $D_y = 2\pi k A^y$ and $D_z = 2\pi l A^z$. Here A^x is the amplitude of the sine wave in the x direction and analogously for A^y and A^z .

The formulas for the general case and for higher-order Fourier coefficients look more complicated, but the characteristic features of the diffraction pattern remain and can be concluded from Eq. (6.77) and the properties of the Bessel functions shown in Figure 6.44, namely:

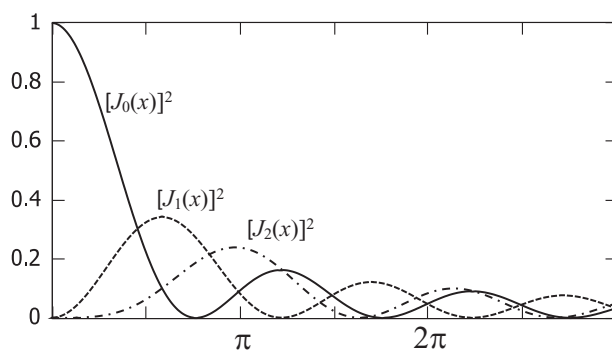


Figure 6.44 Square of the first three Bessel functions $[J_p(x)]^2$

- Each reflection is surrounded by an infinite set of satellite reflections in the case of incommensurate lattices. For commensurate superstructures the satellites will coincide with higher-order main reflections and their satellites, resulting in a finite density of reflections.
- The intensity of each satellite decreases (non-monotonously) with increasing distance from the nearest main reflection.
- The intensity of each satellite follows the intensity of the main reflection.
- The intensities of the main reflections decay as J_0^2 with increasing scattering vector while those of the satellites increase. This behaviour is illustrated in Figure 6.45.

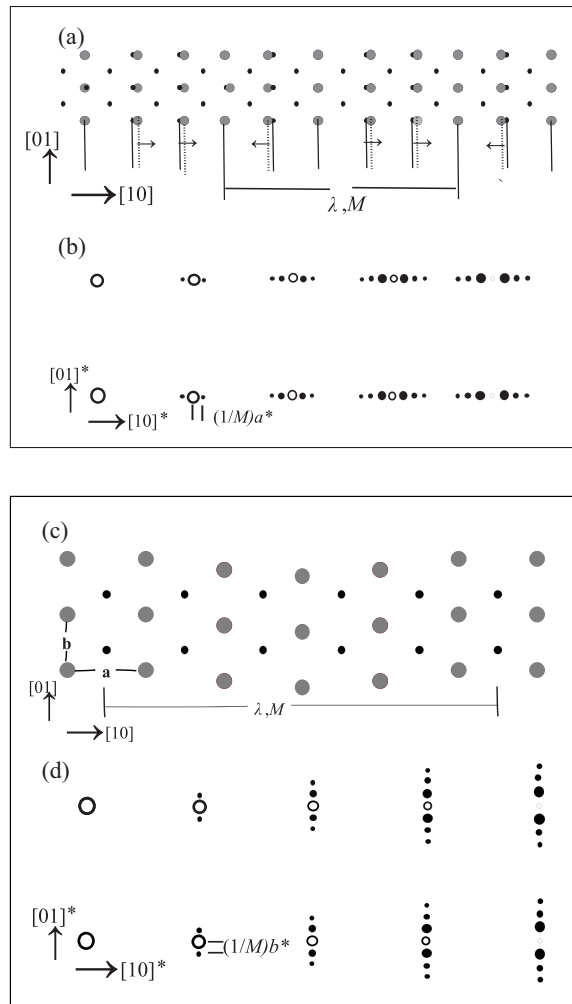


Figure 6.45 Characteristic diffraction pattern of two 1-D sinusoidal modulations: (a) longitudinal modulation and (b) corresponding diffraction pattern; (c) transverse modulation and (d) corresponding diffraction pattern. In (a) and (c) the black dots serve as a periodic grid to highlight the modulations (grey positions). In (b) and (d) the open circles are main reflections, while black dots are satellite reflections; dot size suggests average spot intensity.

The Bessel function of order 0 is a cosine-like function with decaying amplitude and characterises the intensity decay of the main reflections with increasing scattering vector. The higher-order Bessel functions are decaying sine-like functions where the maximum is shifted to higher values of the argument with increasing order. The characteristic diffraction patterns of two 1-D displacive modulations are shown in Figure 6.45.

Satellite reflections occur in the reciprocal lattice in the direction of the modulation vector. There are no satellites around the $(0k0)$ plane in reciprocal space for a longitudinal modulation in the $[100]$ direction and no satellites around the $(h00)$ plane for a transverse modulation with wave vector in $[100]$ direction and shift in the $[010]$ direction.

For modulations of the scattering amplitudes (as opposed to modulations of atomic positions) the diffraction pattern looks different. This occurs, for example, with a modulation of the occupation factor in X-ray diffraction. In LEED the effective scattering amplitude of an atom depends on its surroundings and is therefore always coupled to a displacive modulation. A periodic deviation from the mean atomic scattering factor may occur by a modulation of the occupation factor in compounds, by vacancies, by charge density waves or by other factors that do not change the atomic position. For a 1-D modulation with a period M the atomic scattering factor of the n -th atom can be written as:

$$f_n(hkl) = f_{o,n}(hkl) + \sum_s \Delta f_s e^{2\pi i s n/M}, \quad (6.78)$$

where Δf_s are the Fourier coefficients; the complex-number formulation of the Fourier series is used here. Equation (6.78) can be inserted into the structure factor equation (Eq. (6.75)) and it is directly seen that satellites occur around each reflection. Each Fourier component produces one satellite. The diffraction pattern is schematically shown in Figure 6.46.

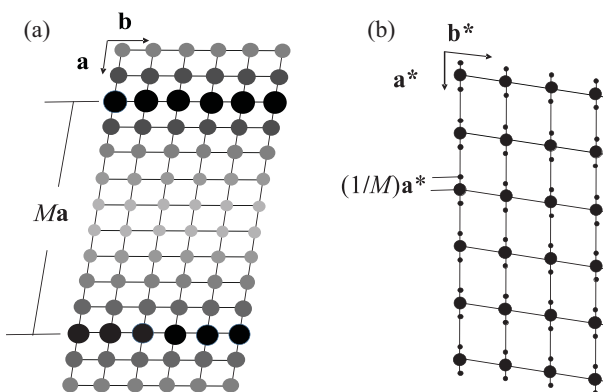


Figure 6.46 (a) Example of a modulation of the scattering factor with a periodic occupation of lattice points with different atoms. (b) Schematic drawing of the diffraction pattern for a sinusoidal modulation, showing only the nearest satellites.

6.3.8 Multiple Scattering Effects in LEED from Modulated Structures

Multiple scattering effects in LEED from modulated structures introduce several differences compared to X-ray diffraction. Because of multiple scattering, the effective scattering amplitude of an atom depends on its surroundings. This is illustrated in Figure 6.47. The effect is not small, as the amplitude and the phase of the effective scattering amplitude vary substantially when the interatomic distances and angles to the surrounding atoms are changed. The result is that any displacive modulation is accompanied by a modulation of the effective scattering factor. We may consider the superposition of two rigid lattices with different lattice constants. In X-ray diffraction the superposition of two reciprocal lattices is illustrated in Figure 6.48(a) and (b). Satellite reflections occur only when a modulation exists. This is not the case for multiple scattering: the superposition of two rigid lattices can produce non-zero intensity at all combinations of the two reciprocal nets. This can be explained by double and multiple diffraction from the two lattices, as illustrated in Figure 6.48(c), or by the variation of the effective scattering amplitude, as in Figure 6.47(b). Both interpretations are completely equivalent.

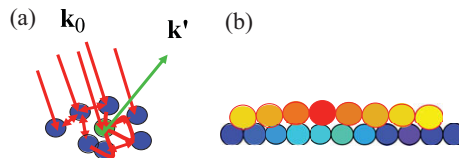


Figure 6.47 Illustration of multiple scattering in LEED. (a) The effective scattering amplitude relates the amplitude of the incoming wave \mathbf{k}_0 to that of the scattered wave \mathbf{k}' leaving the surface without further scattering (drawn in red are various multiple scattering paths that end at the same green atom). The effective scattering amplitude therefore depends on the surroundings of an atom. (b) Varying surroundings are symbolised by different colours of atoms in inequivalent positions.

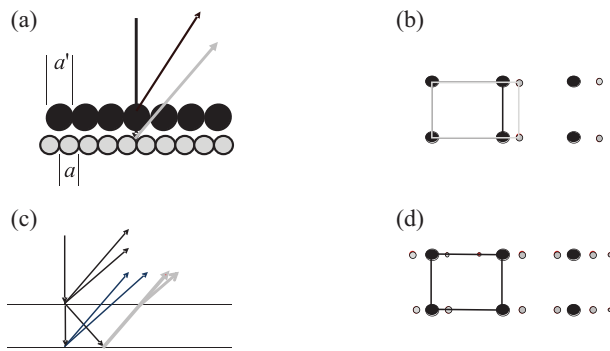


Figure 6.48 (a) Combination of two unmodulated lattices with lattice constants a and a' . (b) Diffraction pattern in X-ray diffraction showing the superposition of reflections at the points of the two corresponding reciprocal lattices. (c) Various multiple scattering paths in LEED (for normal incidence). (d) Diffraction pattern observed in LEED.

The consequence for LEED investigations of modulated surfaces is that it is not possible to distinguish whether reflections result from multiple diffraction or from surface modulation. By contrast, in X-ray diffraction it is possible to distinguish displacive modulations from density modulations by the observation of satellite reflections in the diffraction pattern.

In the kinematic scattering theory, the intensity of the satellite intensities follows the intensity of the main reflections and for displacive modulations the intensity increases with increasing distance from the main reflection, as illustrated in Figure 6.45. In X-ray diffraction the intensity of satellite reflections as a function of the scattering vector can be used to estimate modulation amplitudes; Patterson methods can be applied for that purpose [6.189]. However, this is not possible for LEED, although it remains in general true that the intensity of satellites increases with the modulation amplitude.

Due to multiple scattering in LEED, a modulation of the scattering amplitude occurs in addition to a displacive modulation. Therefore, more satellites are visible in LEED than in X-ray diffraction and occur also around the (00) spot; for a purely displacive modulation this would not be observed in X-ray diffraction for lateral modulations, see Figure 6.45. In the LEED pattern of modulated surfaces, the main factor determining the intensity of the satellites is a height modulation, that is, a transverse modulation normal to the plane of the surface. Since in LEED the measurement is usually made near normal incidence and at a high momentum transfer normal to the surface, the region in reciprocal space with low momentum transfer normal to the surface is rarely observed. Satellites near the (00) beam always occur at high momentum transfer normal to the surface and do not indicate a density modulation.